論文 / 著書情報
Article / Book Information

題目(和文)	
Title(English)	Detection of very high energy gamma rays from the direction of the vela pulsar
著者(和文)	吉越貴紀
Author(English)	Yoshikoshi Takanori
出典(和文)	学位:博士(理学), 学位授与機関:東京工業大学, 報告番号:甲第3118号, 授与年月日:1996年3月26日, 学位の種別:課程博士, 審査員:
Citation(English)	Degree:Doctor (Science), Conferring organization: Tokyo Institute of Technology, Report number:甲第3118号, Conferred date:1996/3/26, Degree Type:Course doctor, Examiner:
学位種別(和文)	博士論文
Type(English)	Doctoral Thesis

Detection of Very High Energy Gamma Rays from the Direction of the Vela Pulsar

A Dissertation Submitted

in Candidacy for the Degree of

Doctor of Science

Presented by

Takanori Yoshikoshi

Supervisor

Prof. F. Kakimoto

March, 1996

Tokyo Institute of Technology

Contents

Abstract

The Vela pulsar has been observed in TeV gamma rays with the 3.8 m telescope of the CANGAROO (Collaboration between Australia and Nippon (Japan) for a GAmma-Ray Observatory in the Outback) project between January 1993 and March 1995. Evidence of a gamma-ray signal has been detected at the $\sim 6\ \sigma$ statistical significance level. The integral gamma-ray flux is estimated to be $(2.5 \pm 0.5 \pm 0.4) \times 10^{-12}$ photons $\mathrm{cm}^{-2}\ \mathrm{sec}^{-1}$ above 2.5 ± 1.0 TeV, and the signal is consistent with steady emission over the three year time scale. No pulsed emission modulated with the pulsar period has been detected, and the 95 % confidence level flux upper limit to the pulsed emission from the pulsar is $(2.7 \pm 0.5) \times 10^{-13}$ photons $\mathrm{cm}^{-2}\ \mathrm{sec}^{-1}$ above 2.5 ± 1.0 TeV.

The most probable direction of the emission appears to be offset from the pulsar by about $0^\circ.14$. The tracking accuracy of the 3.8 m telescope was examined by studying the motion of bright stars in the field of view with the aid of simulations. The result shows that the tracking is accurate within errors less than $0^\circ.02$, which is comparable with the $0^\circ.01$ step size of the telescope driving motors.

The observation method entails imaging the atmospheric Čerenkov light from air showers which are initiated by gamma rays. The features of Čerenkov light images due to TeV gamma rays (gamma-ray images) have been investigated using Monte Carlo simulations. A new analysis method has been developed, and the observed signal appears to show the gamma-ray-like tendency inferred from the simulations, demonstrating that the signal is very likely to be due to gamma rays. A method to reconstruct a gamma-ray source direction has been developed; the "source probability density function (SPDF)", which enables the gamma-ray source direction to be inferred from the extended structure of the gamma-ray image, is defined. Using the SPDF, the location of the emission region was reconstructed with the accuracy of $\leq 0^\circ.18$. The possibility of the observed signal being offset from the pulsar or being extended is examined and discussed.

Acknowledgements

I would like to thank my supervisor, Prof. Fumio Kakimoto, for his support over the past six years. I also wish to thank Mr. Shoichi Ogio for his support and encouragement.

I would like to thank Prof. Tadashi Kifune (Institute for Cosmic Ray Research, University of Tokyo), Prof. Toru Tanimori (Tokyo Institute of Technology) and Prof. Yutaka Matsubara (Solar-Terrestrial Environment Laboratory, Nagoya University) for their suggestion in my research work. I would also like to thank my colleagues in the University of Adelaide; Prof. John Patterson, Prof. Ray Protheroe, Dr. Greg Thornton, Dr. Phil Edwards, Dr. Mike Roberts and Dr. Gavin Rowell for their help during my stay in Woomera and Adelaide. Thanks especially to Dr. Greg Thornton and Dr. Phil Edwards for kind reading my manuscript. Dr. Thornton is also given my thanks for his help in the period analysis. Thanks to Prof. Masaki Mori (Miyagi University of Education) for giving information about an EGRET pulsar. Thanks to others who assisted me in the observations in Woomera; Prof. Tadao Hara (Yamanashi Gakuin University), Dr. Atsumu Suzuki (Kobe University), Dr. Tadahisa Tamura (Kanagawa University) and Mr. Ryutaro Susukita (Kyoto University). All other colleagues in the CANGAROO collaboration are given my best thanks.

Thanks to my colleagues in the Kakimoto laboratory; Mr. Kenichi Kadota, Mr. Yuji Shirasaki, Mr. Nelson Gironda, Mr. Masahiro Takeda, Mr. Satoshi Ueno, Mr. Takekazu Nakamura, Mr. Daijiro Senda, Mr. Ryo Ohtsuki and Mr. Yukihide Shibuya for their encouragement. Dr. Shigeru Yoshida (Institute for Cosmic Ray Research, University of Tokyo) is also given my thanks for his suggestion and encouragement.

Chapter 1

Introduction

Astronomy is based on observing photons coming from the universe. It began with the observation of optical photons and extended to the other energy windows; radio, infrared, X-ray, gamma ray and so on. Gamma rays have the highest energy of these and are an interesting probe because they are directly related to the most energetic phenomena in the universe. To produce gamma rays, especially for gamma rays of relatively high energies, it is necessary to accelerate charged particles to at least the same energies as the gamma rays. Therefore, the neighborhood of a gamma-ray source, or the gamma-ray source itself, must be a part of the solution to the long-standing question of the origin of cosmic rays.

Recently, gamma-ray astronomy has become a quite active field of astronomy. Gamma rays in the energy region below 10 GeV (= 10^{10} eV) have been intensively investigated by the Compton Gamma-Ray Observatory (CGRO) satellite, launched in 1991. The Energetic Gamma-Ray Experiment Telescope (EGRET), which is one of four instruments on the CGRO, covers the highest energy range of satellite experiments and has revealed more than 100 gamma-ray sources at 100 MeV [39, 119]. About the half of them have not been identified with the objects observed at the other wavelengths and the production mechanisms of the gamma rays in the sources are not well understood. On the other hand, in the energy region above 200 GeV, the Crab nebula was identified at the Whipple Observatory as the first "standard" gamma-ray source for ground-based gamma-ray telescopes. Furthermore, TeV (= 10^{12} eV) gamma rays from the Active Galactic Nuclei (AGN), Markarian 421 [91] and Markarian 501 [93], were detected at the same observatory. In spite of about 40 AGNs having been identified by EGRET, TeV gamma rays have been detected from the only two nearby AGNs ($z \sim 0.03$) so far, and this fact is strong evidence for the absorption of TeV gamma rays by the intergalactic infrared radiation field [32, 109]. Gamma rays from the above TeV gamma-ray sources were detected using the atmospheric Čerenkov imaging technique, and this technique has drastically increased the sensitivity of ground-based gamma-ray telescopes. The observation and analysis methods in this technique have been established by the Whipple Observatory and some other observatories.

The 3.8 m telescope of CANGAROO (Collaboration between Australia and Nippon (Japan) for a GAmma-Ray Observatory in the Outback) has been in operation since 1992 to search the southern hemisphere for TeV gamma-ray sources. We have ever detected TeV gamma-rays from the Crab nebula [113] and PSR 1706 − 44 [63] using the atmospheric Čerenkov imaging technique. In particular, PSR 1706 − 44 has been identified in our observations as the first TeV gamma-ray source in the southern hemisphere. We have also observed other TeV gamma-ray source candidates; pulsars (the Vela pulsar, PSR 1055 − 52 and PSR 1259 − 63), AGNs (PKS 0521 − 365 and PKS 2005 − 489) and supernova remnants (W28). The data are still in analyses.

To date, EGRET has detected pulsed gamma-ray emission from seven pulsars. Pulsars are rotating, magnetized neutron stars and they are one possible class of candidates for TeV gamma-ray sources. Many theoretical models for pulsars and their gamma-ray production mechanisms have been proposed and some models successfully explained several features of the emission from pulsars and their environments. However, uncertainties still remain and a self-consistent model of pulsars has not been established. In order to understand high energy phenomena at pulsars, more TeV gamma-ray observations of pulsars are necessary. Three of the seven pulsars observed by EGRET are in the southern hemisphere and one of them, PSR 1706 − 44, has been already identified by the CANGAROO 3.8 m telescope as a TeV gamma-ray source. The Vela pulsar is another southern EGRET pulsar and is the brightest source in the EGRET energy region. Therefore, it is natural to think that the Vela pulsar may also be emitting TeV gamma rays, and it may be possible to contribute to understanding pulsar mechanisms by investigating TeV gamma-ray emission from the Vela pulsar. The main purpose of this thesis is to investigate TeV gamma-ray emission from the Vela pulsar and to discuss the production mechanisms of TeV gamma rays around the pulsar.

Only four TeV gamma-ray sources (the Crab nebula, PSR $1706-44$, Markarian 421 and Markarian 501) have been found by ground-based telescopes so far, however, more sensitive telescopes are planned or under construction at present and it can be expected that more TeV gamma-ray sources will be found as the threshold energies of the telescopes reduces towards the EGRET energy.

Chapter 2

Very High Energy Gamma-Ray Astronomy

2.1 Classification of Gamma-Ray Astronomy

Gamma rays are the most energetic photons. Their energy extends from 0.51 MeV (the electron's rest mass) up to the highest observed particle energy (10^{20} eV). Because of the wide energy range (fifteen decades!), there are several detection methods for gamma rays depending on their energy, and gamma-ray astronomy is divided into several energy ranges based on the detection methods. Following Weekes's definition [124], they are described in Table 2.1.

Gamma rays up to about 10 GeV, the "High Energy" (HE) region, have been observed using gamma-ray satellites, SAS-2 [38], COS-B [94] and CGRO [103]. To date, as mentioned in Chapter 1, 129 HE gamma-ray sources have been identified [119] and the galactic diffuse HE gamma-ray distribution has been investigated precisely in their missions [14, 75]. However, with the present technology it is not feasible to launch satellites which can efficiently detect gamma rays of energy greater than 10 GeV because of constraints of size and weight and power law spectra ($\propto E^{-\gamma}$) of gamma rays. Therefore, gamma-ray observations at energies greater than 100 GeV have been carried out using ground-based detectors.

Energy (eV)	Greek	Classification	Technique (Observation platform)
$5.1 \times 10^5 \sim 1 \times 10^7$	$0.51 \sim 10$ MeV	low / nuclear (LE)	scintillator (satellite)
$1 \times 10^7 \sim 3 \times 10^7$	$10 \sim 30$ MeV	medium (ME)	Compton telescope (satellite)
$3 \times 10^7 \sim 10^{10}$	$0.03 \sim 10$ GeV	high (HE, 100 MeV)	spark chamber (satellite)
$10^{10} \sim 10^{14}$	$0.01 \sim 100$ TeV	very high (VHE, TeV)	atmospheric Čerenkov (mountain / sea level)
$10^{14} \sim 10^{17}$	$0.1 \sim 100$ PeV	ultra high (UHE, PeV)	air shower array (mountain)
$10^{17} \sim 10^{20}$	$0.1 \sim 100$ EeV	extremely high (EHE, EeV)	air shower array (sea level)

Table 2.1: Classification of gamma-ray astronomy.

If a gamma ray enters the earth's atmosphere, it initiates an Extensive Air Shower (EAS). All ground-based gamma-ray detection methods are based on sampling a part of an EAS, using the atmosphere as a large target. This "indirect" detection method has the advantage of large effective detection area compared with "direct" detection by satellites, but has the difficulty of distinguishing EASs initiated by gamma rays from the overwhelming background EASs initiated by cosmic-ray nuclei.

Gamma rays in the "Very High Energy" (VHE) region are detected using the "atmospheric Čerenkov technique". In this technique Čerenkov light radiated from relativistic charged particles in an EAS are detected by one or several ground-based telescopes. Čerenkov light is radiated in the upper atmosphere, and thus the difference in the development of EASs between primary gamma rays and primary cosmic rays is well reflected in the angular distribution of the light. Angular resolution of typically $0^\circ.1$ is obtained by imaging the Čerenkov light.

2.2 VHE Gamma-Ray Production Processes

VHE gamma rays are produced from highly accelerated charged particles in the following processes.

Neutral pion decay: If a high energy proton (or nucleus) interacts with matter or ambient radiation, neutral pions are generated in multiparticle production. Each neutral pion immediately decays into two gamma rays with a mean lifetime of $0.83 \times 10^{-16}\gamma_\pi$ sec, where γ_π is the Lorentz factor of the neutral pion.

Inverse Compton scattering: In this process, a gamma ray is produced when a relativistic electron interacts with an ambient photon. An ambient photon of energy ϵ appears to be moving with an energy $\gamma\epsilon$ in the rest system of a relativistic electron with Lorentz factor γ. In this inertial frame, the Compton scattered photon has an energy less than $\sim \gamma\epsilon$ and, when transformed back to the laboratory system, an energy $\sim \gamma^2\epsilon$. The energy of the Compton boosted photon is given by

$$\begin{aligned} E \sim \gamma^2\epsilon \quad &\text{when} \quad \gamma\epsilon \ll m_e c^2, \\ E \sim \gamma m_e c^2 \quad &\text{when} \quad \gamma\epsilon \gg m_e c^2, \end{aligned} \tag{2.1}$$

where m_e is the electron's rest mass. This process is important when the density of ambient photons is high.

Bremsstrahlung: When an electron (or any other charged particle) is accelerated in the Coulomb field of a nucleus, bremsstrahlung photons are emitted. The bremsstrahlung photons have the spectral shape $\sim 1/E_\gamma$, so that more photons are emitted at lower energies.

Synchrotron radiation: An electron (or any other charged particle) is accelerated when it traverses a magnetic field, and, as a result, photons are emitted. In a homogeneous magnetic field of strength H, the characteristic photon energy E (eV) is [94]

$$E = 5 \times 10^{-9} H_{\perp} \gamma_e^2, \tag{2.2}$$

where γ_e is the Lorentz factor of the electron, $H_{\perp} = H \sin\theta$ is in gauss and θ is the angle between the electron's velocity and the magnetic field. (2.2) implies that only extreme relativistic electrons in an extreme strong magnetic field can produce VHE gamma rays. However, low energy photons generated in this process play an important role to supply with target photons for inverse Compton process.

Curvature radiation: In the exceptionally strong magnetic field of a pulsar, high energy electrons and positrons are constrained to move parallel to the magnetic field lines. The particles are accelerated when they move along the curved field lines, and radiate "curvature" radiation in their direction of motion. The characteristic energy of this radiation, E_c (eV), is given by [94]

$$E_c \sim \frac{3}{2} \frac{\hbar c \gamma^3}{\rho_c} = \frac{2.96 \times 10^{-5} \gamma^3}{\rho_c}, \tag{2.3}$$

where ρ_c (cm) is the radius of curvature of the magnetic field line, $\hbar = h/2\pi$ and γ is the Lorentz factor of the particle. This process is important for very high energy electrons and positrons in the environments of pulsars.

Among the above processes, inverse Compton scattering is more effective to produce higher energy photons, because accelerated electrons can give almost all their energies to scattered photons. Mechanisms to accelerate primary charged particles to the energies greater than the VHE region are described in the following section.

2.3 VHE Gamma-Ray Source Models

As mentioned in Section 2.2, highly accelerated charged particles are necessary to produce VHE gamma rays. In this section, VHE gamma-ray source candidates are reviewed, as well as their particle acceleration mechanisms.

2.3.1 Pulsars

Pulsars, whose radiation is pulsed with a very regular period, were discovered in radio observations [56]. Most of the periods observed are ~ 1 sec, but they span the range $0.001 \sim 5$ sec [115]. Most of pulsars are observed to be slowing down and this fact implies a part of their energies is released into the interstellar space. A few of more than 500 known radio pulsars also emit pulses at visible, X-ray or gamma-ray frequencies. Most of pulsars populate the plane of our galaxy [115] but a few pulsars have been discovered in the Large Magellanic Cloud (LMC) and the Small Magellanic Cloud (SMC) [76].

It is now generally believed that pulsars are rapidly rotating magnetized neutron stars. Figure 2.1 shows a schematic view of a pulsar. The magnetic field is thought to be a dipole field as the most plausible assumption. Magnetic dipole radiation is radiated from a rotating dipole and for a dipole moment $\vec{\mu}$ rotating at angular frequency Ω, with angle α between its spin axis and $\vec{\mu}$, the radiation rate is

$$\dot{E} = \frac{2\mu^2\Omega^4 \sin^2\alpha}{3c^3} \sim 4 \times 10^{43} \left(\frac{B}{10^{12}\ \mathrm{G}}\right)^2 \left(\frac{P}{1\ \mathrm{msec}}\right)^{-4}\ \mathrm{erg\ sec^{-1}}. \tag{2.4}$$

For a neutron star of radius R, the magnetic moment and the neutron star's surface magnetic field strength B are related by $\mu = BR^3$. Assuming the radiation power of (2.4) is equivalent to the "spindown luminosity",

$$\dot{E} = -I\Omega\dot{\Omega} = 4\pi^2 I\dot{P}P^{-3}, \tag{2.5}$$

where I is the moment of inertia and $P = 2\pi/\Omega$, the neutron star's surface magnetic field

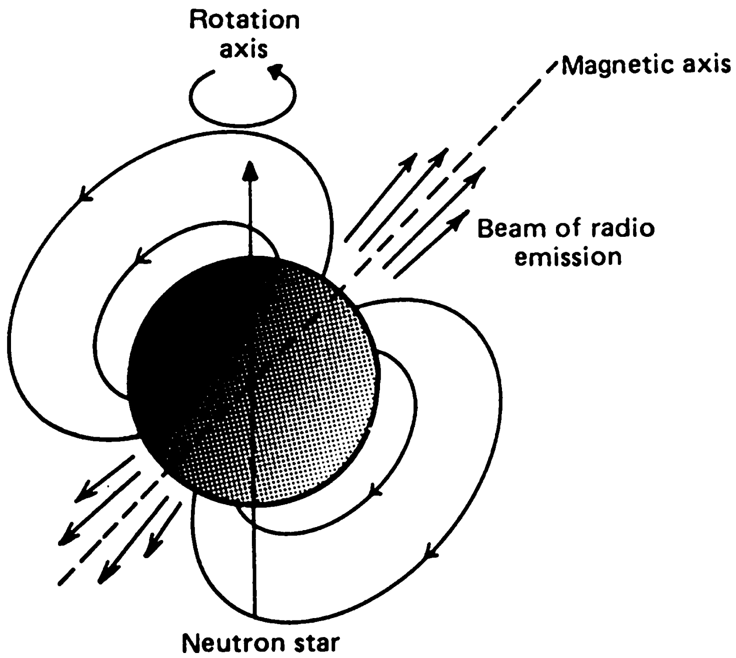

Figure 2.1: A schematic model of a pulsar as a magnetized rotating neutron star in which the magnetic and rotation axes are misaligned [69].

strength is

$$B = \left(\frac{3c^3 I P\dot{P}}{8\pi^2 R^6}\right)^{1/2} \sim 3.2 \times 10^{19} (P\dot{P})^{1/2} \text{ G}, \tag{2.6}$$

where $R = 10^6$ cm, $I = 10^{45}$ g cm^2 and $\sin\alpha = 1$ are taken. For most of pulsars it is $\sim 10^{12}$ G [87]. This rapidly rotating strong magnetic field induces a strong electric field. Its potential drop between the magnetic pole and equator is [51]

$$V \sim \frac{2\pi R^2 B}{cP} = 6 \times 10^{16} \left(\frac{B}{10^{12}\text{ G}}\right)\left(\frac{P}{1\text{ sec}}\right)^{-1} \text{ V}. \tag{2.7}$$

Caused by this strong electric field, any neutron star must be surrounded by plasma [45]. Plasma particles can move only parallel to the magnetic field lines owing to the strong magnetic field, thus the magnetic field lines become equipotentials ($\vec{E} \cdot \vec{B} = 0$). The plasma particles corotate with the neutron star within the light cylinder, at which the corotating

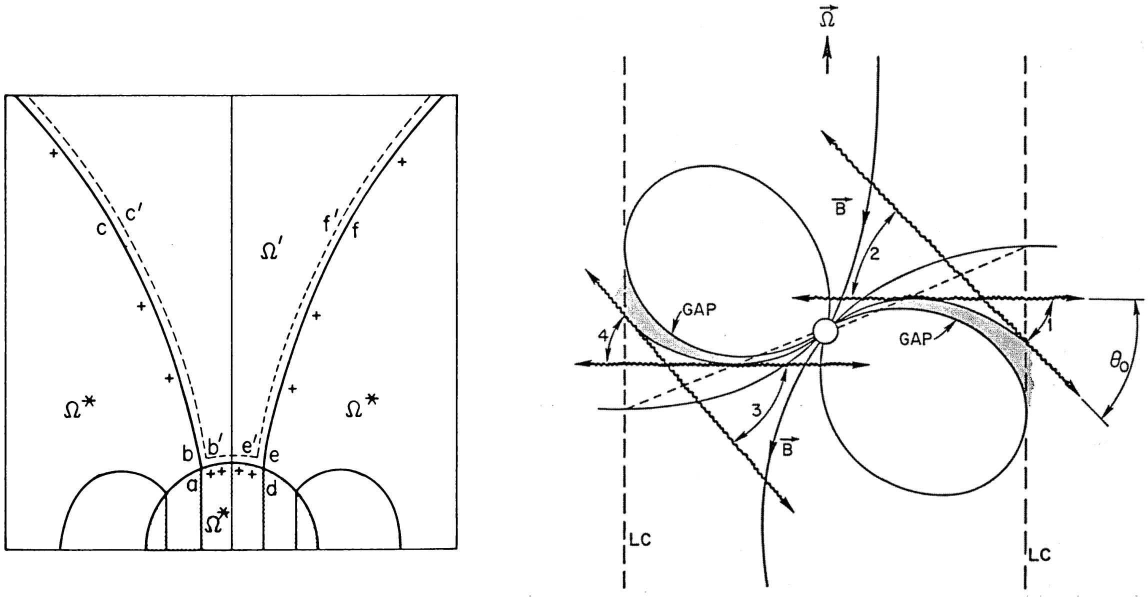

Figure 2.2: Schematic locations of vacuum gaps in phenomenological pulsar models. In the polar cap model (left), vacuum gaps are generated at the magnetic poles of the neutron star, between the solid and dashed lines [100]. Vacuum gaps in the outer gap model (right) are generated near the light cylinder (LC) [24].

plasma velocity is equal to the speed of light and its radius is

$$R_L = \frac{c}{\Omega} \sim 1.5 \times 10^6 \left(\frac{P}{1 \text{ msec}}\right) \text{ cm.} \tag{2.8}$$

In the above "basic" model, it is impossible to effectively accelerate charged particles in the pulsar's magnetosphere because plasma flow neutralizes the electric field parallel to the magnetic field lines. However, recent phenomenological models indicate the existence of vacuum gaps in the magnetosphere and high energy "curvature" or "inverse Compton" or "synchrotron" photons are produced by the accelerated particles. There are now two kinds of phenomenological models; the "polar cap" model [100, 111] and the "outer gap" model [24], which differ in the location of gaps. In the polar cap model, vacuum gaps are generated at the neutron star's magnetic poles as shown in the left of Figure 2.2. On the other hand in the outer gap model, gaps are more distant from the neutron star, but are inside of the light cylinder as shown in the right of Figure 2.2. They explain the observed pulses due to rotating narrow radiation from the local vacuum gaps.

Almost all observed radio profiles of pulsars have been explained by the polar cap model [70]. However, this model has the difficulty explaining observed gamma-ray emissions in the energy range above 100 MeV, because the polar cap region has a strong magnetic field ($\sim 10^{12}$ G) in which photons of energy greater than $\sim$ 100 MeV immediately pair-produce ("magnetic pair production" [35]) and cannot escape the polar cap region [5]. On the other hand, a magnetic field in the outer gap region is much weaker than that in the polar cap region ($10^4 \sim 10^5$ G for the case of the Vela pulsar [24]) and high energy photons can escape the outer gap region. In the outer gap model, there are two types of outer gaps on the basis of their radiation mechanisms; they are the "Crab-type" and "Vela-type" outer gaps [25, 26]. Accelerated electrons and positrons in the Crab-type outer gap lose most of their energies via curvature radiation instead of synchrotron radiation as in the case of the Vela-type outer gap. This difference is due to the smaller curvature radii of the magnetic field lines in the Crab-type outer gap. The Crab-type outer gap will turn to the Vela-type outer gap when

$$P > 4.6 \times 10^{-2} \left(\frac{B}{10^{12}\ \mathrm{G}} \right)^{2/5} \ \mathrm{sec}, \tag{2.9}$$

where P is the pulsar period and B is the surface magnetic field [26]. Pulsars having the Crab-type (Vela-type) outer gap are called Crab-like (Vela-like) pulsars. There are, at present, only a few observed pulsars in the Crab-like region. The outer gap model predicts gamma-ray emission from the outer gap turning off when

$$P > 0.17 \left(\frac{B}{10^{12}\ \mathrm{G}} \right)^{5/12} \alpha^{-5/4} \sin^{1/6}\theta \ \mathrm{sec}, \tag{2.10}$$

where α is the ratio of the mean distance from the pulsar to the outer gap to the light cylinder radius and θ is the mean pitch angle of the secondary electrons and positrons[1] with respect

[1] In the model of Cheng, Ho and Ruderman [25], electrons and positrons accelerated in the Vela-type outer gap (primary $e^{\pm}$) produce primary gamma rays via inverse Compton scattering. Then, secondary $e^{\pm}$ pairs are produced by the primary gamma rays [80].

to the local magnetic field [26]. Therefore, most of radio pulsars ($P \sim 1$ sec) cannot have outer gap accelerators [23].

Seven gamma-ray emitting pulsars have been identified so far in the mission of the CGRO satellite. They are the Crab pulsar [82], the Vela pulsar [60], Geminga [13], PSR 1706 − 44 [118], PSR 1055−52 [40], PSR 1951+32 [95] and PSR 0656+14 [96]. Of these, only Geminga has no detectable radio pulses. Of the more than 500 known radio pulsars, these gamma-ray pulsars belong to the class of the highest values of the total energy flux at the earth, which is proportional to $\dot{E}/d^2$, where $\dot{E}$ is the spindown luminosity and d is the distance to the pulsar [95], and therefore they are strong candidates for VHE gamma-ray sources. Figure 2.3 shows integral energy spectra of the seven pulsars observed by EGRET. Their spectra are well represented by power laws, and if they are extrapolated to the VHE region, their fluxes are well above the sensitivity of the CANGAROO 3.8 m telescope for gamma rays. Figure 2.4 shows the plot of the gamma-ray efficiencies $\eta = L_\gamma/\dot{E}$ (L_γ is the gamma-ray luminosity at 100 MeV) versus the characteristic ages $\tau = P/2\dot{P}$ for the EGRET pulsars [95, 96]. The gamma-ray efficiencies roughly tend to increase with age and are approaching 100 % for the characteristic ages approaching 10^6 years. No HE gamma-ray pulsars have been detected with ages greater than 10^6 years and this possibly indicates that the HE gamma-ray emission turns off for older pulsars as expected in the outer gap model [101]. In all of pulsars, not only the gamma-ray pulsars, visible luminosities, which have ever been given by radio, optical, X-ray and gamma-ray observations, are much less than the spindown luminosity given by (2.5), and it is possible that the residual energies are converted into gamma rays of the energy greater than the HE region.

2.3.2 Supernova Remnants (SNRs)

Supernova remnants (SNRs) are remnants formed after supernova explosions, and generally believed to be a source of galactic cosmic rays. The first-order Fermi acceleration by shock waves at the supernova shell is generally accepted as an acceleration mechanism

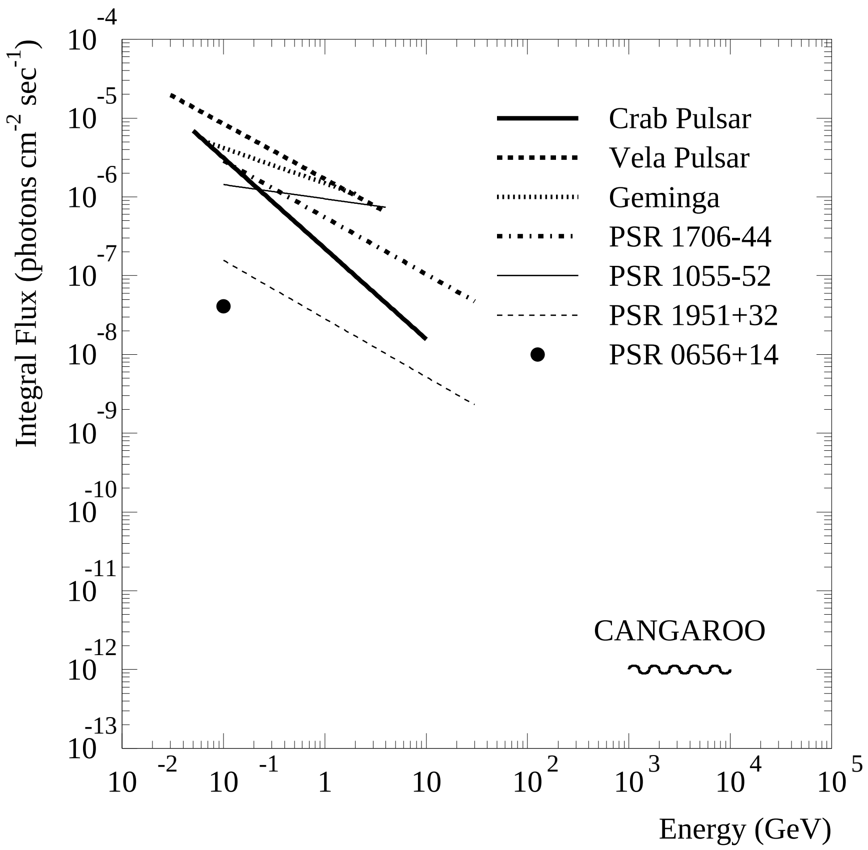

Figure 2.3: Integral energy spectra of the seven EGRET pulsars. The wavy line shows the sensitivity of the CANGAROO 3.8 m telescope for gamma rays.

of cosmic rays [18]. Since cosmic rays can produce VHE gamma rays via interactions with ambient matter and neutral pion decay (Section 2.2), SNRs can also be candidates for VHE gamma-ray sources.

Fermi (1949) proposed that cosmic rays are accelerated in the interstellar space of the galaxy by collisions against moving magnetic fields [37]. Cosmic-ray particles moving among irregular magnetic fields elastically collide against irregularities of the fields. Since the fre-

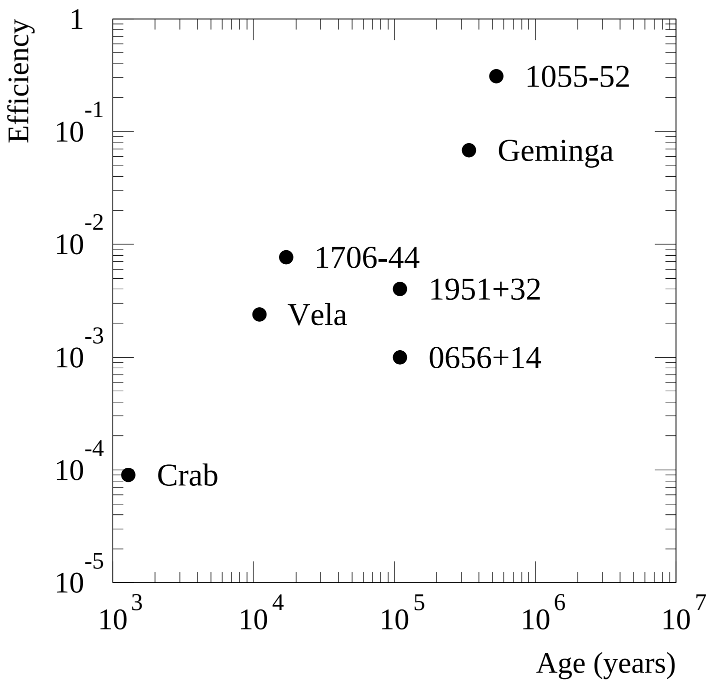

Figure 2.4: The gamma-ray efficiencies ($\eta = L_\gamma/\dot{E}$) versus the characteristic ages ($\tau = P/2\dot{P}$) for the EGRET pulsars [95, 96].

quency of encounters is proportional to the relative velocity, the probability of a "head-on" collision is higher than that of an "overtaking" collision. The net mean energy gain per collision is

$$\frac{\Delta E}{E} = 4\gamma_V^2 \left(\frac{V}{c}\right)^2 . \tag{2.11}$$

The acceleration by (2.11), in which $\Delta E/E$ is proportional to $(V/c)^2$, is known as the "second-order Fermi acceleration". If this process is associated with a strong shock wave, such as a supernova shock wave, particles which are repeatedly scattered across the shock can be efficiently accelerated almost only by head-on collisions because the magnetic flow velocity upstream of the shock is faster than the downstream velocity. In this case, the energy gain per collision is $\Delta E/E \sim 2(V/c)$, and this process is called the "first-order Fermi acceleration". The first-order Fermi acceleration is much more efficient than the second-order Fermi acceleration because $V \ll c$. Fermi's acceleration models have the advantage of yielding naturally an inverse power law for the spectral distribution of cosmic rays [69].

Naito and Takahara have calculated the gamma-ray spectra resulting from proton-proton collisions in a spherical supernova shell [79]. If their assumptions are correct, gamma rays produced via neutral pion decays appear to be observable in the VHE region from nearby SNRs. They have given several nearby SNRs possible to emit VHE gamma rays in their model; Vela XYZ (0.5 kpc), SN 1006 (1.0 kpc), Crab (2.0 kpc), IC 443 (2.0 kpc) and W44 (3.0 kpc). Sturner and Dermer have suggested that 13 sources associate with SNRs of the 37 unidentified Galactic plane sources in the first EGRET source catalog [110]. Vela, IC443 and W44 are also included in the 13 SNRs.

2.3.3 Pulsar Winds and Synchrotron Nebulae

A compact object, a neutron star or a black hole, is theoretically expected to be formed at a supernova explosion if the progenitor star's mass exceeds a critical mass ($\sim 8M_\odot$ [106]), and some neutron stars have actually been found as pulsars within SNRs. In this case, surrounding nebulae can be fed a great fraction of the spindown energy by their pulsars. These filled-center nebulae or SNRs are often called "plerions" [126, 127]. The dipole electromagnetic waves of (2.4) have the same frequency as the pulsar's rotation frequency, and cannot propagate in the plasma because their frequency is well below the plasma frequency ν,

$$\nu = \frac{1}{2\pi}\left(\frac{ne^2}{m_e\epsilon_0}\right)^{1/2} \sim 9.0 \times 10^3 n^{1/2}\,\mathrm{sec}^{-1}, \tag{2.12}$$

where n is the plasma density in cm^{-3} [4]. Instead of the dipole waves, the pulsar spindown energy is possibly transported by a relativistic magnetohydrodynamic (MHD) wind consisting mostly of electron-positron pairs. This "pulsar wind" can form a shock at which the surrounding nebula can provide enough pressure to balance the wind ram pressure as shown in Figure 2.5 [61, 97]. Electrons can be accelerated at the shock and boost synchrotron or

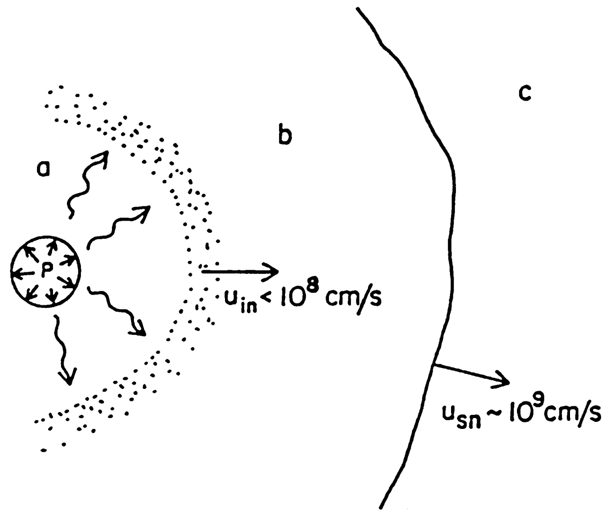

Figure 2.5: A schematic view of a pulsar wind in a SNR [51]. The inner circle of the radius r_s is the shock generated by the pulsar wind.

background (infrared, 2.7 K) photon energies by inverse Compton scattering possibly up to the UHE region. If the boosted photon is a synchrotron photon, this process is called the "synchrotron-self-Compton (SSC) model".

The Crab nebula has been confirmed as a VHE gamma-ray source by many groups [9, 47, 66, 113, 122]. A plausible interpretation for the VHE gamma-ray emission from the Crab nebula has been given by De Jager and Harding appling the above scenario [31]. In their model, the maximum electron energy at the shock is given by

$$E_{max} \sim eB_s r_s, \tag{2.13}$$

where B_s is the magnetic field strength at the shock and r_s is the distance of the shock from the pulsar. Following Kennel and Coroniti [62], B_s is approximated as

$$B_s \sim \frac{3(1-4\sigma)}{r_s}\left[\frac{\sigma\dot{E}}{(1+\sigma)c}\right]^{1/2}, \tag{2.14}$$

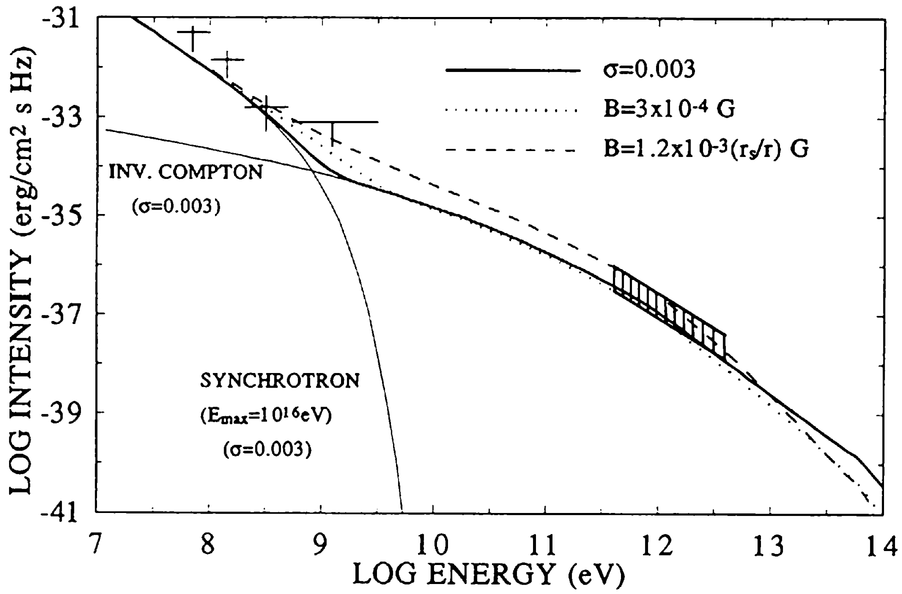

Figure 2.6: The expected gamma-ray spectrum of the Crab nebula calculated from the MHD and SSC models [31]. The observed HE (COS-B) and VHE (the Whipple Observatory) gamma-ray spectra have been explained to be of synchrotron and inverse Compton photons, respectively.

where $\dot{E}$ is the spindown luminosity of the pulsar and σ is the ratio of the magnetic energy density to the particle energy density just ahead of the shock, which has been estimated to be very small by some authors [34, 61, 97]. Taking the optimum value of σ estimated by Kennel and Coroniti, $\sigma = 0.003$, $E_{max} \sim 10^{16}$ eV for the case of the Crab nebula. Figure 2.6 shows the gamma-ray spectrum of the Crab nebula calculated by De Jager and Harding using the MHD and SSC models. The observed HE and VHE gamma-ray spectra have been explained to be of synchrotron and inverse Compton photons, respectively (Aharonian and Atoyan have, however, suggested that the spectrum of the Crab nebula is not well explained only by the SSC model and also introduced the bremsstrahlung of relativistic electrons [1]).

The properties of some of the principal plerions are summarized in Table 2.2 [105]. Four

Source name	Central object	Period (msec)	Distance (kpc)	Age (log(yr))
Crab nebula	PSR 0531 + 21 (Crab pulsar)	33	2.0	3.09
CTB 80	PSR 1951 + 32	39	3	5.02
SNR 0540 − 69	PSR 0540 − 69	50	55	3.22
Vela X	PSR 0833 − 45 (Vela pulsar)	89	0.5	4.05
MSH 15 − 52	PSR 1509 − 58	150	4.2	5.02
G201.2 + 82	PSR 0656 + 14	385	0.4	5.04
CTB 109	-	6980	3.6	5.2
3C58	-	-	2.6	2.91?
W50	SS433	-	5.5	?

Table 2.2: Principal plerions [105].

of the seven EGRET pulsars (the Crab pulsar, the Vela pulsar, PSR 1951 + 32 and PSR 0656 + 14) are included in the plerions. Of these, VHE gamma rays have already been detected from the Crab nebula, and the other three plerions are also strong candidates for VHE gamma-ray sources because they are fed great energies by their pulsars. SNR 0540 − 69, which is in the Large Magellanic Cloud, most closely resembles the Crab nebula and has been called the 'twin' of the Crab nebula. However, if it has the same luminosity in the VHE region, its flux will be reduced by more than a factor of 700 because of the greater distance.

2.3.4 Active Galactic Nuclei (AGNs)

Acceleration of high energy particles is thought to take place in Active Galactic Nuclei (AGNs), which is located in the center of active galaxies. Intense continuum radiation has been observed from AGNs at optical, radio and X-ray wavelengths which is variable on a time-scale of weeks and months. Since causality requires the dimensions of the emitting volume to be $r \lesssim c\tau$, where τ is the time-scale of the variability, this continuum emission must originate within a very compact region, $r \lesssim 0.1$ pc. Some AGNs have broad emission lines, which implies the existence of very high velocity gas motions. In a few cases, radio jets are observed extending from the nucleus. AGNs are classified by their observed profiles as follows:

Seyfert galaxy: The galaxies in this category were first listed by Seyfert in 1943. Many strong emission lines are observed in their spectra. They are further classified into two types (Seyfert I and Seyfert II) owing to their emission line profile. Most of Seyfert galaxies are classified morphologically as spirals.

Blazar: Compared with Seyfert galaxy, no remarkable emission lines are in the spectrum of blazars, and their continuum emission is highly polarized. Jets are thought to be ejected from blazars to the direction of the earth. BL Lac objects and OVV (Optically Violent Variable) Quasars belong to this category.

Radio galaxy: Most of elliptical galaxies are not observable at radio wavelengths, but a few of them are strong radio sources. They are called radio galaxies.

Quasar: The spectrum profile of quasars is similar to Seyfert I galaxy, but quasars have very high redshifts up to $z \sim 4$. Some of them are also bright at radio wavelengths (radio loud quasar).

The central compact object of AGN is assumed to be a massive black hole ($10^6 \sim 10^{10} M_\odot$ [69]) and recent observations at optical, radio and X-ray wavelengths support the existence of massive black holes in some active galaxies [43, 52, 78, 112]. On the basis of the assumption of the presence of a massive black hole and its accretion disk, a model to interpret observed profiles of AGNs in a unified scheme is proposed by some authors [3, 7].

Of the about 500 AGNs [39], the two BL Lac objects, Markarian 421 [91] and Markarian 501 [93], have been identified as VHE gamma-ray sources so far. Of particular interest, a

TeV/X-ray flare from Markarian 421 was detected in May of 1994 by the Whipple Observatory and the X-ray satellite ASCA [72]. The authors have explained the VHE gamma-ray emission due to inverse Compton scattering in the SSC model. Blazars and quasars are classified as more active than the other AGNs, and Markarian 421 and Markarian 501 are the most nearby blazars (their redshifts are 0.031 and 0.034, respectively [27]). It is suggested that VHE gamma-ray emission from distant AGNs is less observable since the gamma rays are absorbed in the intergalactic infrared radiation field (IIRF) [32, 109]. A gamma ray of energy ϵ_1 can pair-produce interacting with a photon of energy ϵ_2, if ϵ_1 is greater than a threshold value, ϵ_t, given by

$$\epsilon_t = \frac{2m^2c^4}{\epsilon_2(1-\cos\theta)}, \tag{2.15}$$

where m is the mass of the produced particles and θ is the angle between the photon trajectories. Restricting attention to electrons and the case of head-on collisions, we have

$$\epsilon_t = 0.26 \times 10^{12}/\epsilon_2, \tag{2.16}$$

where the energies are in eV. Infrared radiation fields are important for VHE gamma rays because

$$\epsilon_2 \sim \frac{2m^2c^4}{\epsilon_t} \sim 0.5 \left(\frac{\epsilon_t}{1\ \mathrm{TeV}}\right)^{-1}\ \mathrm{eV}. \tag{2.17}$$

This absorption of VHE gamma rays in the IIRF seems to be plausible taking into account that VHE gamma rays have been detected from only the two nearby BL Lac objects in spite of about 40 AGNs having been identified in the HE region [119] and some distant AGNs are brighter than the two BL Lac objects at 100 MeV. The magnitude of the IIRF is important in investigating the evolution of galaxies [108] but is difficult to be separated in direct observations from Galactic foreground radiation and the zodiacal light in the solar system. The IIRF can, however, be probed by investigating spectral cutoffs of AGNs above 10 GeV [17, 32]. Furthermore, if several AGNs are seen to have spectral cutoffs consistent with IIRF extinction, it may be possible that the Hubble constant is determined with better accuracy, say, with an error of about 10 % [102]. There exists a completely unexplored energy window between satellite and ground-based experiments from 10 to 200 GeV at present, and the spectral cutoffs of most of the AGNs detected by EGRET must be in this energy window. Several ground-based gamma-ray telescopes having reduced energy thresholds (50 $\sim$ 100 GeV) are currently planned or under construction [86, 114].

Chapter 3

The Vela Pulsar and the Vela SNR

3.1 The Vela Pulsar

The Vela pulsar, PSR 0833 – 45, is a young ($\sim 10^4$ year) nearby ($\sim$ 500 pc) pulsar, which was first discovered as a radio pulsar in 1968 [67]. Its pulsed radiation, with a short period of about 89 msec and a relatively large $\dot{P}$, is observed at radio, optical, X-ray and gamma-ray wavelengths. Figure 3.1 shows its pulsed profile which differs between the wavelength bands [20], unlike the case of the Crab pulsar which is often compared with the Vela pulsar. The radio signal shows a strong single peak, while double peaked profiles are seen at optical [123] and gamma-ray [60, 117] wavelengths, although the phases of the peaks are not coincident. Its recently discovered X-ray pulse also seems to have a different profile from the others [83].

The Vela pulsar has the second highest spindown luminosity at the earth ($\dot{E}/d^2$) of the known radio pulsars (the Crab pulsar is the first). "Glitches", which are discontinuities in the regular change of period of the pulsar, have been observed in the Vela pulsar every 2 or 3 years. The proper motion of the pulsar has been measured to be 49 marcsec yr^{-1} at a position angle of 305° [8], and this direction is almost perpendicular to the pulsar rotation axis [73].

At the HE gamma-ray band, the Vela pulsar is the brightest discrete object in the sky [39]. Its HE gamma-ray emission is 100 % pulsed and upper limits for the unpulsed emission

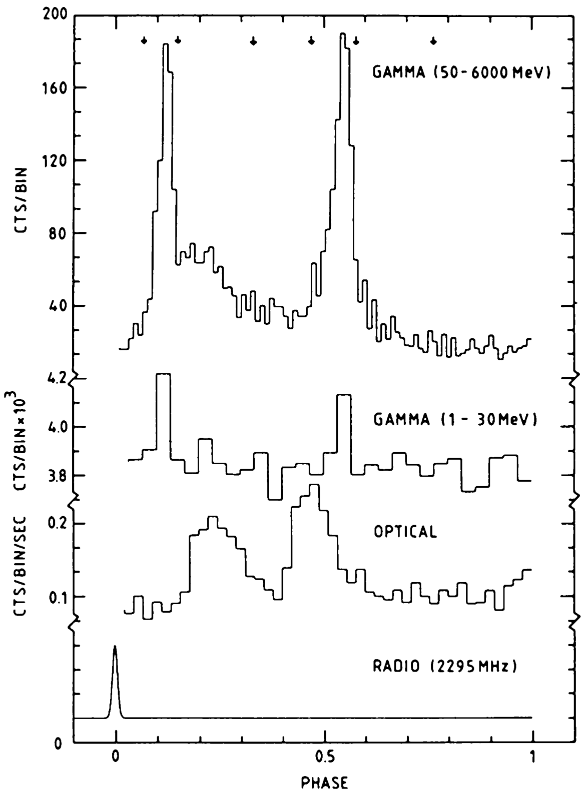

Figure 3.1: The lightcurve from the Vela pulsar at radio, optical, soft gamma rays and high energy gamma rays [48].

have been given from recent observations with EGRET [60]. As shown in Figure 3.2, the spectrum of the pulsed emission is well represented by a single power law of the differential index -1.70 up to 4 GeV. If this spectrum is extrapolated to the VHE range, the expected flux around 1 TeV is well beyond the sensitivity of the 3.8 m telescope. However, a spectral break is apparent at energies above a few GeV.

In the outer gap model described in Chapter 2, the Vela pulsar is in the category of Vela-like pulsars, as the name shows. Cheng, Ho and Ruderman have suggested that VHE gamma rays can be emitted from the outer gaps of the Vela pulsar via inverse Compton scattering up to the energy of about 6×10^{12} eV [25]. They have also shown that the ratio of

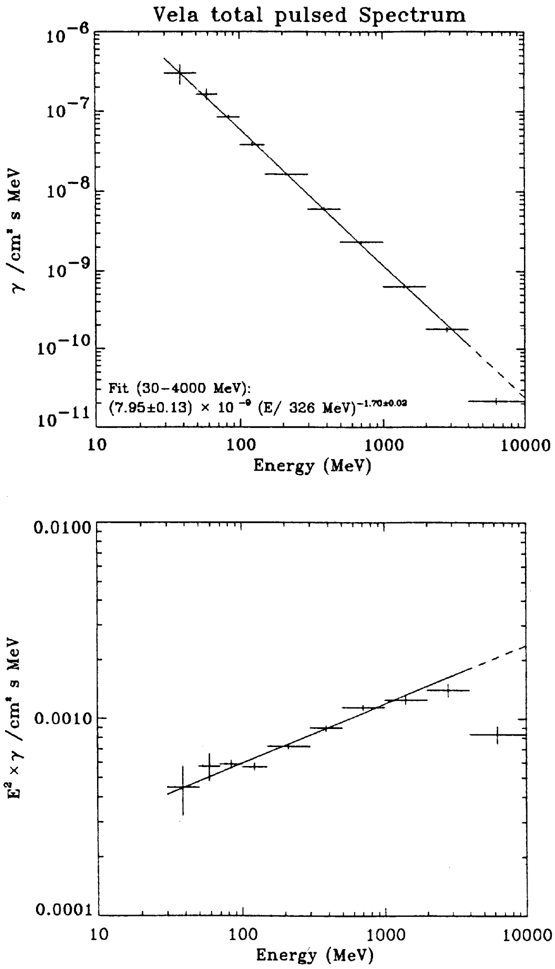

Figure 3.2: The spectrum of the pulsed HE gamma-ray emission from the Vela pulsar detected by EGRET [60]. A spectral break is apparent at energies above a few GeV.

inverse Compton loss to synchrotron loss by secondary electrons and positrons is $\sim 10^{-2}$ and the total radiated power from the Vela outer gaps is $\sim 3 \times 10^{-2}\dot{E}$, where $\dot{E}$ is the spindown luminosity. Thus, it has been predicted in the outer gap model that the power of $\sim 3\times10^{-4}\dot{E}$ is radiated into the VHE region.

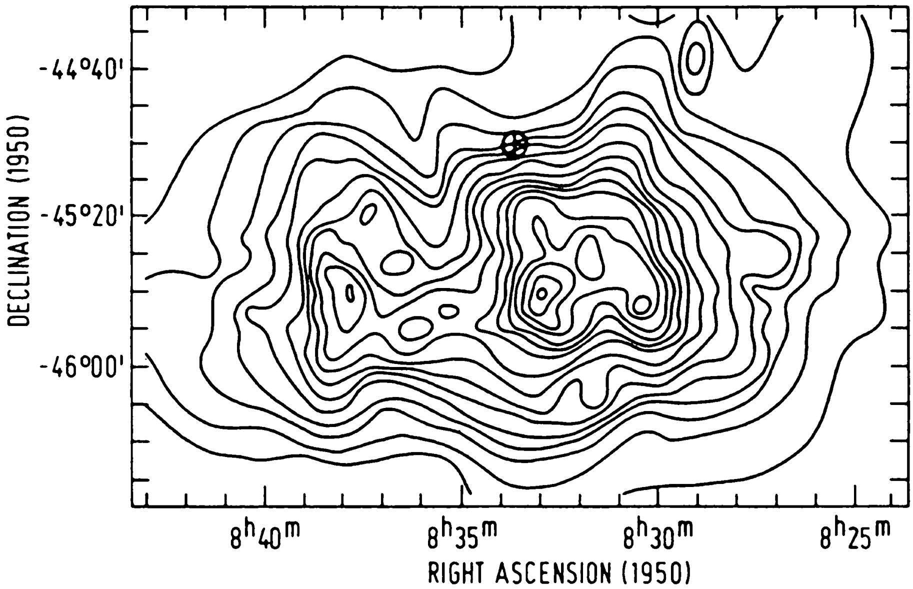

Figure 3.3: A radio contour map of Vela X at radio wavelength $\lambda = 11.3$ cm showing the position of the Vela pulsar ($\oplus$) [127]. Vela YZ are outside of this map.

3.2 The Vela SNR

The Vela pulsar is located almost at the center of the Vela supernova remnant, which has a shell structure of 8°.3 diameter [6]. The Vela SNR includes the strong radio sources Vela XYZ. Vela X, of which the radio map is shown in Figure 3.3, is the brightest of these and is located about 1° from the pulsar to the south-southwest. Vela X is sometimes classified as a plerion owing to the pulsar-SNR association and is thought to be powered by the Vela pulsar [127].

At X-ray wavelengths, a strong pointlike DC source exists at the pulsar position [53, 84, 128], although its pulsed signal is weak. In the soft X-ray band (about a few keV), a compact nebula with a few arcmin radius appears around the pulsar [53, 84]. Furthermore, recent observations by the Rosat X-ray telescope revealed a jet of diffuse emission which

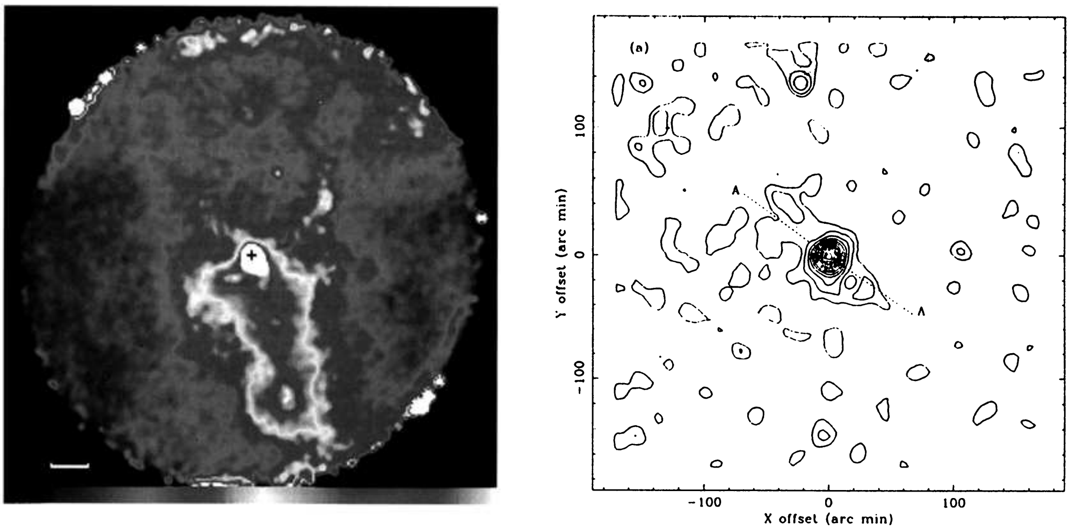

Figure 3.4: X-ray maps around the Vela pulsar. The left is a soft X-ray image (0.9 $\sim$ 2.0 keV) observed with the Rosat X-ray telescope [74]. The horizontal bar is 10 arcmin long. The right is a hard X-ray contour map (2.5 $\sim$ 10 keV) observed with the University of Birmingham coded mask telescope flown on the Spacelab 2 [128]. The line AA gives the orientation of the pulsar spin axis suggested by Manchester [73].

originates at the pulsar and extends in the direction of Vela X (see the left of Figure 3.4). Markwardt and Ögelman suggested that the total emitted luminosity in 0.7 $\sim$ 2.4 keV is $\sim 10^{-33}$ erg sec^{-1}. Almost half of the pulsar spindown energy is spent in driving the jet if their thermal plasma model is correct [74] and Vela X, which is coincident with the end of the jet, is due to radio synchrotron emission from the electrons shock-accelerated by the sudden jet termination. On the other hand in the hard X-ray band (about a few tens of keV), diffuse emission extending about 1° to both the northeast and the southwest appears around the pulsar and this elongation is roughly aligned with the pulsar rotation axis. Willmore et al. suggested this elongated region is a synchrotron nebula [128]. This pulsar-nebula association reminds us of the case of the Crab pulsar and nebula.

Features	Crab	Vela
Lightcurve (HE gamma ray)	double peak	double peak
Lightcurves at different wavelengths	similar	different
Continuous emission (HE gamma ray)	yes	upper limit
Synchrotron nebula	yes	yes
Jet (X-ray)	yes	yes
Counter jet (X-ray)	yes	?
VHE gamma-ray emission	yes (unpulsed)	?

Table 3.1: Principal observed features of the Crab and Vela pulsars/nebulae.

3.3 Comparison with the Crab Pulsar and Nebula

The Crab pulsar and the Vela pulsar are the two main prototypical pulsars and their features are often compared including their nebulae or SNR associations. The comparison is a convenient way to emphasize their characteristics.

The two pulsars have the largest two values of the spindown luminosity among all of the known pulsars. Both the Crab nebula and Vela X are classified as plerions. The HE gamma-ray lightcurve of the Crab pulsar is double-peaked as in the case of the Vela pulsar, but lightcurves of the Crab pulsar in the other wavelengths have almost the same double-peaked profiles [124]. In the HE gamma-ray region, continuous emission is also detected from the direction of the Crab pulsar, unlike the case of the Vela pulsar, and this is known to be the contribution from the nebula [82]. At X-ray wavelengths, an X-ray emitting jet is ejected from the Crab pulsar like the case of the Vela pulsar, and it is aligned with the pulsar rotation axis [55]. However, the existence of a counter jet has not been confirmed in the case of the Vela pulsar unlike the Crab. As described in Chapter 2, the Crab nebula has been confirmed as a VHE gamma-ray source by many groups, but pulsed emission has not been detected from the Crab pulsar. The above features are summarized in Table 3.1.

As reviewed above, the observed features around the Vela pulsar are very complicated. We can find several promising features for the generation of VHE gamma rays in the region near the pulsar: the jet, the synchrotron nebula, the material of the SNR and of course the pulsar itself. Therefore, there is no doubt that the Vela SNR, including the pulsar, is a strong candidate VHE gamma-ray source, but it is possible that VHE gamma rays are emitted from different regions away from the pulsar because several extended structures are seen a few degrees from the pulsar. If a VHE gamma-ray signal is detected, the position and the size of the source are important parameters for an understanding of the physical phenomena around the pulsar. The CANGAROO 3.8 m telescope has the finest-pixel imaging camera of the current experiments as mentioned in Chapter 4 and it is adequate to determine the position and the size of the VHE gamma-ray source precisely.

3.4 Previous VHE Gamma-Ray Observations

The Vela pulsar is a strong candidate for a VHE gamma-ray source as mentioned above and has been a high priority object in southern hemisphere VHE gamma-ray observations. Previous observations of VHE gamma rays from the Vela pulsar are summarized in Table 3.2.

Positive observations of VHE gamma rays from the Vela pulsar have been reported by two groups so far. Grindlay et al. detected a pulsed signal from the Vela pulsar at the 4 σ level. The signal showed a single peaked lightcurve and the peak was seen 3 msec before the radio pulse [49]. However, they couldn't confirm their result by their further observations and concluded there was no evidence for pulsed emission. The Tata group also reported the detection of VHE gamma rays from the pulsar. The 1979 data set showed evidence for a double peaked lightcurve [15], while only a single peak was found in the data between 1982 and 1985 [16]. Absolute phase was not known for the 1979 observations, but it was available during the latter observations. They noted the single peak was close to the phase of the first optical peak. However, pulsed emission from the Vela pulsar has not been detected in the

Group	Site	Year	Energy (TeV)	Flux (10^{-12} cm^{-2} sec^{-1})	Lightcurve	Reference
Sydney	Narrabri	1972	0.3	10 ± 3.3	single peak	[49]
Sydney	Narrabri	1973	5	0.7 ± 0.3	single peak	[49]
Sydney	Narrabri	1974	0.3	< 20		[49]
Tata	Ooty	1979	10.4	15 ± 3	double peak	[15]
Tata	Ooty	1979 ~ 1980	9.3	< 0.2		[16]
Tata	Ooty	1982 ~ 1983	4.7	1.1 ± 0.3	single peak	[16]
Tata	Ooty	1984 ~ 1985	5.4	1.0 ± 0.3	single peak	[16]
Adelaide	White Cliffs	1986	5	< 58		[28]
Durham	Narrabri	1987	0.3	$< 60 \pm 15$		[19]
Potchefstroom	Nooitgedacht	1989	2	< 17		[80]
Potchefstroom	Nooitgedacht	1992	2.3	< 6		[81]
Adelaide	Woomera	1989 ~ 1992	0.8	< 67		[33]

Table 3.2: Previous observations of VHE gamma rays from the Vela pulsar.

recent observations by other groups [19, 28, 33, 80, 81], and the results of the Tata group have not been confirmed yet.

One should note that, with the exception of a short subset of Grindlay et al.'s data, *only pulsed and transient emission has been searched for in the previous VHE gamma-ray observations of the Vela pulsar.* Our 3.8 m telescope using the atmospheric Čerenkov imaging technique can detect DC gamma-ray emission and it is possible that VHE gamma rays are steadily being emitted from the vicinity of the Vela pulsar taking into account its similarities with the Crab.

Chapter 4

Atmospheric Čerenkov Technique

4.1 Overview

As mentioned in Chapter 2, VHE gamma rays are detected using atmospheric Čerenkov telescopes. Charged particles in EASs initiated by VHE gamma rays lose their energies in ionizing atmospheric nuclei and most of them are attenuated in the atmosphere before arriving at the ground. However, the atmosphere is quite transparent for Čerenkov light radiated from charged particles in EASs. "Čerenkov observations" are possible only on moonless clear nights because of the low intensity of Čerenkov light, and the use of reflectors is necessary to collect Čerenkov photons. The Čerenkov observation has the advantage of the large gamma-ray detection area, which is about 10^4 times larger than the typical area in satellite detection.

Atmospheric Čerenkov telescopes detect not only gamma rays but also the numerous backgrounds due to cosmic-ray nuclei. Therefore, it is important to eliminate background events for effective detections of gamma rays. Fortunately, there are several important differences in the development between EASs initiated by gamma rays ("gamma-ray showers") and EASs initiated by cosmic-ray nuclei ("hadronic showers"), and differences in the Čerenkov light profile can be used to differentiate between them and enhance gamma-ray signals.

There are currently a few kinds of techniques for Čerenkov observation. Of these, the "imaging technique" is the most powerful for rejecting background events. In this technique, Čerenkov images on the focal plane are recorded with an imaging camera consisting of many photomultiplier tubes (PMTs), and the images well reflect the profile of the development of the EAS because Čerenkov photons are radiated within a cone of about 1° with respect to the shower axis. Imaging telescopes have an angular resolution as good as 0°.1 and this is an epoch-making improvement in the signal-to-noise ratio comparing the angular resolution of $\sim 1°$ in non-imaging telescopes.

4.2 Extensive Air Showers

A gamma ray entering the earth's atmosphere initiates an electromagnetic cascade. In the electromagnetic cascade, electrons, positrons and gamma rays increase via pair production and bremsstrahlung. The energy of the primary gamma ray is divided into particles in the cascade and the average particle energy decreases as the cascade proceeds. Finally, ionization loss becomes dominant for the particles and the cascade will decay.

On the other hand, a primary cosmic-ray nucleus entering the atmosphere interacts with an atmospheric nucleus and generates a nuclear cascade. A nuclear interaction causes multi-particle production, in which secondary nucleons and mesons are produced. Pions constitute the greatest fraction of nucleonic cascade particles. Neutral pions decay into gamma rays as $\pi^0 \to 2\gamma$ (Chapter 2) and electromagnetic cascades are produced by the gamma rays as mentioned above. Since the lifetime of charged pion is $2.603 \times 10^{-8}\gamma_\pi$ sec, where γ_π is the Lorentz factor of the charged pion, and the mean free path for charged pion in the atmosphere is ~ 80 g cm^{-2}, charged pions of the energies well greater than 10 GeV further interact with atmospheric nuclei, while the others decay as follows;

$$\pi^+ \to \mu^+ + \nu_\mu, \tag{4.1}$$

$$\pi^- \to \mu^- + \overline{\nu}_\mu. \tag{4.2}$$

The high energy muons generated in the early stage of the development of the EAS can

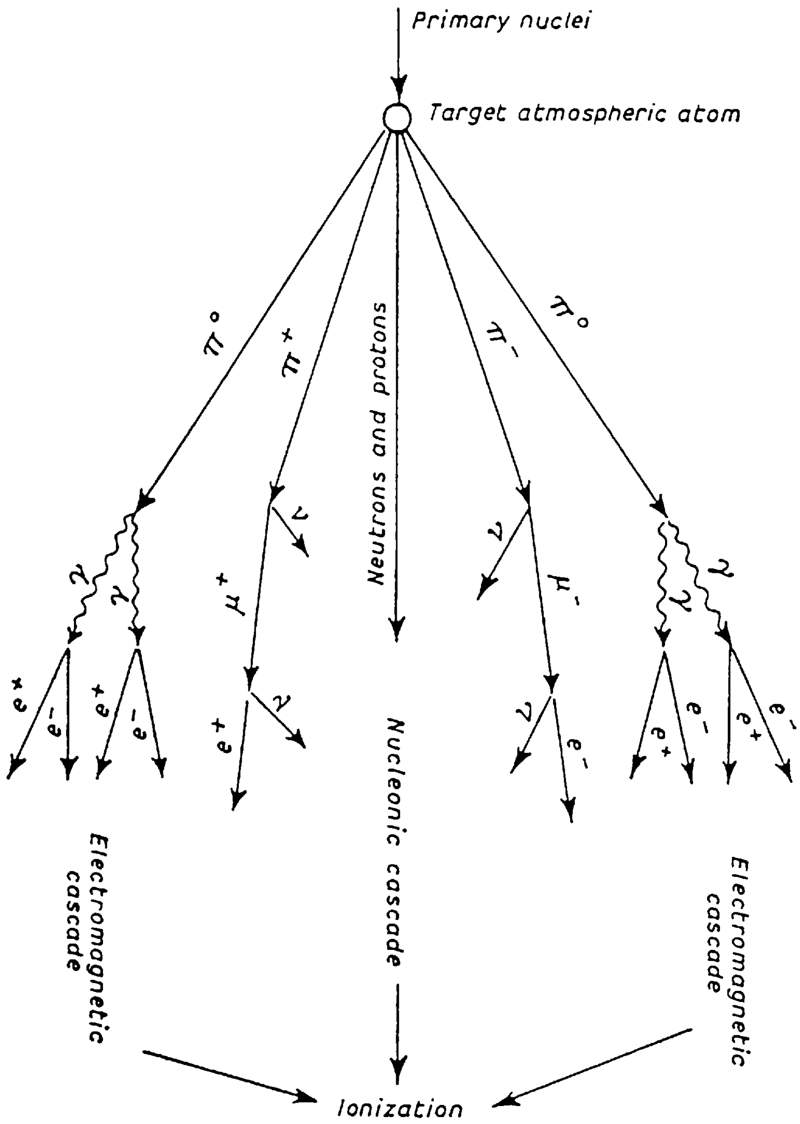

Figure 4.1: Basic elements in the development of the EAS [124].

come to the ground without decaying (the lifetime of muon is $2.197 \times 10^{-6}\gamma_\mu$ sec). The above elements in the development of the EAS are summarized in Figure 4.1.

There are several important differences in the development of EASs between gamma-ray showers and hadronic showers. First, hadronic showers develop later (lower in the atmosphere) because of the longer interaction length. Second, nuclear cascades have larger transverse momenta than electromagnetic cascades and, as a result, hadronic showers are more extended transversely than gamma-ray showers as shown in Figure 4.2. These two facts also mean there are larger fluctuations in the development of hadronic showers. Third, comparing at the same energy of the primary particle, the number of particles in an EAS is roughly one third as many in hadronic showers because pions of all charges are produced in almost equal numbers in multiparticle production, and hadronic showers have more muons.

4.3 Čerenkov Radiation

In a medium of a refractive index n, the velocity of light is $c' = c/n$, where c is the velocity of light in a vacuum. A charged particle which is moving at a velocity $v > c'$ in the medium radiates Čerenkov radiation. The radiation is only permitted at a particular angle θ ("Čerenkov angle") with respect to the track of the particle;

$$\cos\theta = \frac{1}{\beta n}, \tag{4.3}$$

where $\beta = v/c$. For the wavelength 400 nm, The refractive index of air at temperature T K can be expressed as;

$$n = 1.0 + 0.000296 \left(\frac{x}{1030 \text{ g cm}^{-2}}\right)\left(\frac{T}{273.2 \text{ K}}\right)^{-1}, \tag{4.4}$$

where x g cm^{-2} is the atmospheric depth and T is written as $T = 204 + 0.091x$ [57]. Since $n \sim 1.00027$ at 1 atm, the Čerenkov angle is $\theta \leq 1^\circ.3$ for relativistic particles ($\beta \sim 1$) in an EAS from (4.3). Therefore Čerenkov radiation from the EAS is radiated in a few degrees with respect to the shower axis.

The energy output of Čerenkov radiation per unit path is represented by the following equation;

$$\frac{dE}{dl} = \frac{Z^2e^2}{c^2}\int_{\beta n>1}\left(1 - \frac{1}{\beta^2 n^2}\right)\omega d\omega, \tag{4.5}$$

where Ze is the particle charge and ω is the frequency of Čerenkov radiation [59]. From

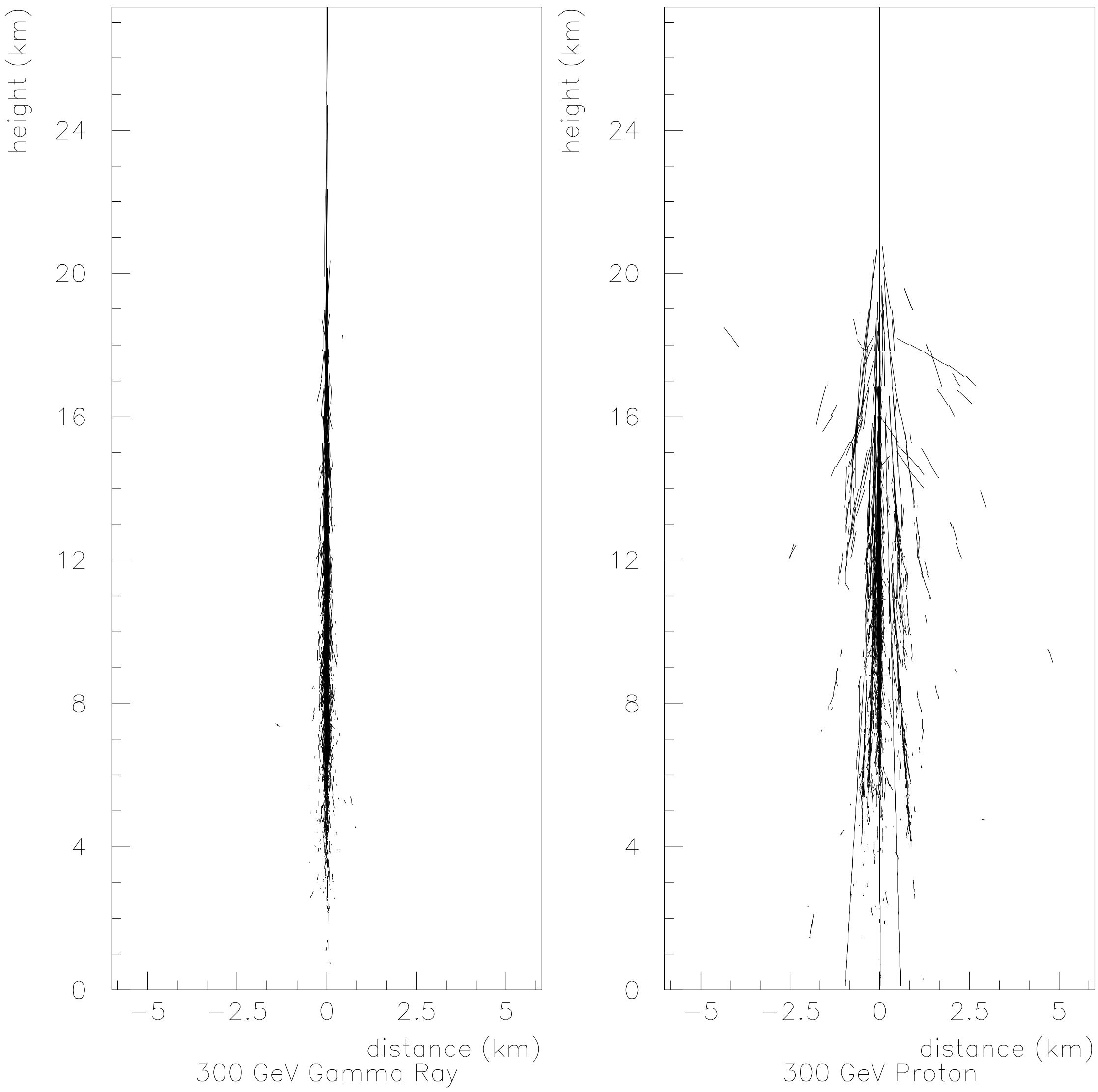

Figure 4.2: Development profiles of Monte Carlo simulated EASs from a 300 GeV gamma ray (left) and a 300 GeV proton (right).

(4.5), the number of photons radiated into the wavelength range between λ_1 and λ_2 is

$$N = 2\pi\alpha Z^2 l \left(\frac{1}{\lambda_1} - \frac{1}{\lambda_2}\right)\left(1 - \frac{1}{\beta^2 n^2}\right), \tag{4.6}$$

where $\alpha = e^2/\hbar c$ is the fine structure constant. The total number of Čerenkov photons radiated from an EAS is proportional to number of electrons in the EAS, and therefore, from the above mentioned, the number of Čerenkov photons from a gamma-ray shower is three times more than that from a hadronic shower. The lateral distribution of Čerenkov light initiated by a gamma ray is almost flat out to a ~ 150 m radius at sea level and the detection area is the order of 10^4 m^2, which is much larger than the typical area of 1 m^2 in satellite detection. Moreover, the Čerenkov photon density detected at sea level is a good estimator for the primary gamma-ray energy. Some of the Čerenkov photons are Rayleigh or Mie scattered in the atmosphere before arriving on the ground [11], and the number of Čerenkov photons from an EAS initiated by a 1 TeV primary gamma ray is only $20 \sim 50$ m^{-2} in $350 \sim 550$ nm at sea level. Therefore, it is necessary for the efficient detection of VHE gamma rays to use reflectors collecting Čerenkov photons from the EAS.

4.4 Atmospheric Čerenkov Imaging Technique

The gamma-ray flux from a strong source, such as the Crab nebula, is $\sim 10^{-11}$ cm^{-2} sec^{-1} above 1 TeV, while The cosmic-ray (background) flux is $\sim 10^{-5}$ cm^{-2} sec^{-1} str^{-1} above 1 TeV. Assuming an effective field of view of a telescope being 10^{-3} str ($\sim 1°$ radius), the signal-to-noise ratio in the detected events is $\sim 10^{-3}$. Therefore, it is necessary to eliminate background events for efficient detection of gamma rays. Non-imaging telescopes before developing the imaging technique had an angular resolution of $\sim 1°$ and no background rejection technique. However, the angular resolution in the imaging technique is $\sim 0°.1$, thus the signal-to-noise ratio in the imaging technique is about 10^2 times better than that of non-imaging telescopes, considering only the angular resolution.

The imaging Čerenkov observation is schematically shown in Figure 4.3. Čerenkov pho-

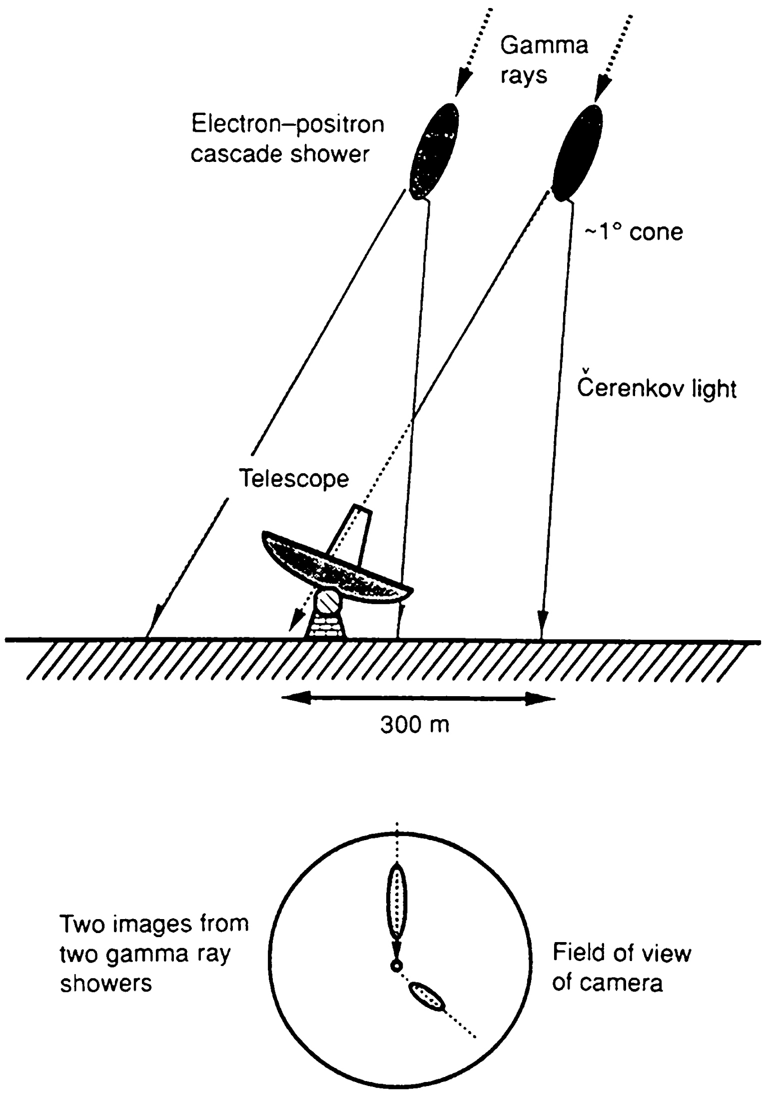

Figure 4.3: The principle of detecting gamma rays through the Čerenkov imaging technique. The image of the light measured with the telescope basically represents the shape of the electron-positron cascade, which is elongated along the shower axis in the direction to the object at which the telescope is aimed [64].

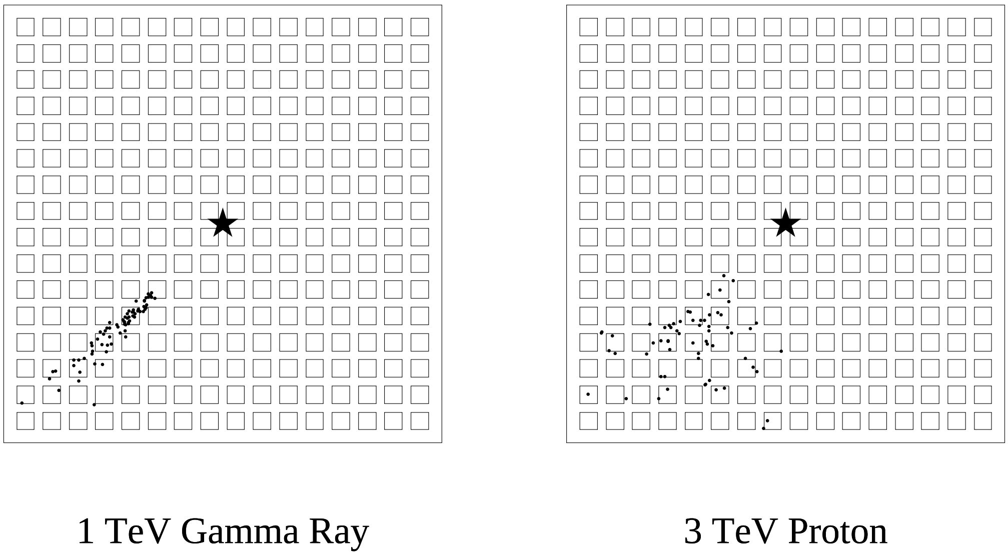

Figure 4.4: Typical Čerenkov images of a 1 TeV gamma ray (left) and a 3 TeV proton (right). The dots represent the positions of Čerenkov photons on the focal plane and photons are detected by an array of PMTs. The source is located at the center of the field of view ($\star$) for both pictures. The large squares represent fields of $3^\circ \times 3^\circ$.

tons collected with a reflector make an image on the focal plane. The image is considered to be a projection of the shower development onto the focal plane and represents the shape of the electron-positron cascade, which is elongated along the shower axis parallel to the direction to the object at which the telescope is aimed. As a result, Čerenkov images of gamma rays ("gamma-ray images") elongate to the source in the field of view. On the other hand, Čerenkov images due to cosmic-ray nuclei ("hadronic images") have random directions in the field of view reflecting the random primary directions of the nuclei and the irregularity of the shower development.

In the imaging technique, images are detected by an imaging camera consisting of many

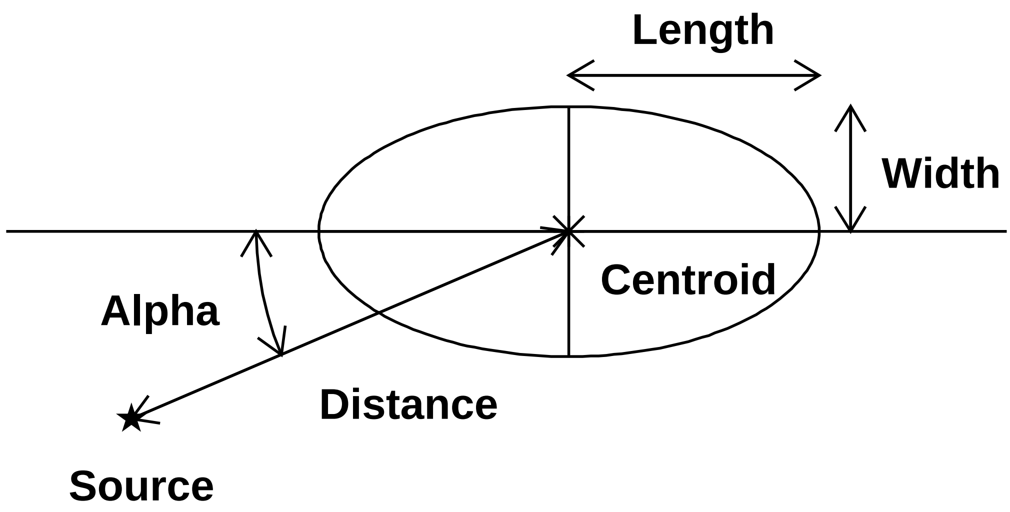

Figure 4.5: Definition of image parameters.

PMTs, as shown in Figure 4.4. Hillas (1985) has shown that a parameterization based on fitting an ellipse to the Čerenkov images is effective in extracting the characteristics required to enhance gamma-ray signals [58]. The image parameters generally used in the imaging technique are schematically shown in Figure 4.5, where:

Width: The rms spread of light along the minor axis of the image; a measure of the lateral development of the cascade.

Length: The rms spread of light along the major axis of the image; a measure of the vertical development of the cascade.

Distance: The distance between the centroid of the image and the source position.

Conc: The degree of light concentration as determined from the ratio of the two largest tube signals to the sum of all signals.

Alpha: The angle between the major axis and a line joining the centroid of the image to the source.

The simulated distributions of the above parameters for primary gamma rays and primary protons are shown in Figure 4.6. The Monte Carlo simulation has been done assuming the primary directions to be of a point source for gamma rays while isotropic for protons. As one can expect from the above, hadronic images should generally be broader in Width, longer in Length and lower in Conc owing to the irregular, wide-spread development of their showers. These image parameters are called "shape parameters". Also Alpha values of gamma-ray images should be concentrated near Alpha = 0°, while Alpha values of hadronic images should be uniform. Alpha is called an "orientation parameter". The above features can indeed be seen in Figure 4.6. The good angular resolution of the imaging technique is due to the strong directionality of gamma-ray images as seen in the Alpha distribution of Figure 4.6.

Telescopes for the imaging Čerenkov observation are generally operated by two observation methods. They are "on/off tracking" and "continuous tracking". Even if many background events are successfully eliminated using the above image parameters, it is impossible to completely eliminate all of them because of the large fluctuation of hadronic showers. In the on/off tracking method, an off-source observation with no prior gamma-ray source in the field of view is done night by night under the almost same conditions as the on-source observation. The off-source data are used to estimate background counts in the imaging technique, and a DC gamma-ray signal from a source can be evaluated subtracting the off-source counts from the on-source counts. On the other hand, the continuous tracking method is not generally used to detect DC signals, and the data are usually used to search for periodic emission or bursts from a source. If DC gamma-ray signals can be detected effectively without any off-source observation, continuous source tracking has the advantage of two times longer exposure time than on/off tracking. New methods to evaluate a DC signal without any off-source observation have recently been proposed by some authors [22, 41, 63], and it may be possible in the near future.

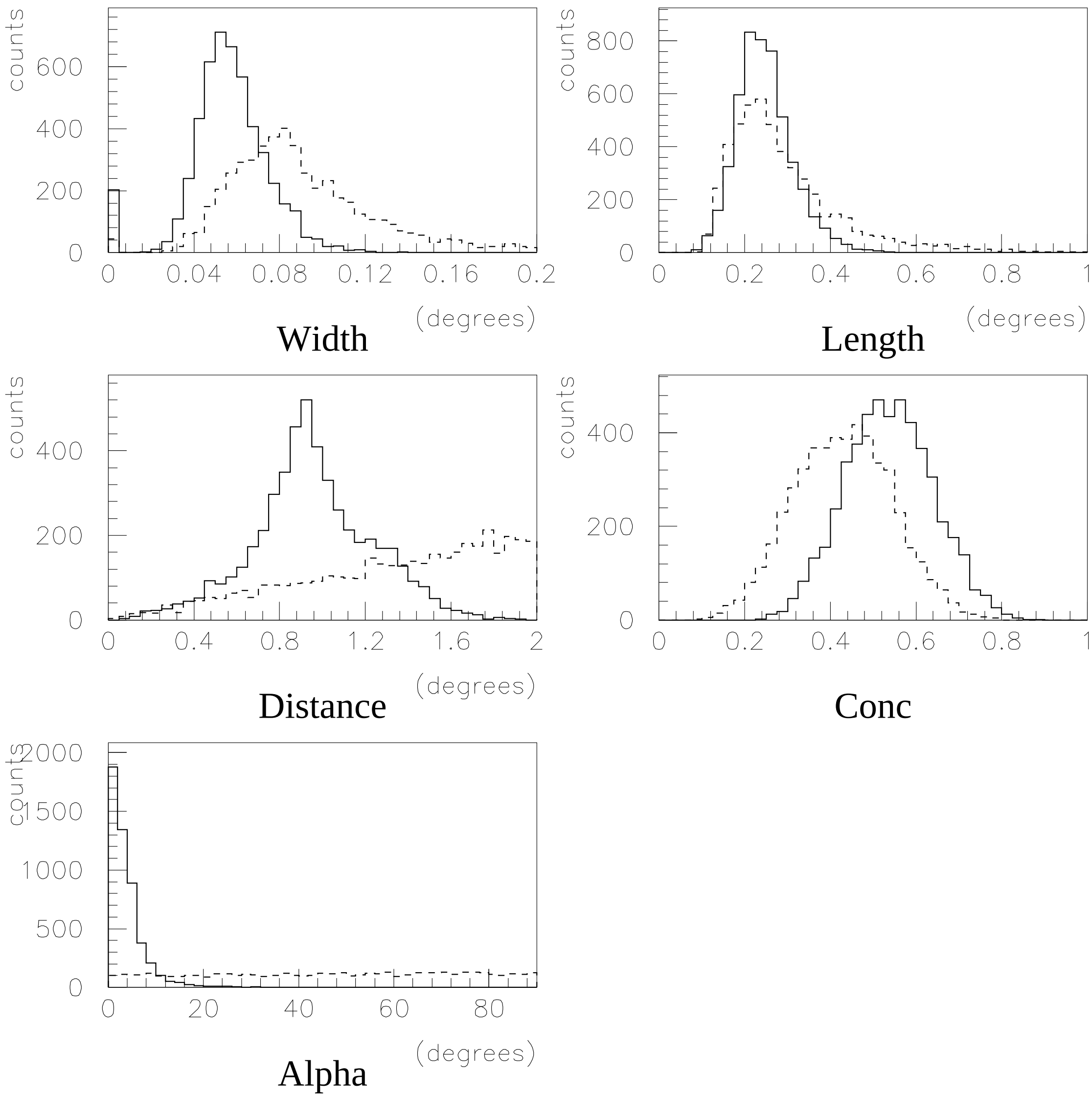

Figure 4.6: Image parameter distributions predicted by simulation for an on-axis gamma-ray source at the zenith and an isotropic background of protons. The solid lines in the figures represent distributions of gamma-ray images and the dashed lines are of proton images. The simulation has been done using the same telescope and the same PMTs as the CANGAROO 3.8 m telescope, but much more PMTs have been arrayed on the focal plane to eliminate edge effects of the imaging camera (see Chapter 7).

Group	Location	Reflectors	Cameras
CANGAROO	Woomera, Australia (137°E, 31°S)	11.2 and 12.6 m^2	256 and 37 pixels
CAO	Crimea, Ukraine (34°E, 45°N)	13.5 $m^2 \times 2$	37 pixels $\times$ 2
Durham	Narrabri, Australia (150°E, 30°S)	42 m^2	109 pixels
HEGRA	La Palma, Canaries (18°W, 29°N)	8.5 and 5.0 m^2	61 and 37 pixels
Whipple	Mount Hopkins, USA (111°W, 32°N)	11 and 10 m[a]	109 pixels $\times$ 2

[a] Diameters.

Table 4.1: Current experiments using the imaging technique.

Current experiments using the imaging technique are summarized in Table 4.1. The pioneer in the imaging technique is the Whipple group. They succeeded in eliminating more than 99 % of the background events in their analysis [92, 98]. The Whipple telescopes have the largest reflectors (10 and 11 m diameters) of the current telescopes and the lowest energy threshold (200 GeV). They have discovered three VHE gamma-ray sources so far (Crab nebula [125, 122], Markarian 421 [91] and Markarian 501 [93]). Their results for the Crab nebula and Markarian 421 are shown with Alpha plots in Figure 4.7. The Crab nebula and Markarian 421 have also been observed by the HEGRA group [65, 88]. They have two imaging telescopes at present and are planning to do stereoscopic observations with five imaging telescopes. The Japanese telescope of the CANGAROO group has the finest-pixel imaging camera with 256 PMTs at present [50]. A radio and gamma-ray (100 MeV) pulsar PSR $1706-44$ was identified as a VHE gamma-ray source by the CANGAROO group [63]. The Alpha distributions for PSR $1706-44$ reported by the CANGAROO group are shown in Figure 4.8. The fine-pixel imaging camera can detect more detailed structure of Čerenkov images and makes more sensitive gamma-ray detection possible. The fine-pixel imaging telescope of the CAT group (588 pixels) is under construction at present, and will start operation at the beginning of 1996 [29].

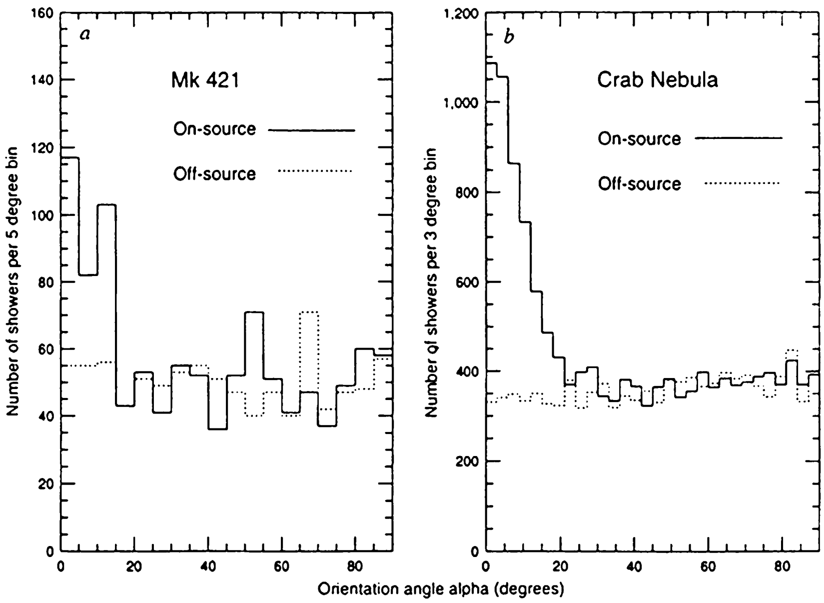

Figure 4.7: Alpha distributions for the Crab nebula and Markarian 421 reported by the Whipple group [91].

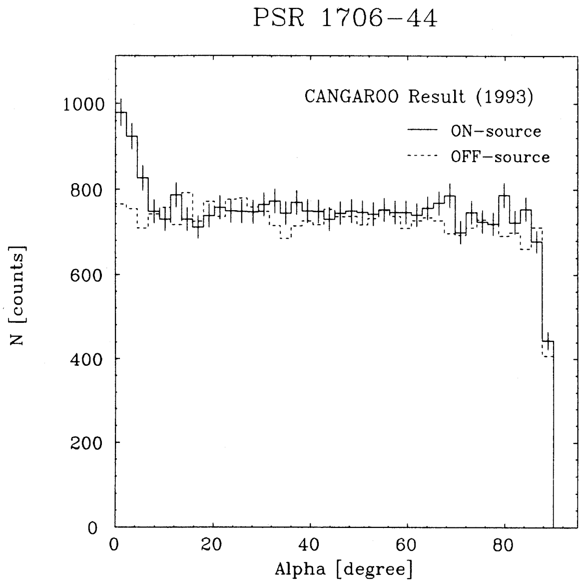

Figure 4.8: Alpha distributions for PSR 1706 − 44 reported by the CANGAROO group.

Chapter 5

The CANGAROO 3.8 m Telescope

5.1 The CANGAROO Project

The CANGAROO project is a collaboration between the University of Adelaide and Japanese institutes for VHE gamma-ray observations.[1] Two atmospheric Čerenkov imaging

---

[1] CANGAROO collaboration:

Y. Hayami, F. Kakimoto, S. Ogio, T. Ohsaki, K. Sakurazawa, T. Tanimori, T. Tsukagoshi, T. Yoshikoshi, *Tokyo Institute of Technology*

N. Hayashida, T. Kifune, M.D. Roberts, M. Teshima, *Institute for Cosmic Ray Research, University of Tokyo*

S.A. Dazeley, J.R. Patterson, G.P. Rowell, G.J. Thornton, *University of Adelaide*

Y. Matsubara, T. Matsuoka, Y. Muraki, T. Sako, *Solar-Terrestrial Environment Laboratory, Nagoya University*

H. Katsumata, T. Konishi, S. Oda, T. Suda, A. Suzuki, *Kobe University*

A. Masaike, R. Susukita, *Kyoto University*

T. Hara, *Yamanashi Gakuin University*

M. Fujimoto, T. Mizumoto, *National Astronomical Observatory*

P.G. Edwards, *Institute of Space and Astronautical Science*

T. Tamura, *Kanagawa University*

M. Mori, *Miyagi University of Education*

H. Muraishi, S. Yanagita, T. Yoshida, *Ibaraki University*

H. Fujii, S. Kabe, Y. Watase, *National Laboratory for High Energy Physics* telescopes are located near Woomera, South Australia (longitude 136°47′E, latitude 31°06′S, 160 m a.s.l.). The Japanese 3.8 m telescope [50] is located 100 m to the east of BIGRAT (the BIcentennial Gamma-RAy Telescope). Stereoscopic observations have been done since 1992 using the two telescopes [120, 121].

5.2 The 3.8 m Telescope

5.2.1 The Reflector and Imaging Camera

Figure 5.1 shows the CANGAROO 3.8 m telescope. The reflector of the 3.8 m telescope has a parabolic shape and both its diameter and focal length are 3.8 m. The telescope was originally used for lunar ranging in the National Astronomical Observatory at Mount Dodaira, Japan, about 20 years ago, and its surface quality was designed to have a blur much better than 1 arcmin. The current accuracy after the installation at Woomera is as good as a few arcmin. The reflector is made of aluminized duralumin and is canigen-plated. The current reflectivity of the reflector is about 50 % at 482 nm.

The telescope is mounted on an alt-azimuth mount. Two pulse-counting motors for altitude and azimuth rotations are controlled by a personal computer (NEC PC98), and the use of two encoders gives a tracking accuracy of 0°.01. The motors are going to be replaced with AC-servo motors in January 1996.

The imaging camera consists of 10 mm (3/8 inch) × 10 mm Hamamatsu R2248 square photomultiplier tubes. The photocathode area of the PMT is 8 mm × 8 mm, which corresponds to an angular extent of 0°.12 × 0°.12, and covers about 40 % of the field of view. The photocathode material is bialkali and the quantum efficiency is about 20 % in the range between 350 nm and 550 nm. Additional 32 PMTs were added to the camera in May 1995, and the present camera contains 256 PMTs, which gives a field of view of about 3°.2 in diameter (Figure 5.2). Each group of eight PMTs is installed in a single box (Figure 5.3) and supplied a common preset high voltage. The operation of the PMTs with a low gain

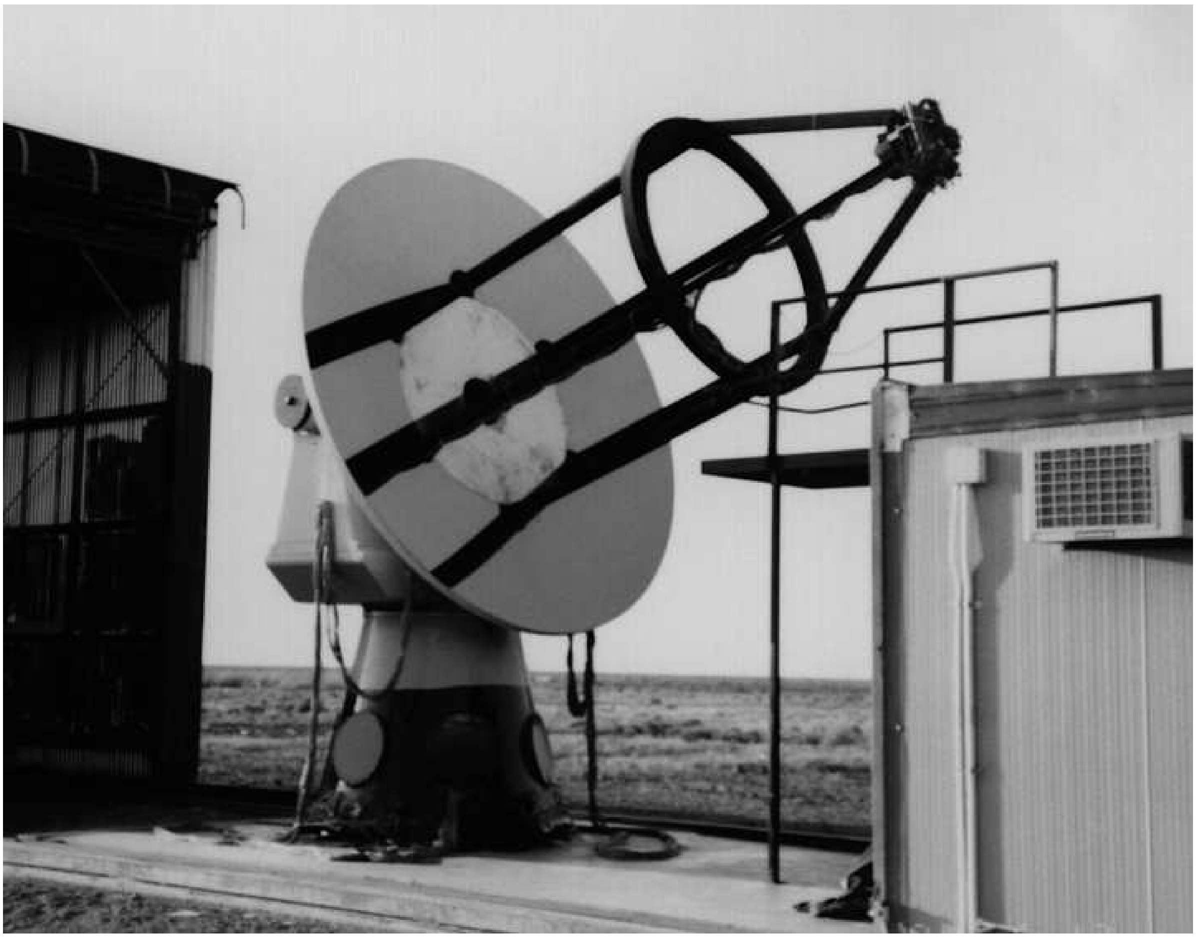

Figure 5.1: The CANGAROO 3.8 m telescope.

($\times \sim 10^5$) is employed in our camera and can reduce the effect of gain variation of the PMTs due to variation of the sky brightness.

A blue light emitting diode (LED, the peak wavelength is 450 nm) is set at the center of the reflector (3.8 m distant from the camera). Blue light pulses of about a 20 nsec width are generated using this LED to calibrate the relative gains of the PMTs.

5.2.2 Electronics and Event Trigger

Outputs of the PMTs are first amplified by buffer amplifiers ($\times 2$) in the high voltage boxes, then are fed into the electronics hut (Figure 5.4) via 30 m long twisted pair cables.

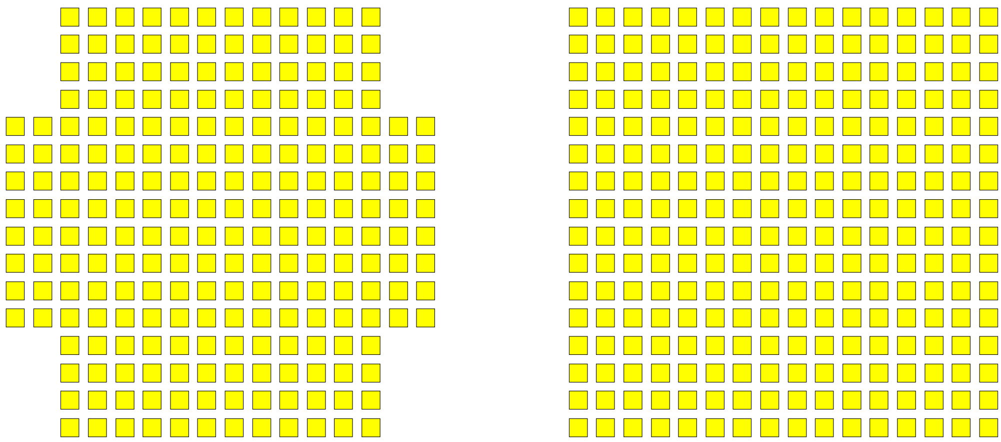

Figure 5.2: The array of PMTs used in the imaging camera. The small squares represent the photocathode area (8 mm × 8 mm) of the PMTs. The left array was used until April 1995, and the present array is shown on the right.

In order to process the signal pulses we developed a special circuit module instead of using separate circuit modules such as analogue to digital converters (ADCs) and time to digital converters (TDCs). This module is called the Čerenkov Circuit Module (CCM). One CCM has 16 input channels and consists of high gain amplifiers, current amplifiers, discriminators, ADCs, TDCs, scalers, DC current monitors and summing circuits (Figure 5.5). The ADC and TDC have 4096 counts (12 bits) maximum, with a resolution of 0.025 pC and 0.25 nsec per count respectively. The ADC gate width is about 50 nsec, which is wide compared with the time of Čerenkov pulse. However, the TDC has the advantage of eliminating signals caused by background light. The scaler and DC current monitor also have 4096 counts maximum. The scaler for each PMT counts number of pulses exceeding the discrimination

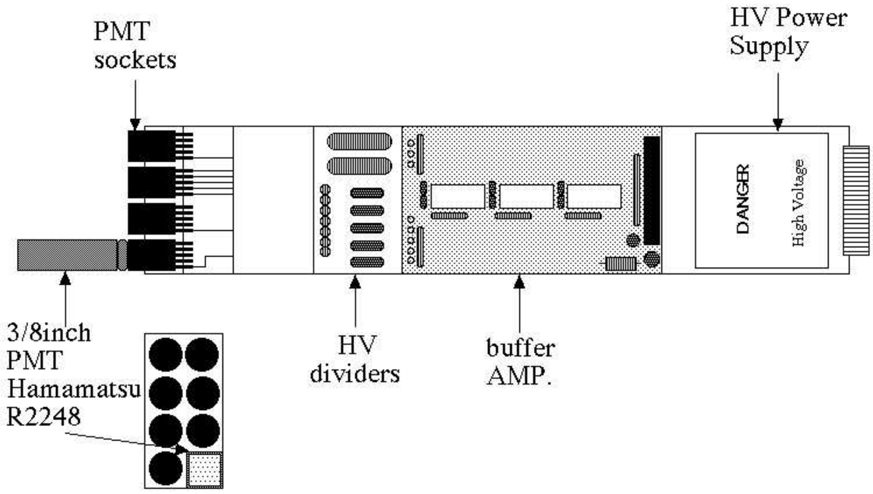

Figure 5.3: The box in which each eight PMTs are installed. Groups of eight PMTs are supplied a common preset high voltage.

level for 1 msec after an event trigger. The count of the scaler is a good indicator of the sky brightness in the field of view of the PMT, and is useful in calibrating the PMTs (Chapter 6).

In the CCM each pulse from each PMT is first amplified, and then divided into four pulses. These are sent to an ADC, a discriminator, a DC current monitor and a summing circuit. The pulse sent to a summing circuit is added with those of the other 15 channels, and then output as a "Linear Sum". Each discriminator gives an output if the input exceeds a preset level, and this output is sent to a TDC, a scaler and a summing circuit after division. The discriminator output sent to a summing circuit is also added with those of the other 15 channels, and output as a "Hit Sum".

The "Linear Sum" and "Hit Sum" outputs from each CCM are added together in linear fan-in/out modules, and are used to generate a trigger pulse for recording data. Figure 5.6 shows a block diagram of the electronics circuits for generating a master pulse for an event

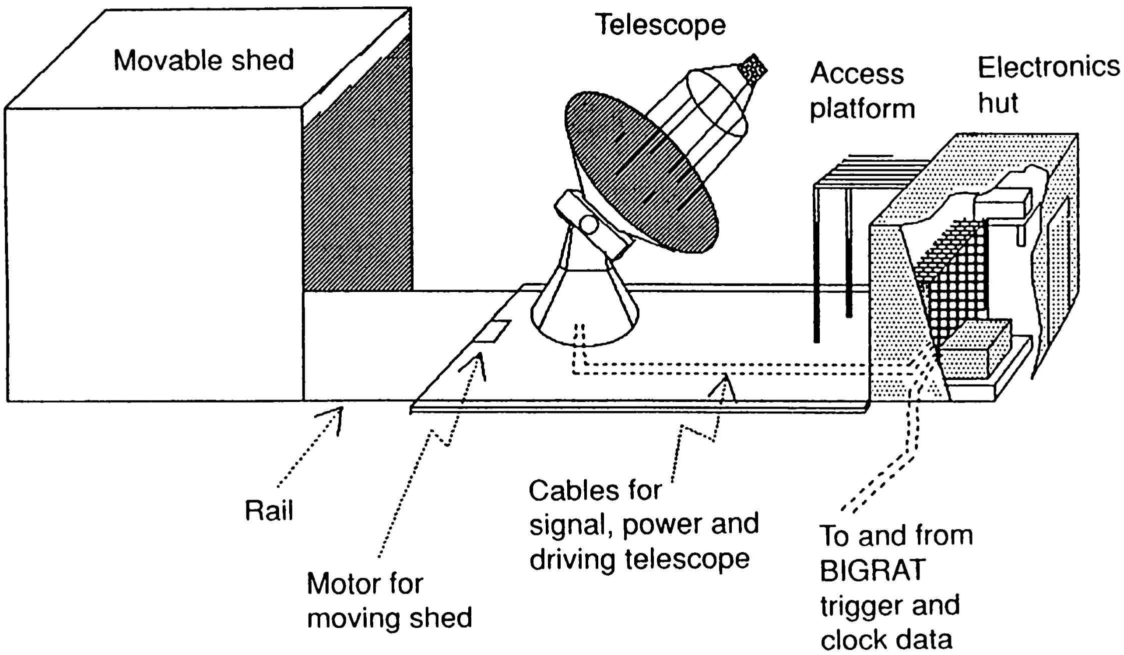

Figure 5.4: A schematic view of the experimental setup of the 3.8 m telescope [64].

trigger.

Our electronics circuit has two preset threshold levels for an event trigger as mentioned above. They have been calibrated using Monte Carlo simulations (Appendix B) and the standard value of the night sky background light. The present thresholds corresponds to 3 photoelectrons for the discriminators in the CCMs and 5 discriminated PMTs for the "Hit Sum" in average.

If a trigger pulse is generated, the data processed by the CCM are sent to a memory module in a CAMAC crate. The CAMAC system is controlled by an on-board micro processor, M68020, in which a real time operating system, OS9, of multi-tasking capability is used. The data are recorded on an 8 mm video tape using an EXABYTE and can be checked and analyzed by a workstation in Woomera.

In August 1993, a Global Positioning System (GPS), with an absolute accuracy of 200

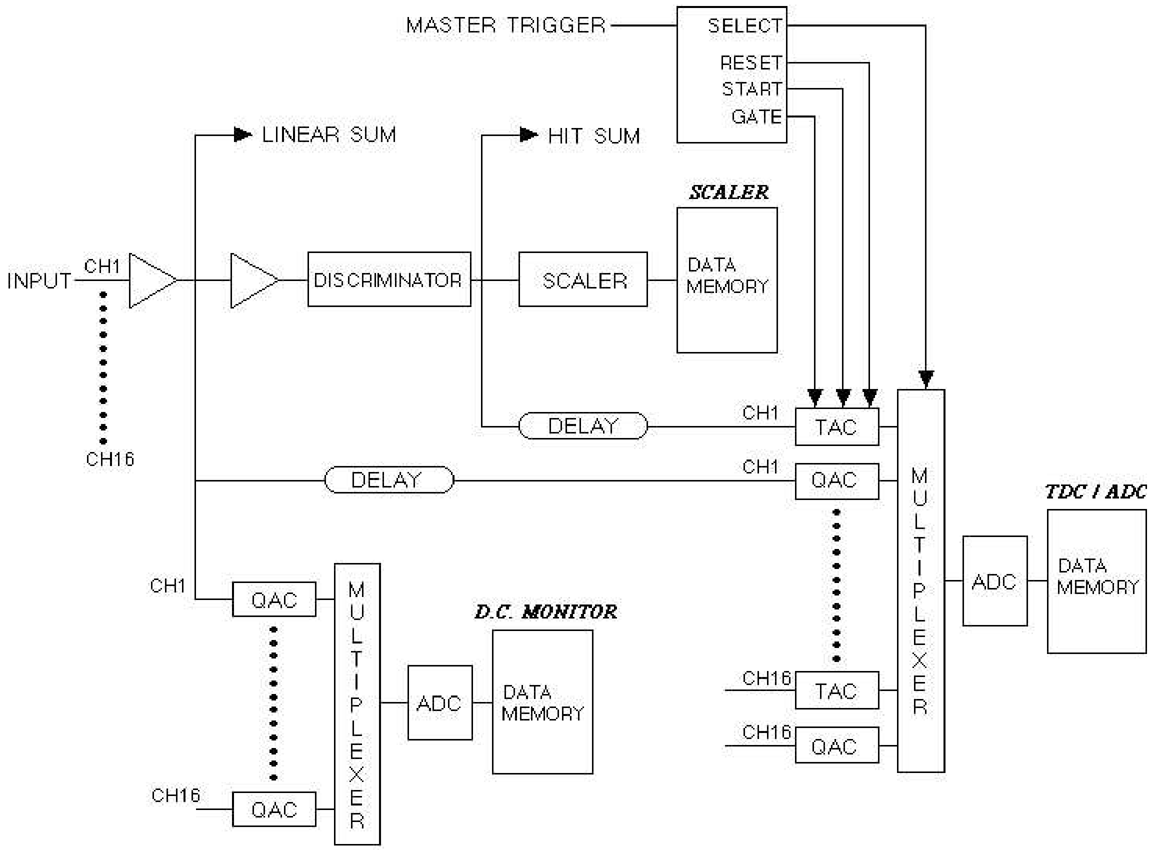

Figure 5.5: The block diagram of the CCM.

nsec, and a CAMAC module counting GPS pulses were installed. The CAMAC module measures the time differences between the GPS pulse and the pulse from our crystal clock, which has a drifting rate of $\sim 10^{-7}$, every second, and the differences are recorded with the data in every triggered event. It is possible to get accurate arrival times of events correcting them by the time differences.

Data recorded after an event trigger consist of a run number, an event number, clock data including outputs from the GPS module, outputs from the CCMs (TDC counts, ADC counts, counts of the scalers and DC currents) and several kinds of flags. In the stereoscopic observation with BIGRAT, trigger signals are sent to each other via underground cables. The trigger signals from BIGRAT are recorded as flags into data.

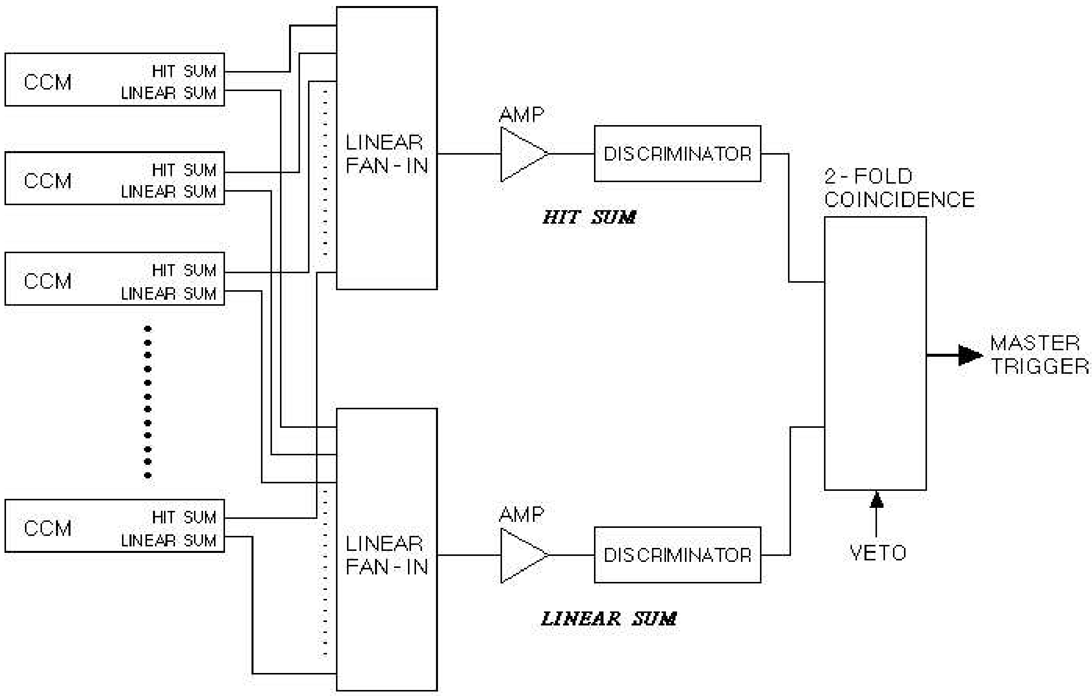

Figure 5.6: The block diagram for event trigger generation.

Chapter 6

Calibration of Tracking Accuracy of the 3.8 m Telescope

6.1 Motivation

As mentioned in Chapter 4, orientation of gamma-ray images is very sensitive to the position of the source in the field of view. Therefore, it is important to calibrate tracking accuracy of the telescope for source identifications with an angular resolution of $\leq 0^\circ.1$. The gamma-ray source candidates reviewed in Chapter 2 are not bright at optical wavelengths, and we cannot directly find the position of any source in counting rates of the PMTs. However, counting rates of the PMTs increase owing to bright stars in the field of view. Since the 3.8 m telescope is mounted on an alt-azimuth mount and the imaging camera is fixed to the reflector, the field of view rotates when the telescope is tracking a point of the sky. Therefore it is possible to calibrate the tracked point using the rotating starlight signals. A method to calibrate a tracked point in the field of view using starlight is proposed in this chapter, and its accuracy is estimated by simulation.

There are various errors which cause a tracked point differing from the center of the camera; the setting error of the camera position with respect to the reflector, the error in a direction of the telescope from a calculated direction and the error in the tracking program to control the telescope itself. Precision of our tracking program has been checked when the telescope was first installed, and the accuracy was as good as about 0°.01, which is the same as the resolution of our encoders. If the error in the tracking program and the error in the azimuthal direction of the telescope are small enough to be ignored, the tracked point is fixed in the field of view of the camera. In this case, the tracked point in the camera can be determined precisely using starlight signals rotating around the tracked point. The very fine pixel of our imaging camera (0°.18 spacing) allows an accurate determination of a tracked point.

6.2 Method of the Calibration

As mentioned in Chapter 5, counts of the scaler for each PMT give a good indication of the sky brightness in the field of view of the PMT. When bright stars are in the field of view of the camera, the scaler counts of the PMT which views one of the stars increase as shown in Figure 6.1. Such increase of scaler counts moves from one PMT to the other as the star position rotates as a function of time. The rotation center should be at the center of the field of view of the camera, if tracking of the telescope is correctly done. Inversely, possible errors of the telescope tracking can be monitored by the change of scaler counts of the PMTs.

The position of the nominal tracked point in the field of view of the imaging camera is estimated in the following procedure.

1. To extract the starlight signals from scaler counts, background levels for the scaler counts are first estimated for each PMT. Figure 6.2 shows a time profile of the scaler counts of a PMT. The scalar counts due to the background light (airglow, zodiacal light and artificial and natural light scattered by aerosols), except for the counts around the peak coincident with the passage of a star, are fitted to a quadratic function. Every scaler count is compared with this time-dependent background and counts obviously exceeding from the background are extracted together with the corresponding time.

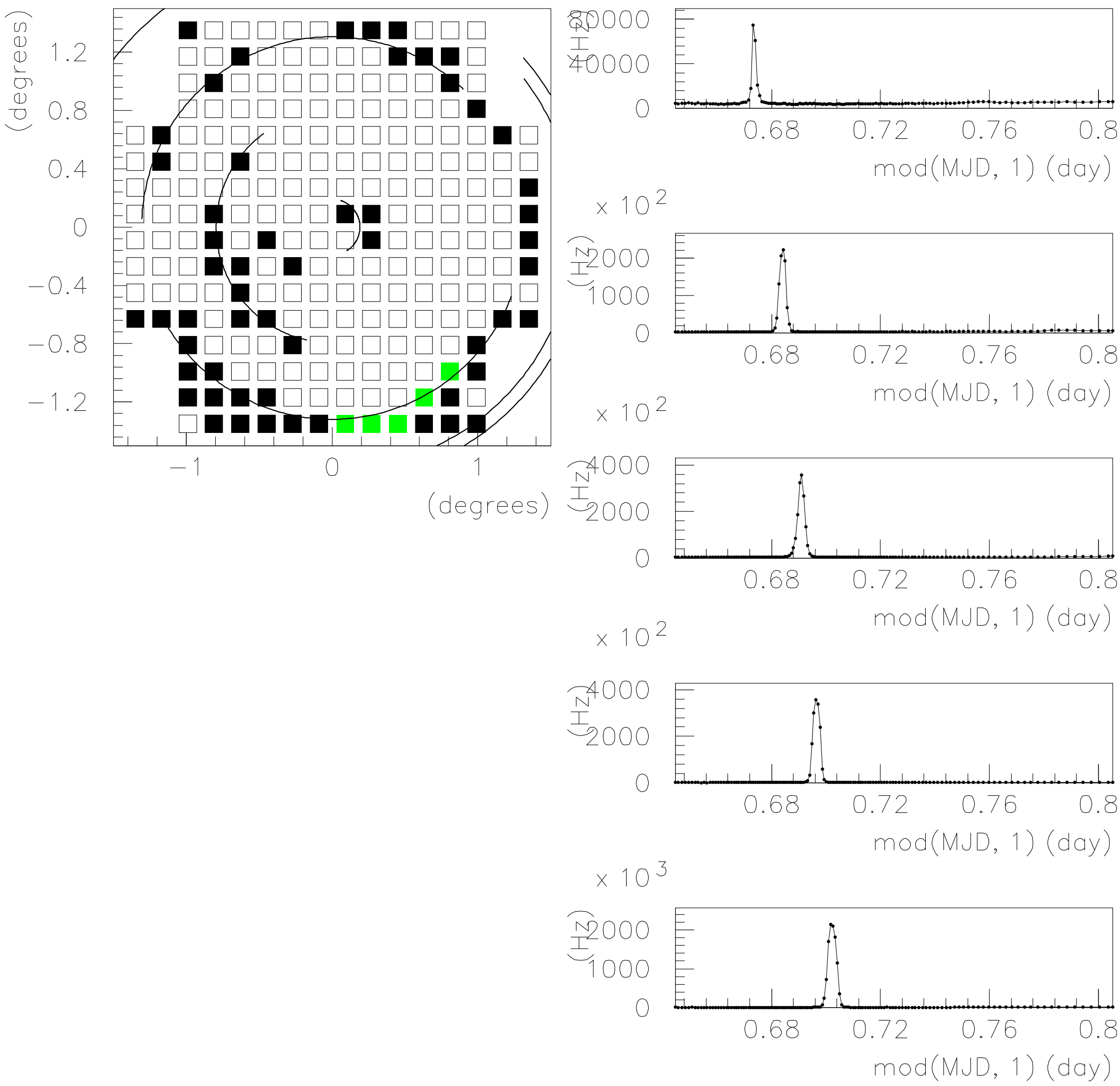

Figure 6.1: An example of the increasing scaler counts due to the passage of bright stars. The arcs in the left figure represent the expected paths of the stars in the field of view during an observation of PSR $1706-44$, and black and gray squares are the PMTs which showed an increase of the scaler count. In the figures on the right it is shown that the increase of the scaler count moves between the gray PMTs as a star of the 3.33 magnitude (η Sco) moves clockwise.

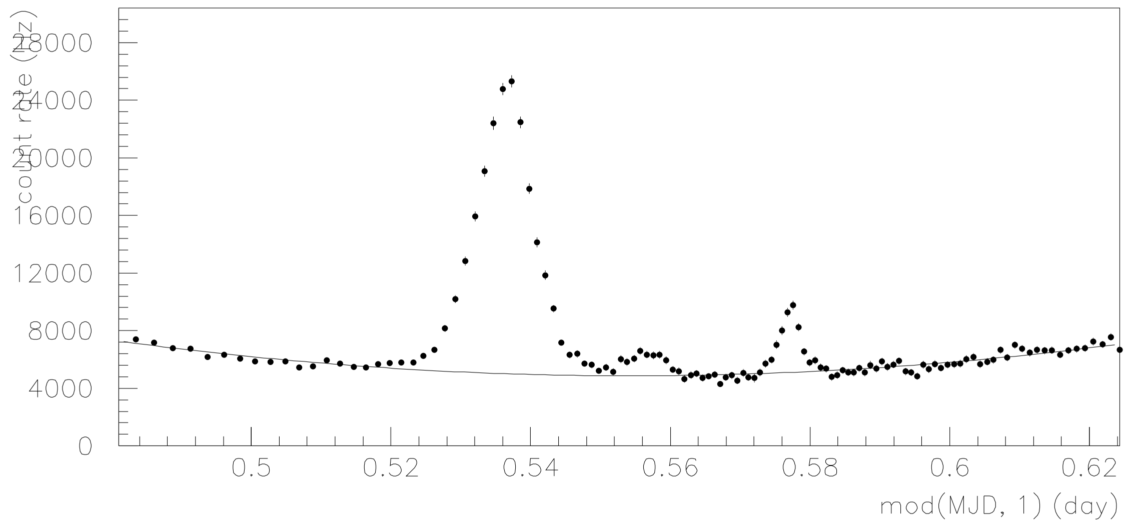

Figure 6.2: A time profile of the scaler counts during an observation of the Vela pulsar. The left peak coincides with the passage of a star of magnitude 5.99. The curve represents the background level and is determined by the fitting to a quadratic function.

2. A vector pointing from the position of a simulated starlight photon to the position of the PMT whose scaler count shows the starlight effect is defined as shown in Figure 6.3. On average, this vector is nearly equal to the vector pointing from the center of the camera to the tracked point. A few tens of starlight photons are simulated for each starlight signal to take into account the effect of the coma aberration. Since the reflector of the 3.8 m telescope is parabolic, the photon distribution of starlight on the focal plane is blurred by the coma aberration. As seen in Figure 6.4, the blur is larger in the outside of the field of view and the size is at most about $0^\circ.2$ in the field of view of the camera (the size of the photocathode is $0^\circ.12 \times 0^\circ.12$). The above vector is calculated for each simulated starlight photon and is superimposed in a map as shown in the right of Figure 6.3.

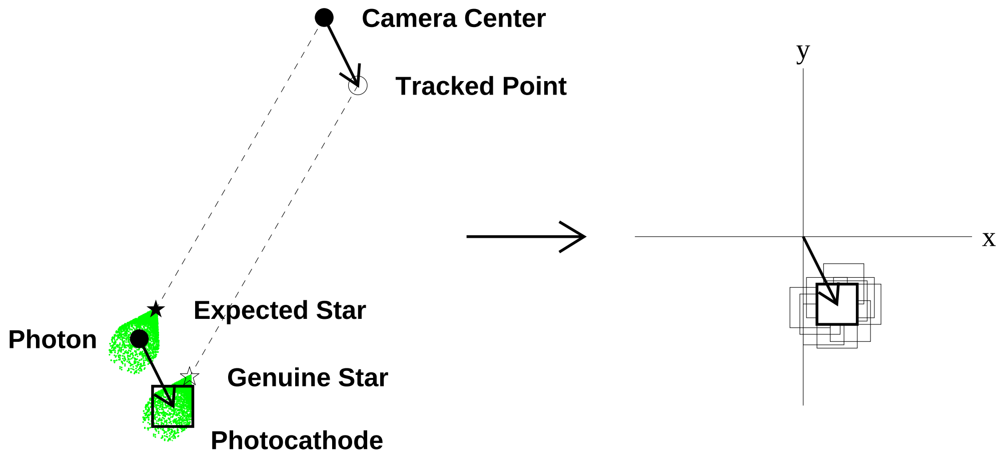

Figure 6.3: A schematic diagram of a method to calibrate a tracked point in the field of view of the imaging camera. For each scaler count including the starlight effect, vectors are taken from the expected positions of photons to the PMT. Then, the vectors are superimposed on a map.

3. A peak should be found at the tracked point in the superimposed map, for example as in the left of Figure 6.5. This peak is fitted to a two-dimensional Gaussian distribution, and the peak maximum position of the fitted Gaussian distribution is taken as the most probable position for the tracked point.

In the above method, at least one bright star is necessary to be in the field of view, and several stars should rotate longer in the field of view to determine a tracked point with better accuracy. The left map in Figure 6.5 was obtained from the data of which the observed object was the Vela pulsar. Figure 6.6 shows the distribution of bright stars around the Vela pulsar. At least four stars are in the field of view while the Vela pulsar is tracked by the 3.8 m telescope. If stars of the visual magnitude $\lesssim 6$ are considered to be useful in this calibration,

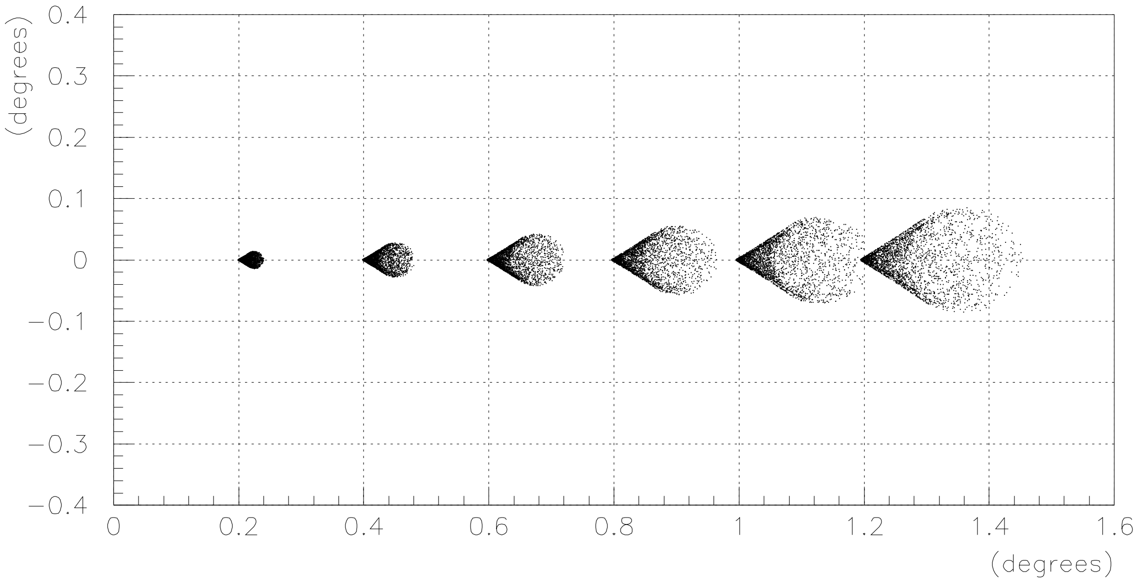

Figure 6.4: Photon images of the coma aberration for the CANGAROO 3.8 m telescope. The offset photon directions with respect to the direction of the telescope are $0°.2$, $0°.4$, $0°.6$, $0°.8$, $1°.0$ and $1°.2$, from the left.

about two of such stars are in a field of view of our camera in average. Therefore, we can expect the tracked point to be given with rather better accuracy in the case using the data of the Vela pulsar. The most probable position of the tracked point given from the left map of Figure 6.5 is at $(0°.013, -0°.018)$ with respect to the center of the camera.

6.3 Accuracy of the Calibrated Tracked Point

Assuming that the spectrum of starlight is of the blackbody radiation, $B(\lambda, T)$, photon flux of starlight at the ground is calculated by the following equation,

$$\frac{dN_s}{dSdt} = CL_0 10^{-0.4m_v} \int_{\lambda_{min}}^{\lambda_{max}} \frac{B(\lambda, T_s)}{hc/\lambda} \epsilon_t(\lambda) d\lambda, \tag{6.1}$$

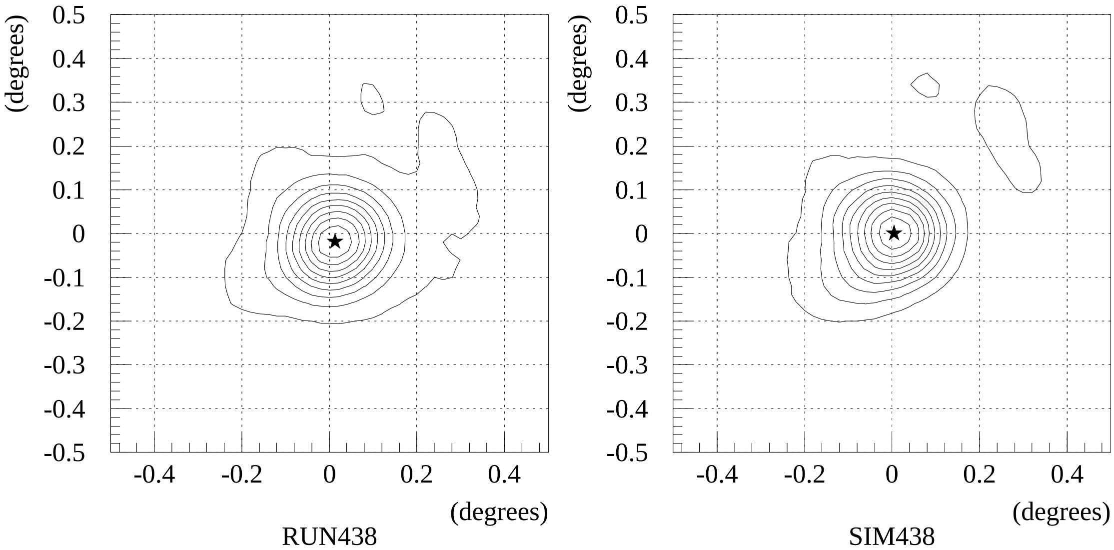

Figure 6.5: Maps indicating the position of each tracked point in the field of view of the camera (the origin is the center of the camera). The left map was produced by the superposition of vectors defined in Figure 6.3 using observed data (the target is the Vela pulsar). The star represents the most probable position of the tracked point determined by fitting the distribution to a two-dimensional Gaussian distribution. The right map was obtained by the same method but using simulated scaler data instead of the observed data. The scaler data were simulated using the same star paths in the field of view as of the left map. Thus, the right map has a similar structure to the left map.

where C is a normalization constant, m_v is the visual magnitude of the star, $L_0 = 3.64 \times 10^{-9}$ erg sec^{-1}cm^{-2}Å^{-1} is the flux of a star of visual magnitude $m_v = 0.0$ [85], T_s is the surface temperature of the star and $\epsilon_t(\lambda)$ is a transmissivity of the atmosphere for the photon of the wavelength λ. Photoelectrons are generated at a photocathode of a PMT by the above starlight in the following rate,

$$\frac{dN_{p.e.}}{dt} = \frac{dN_s}{dSdt} S_r \epsilon_r \epsilon_c \epsilon_q, \tag{6.2}$$

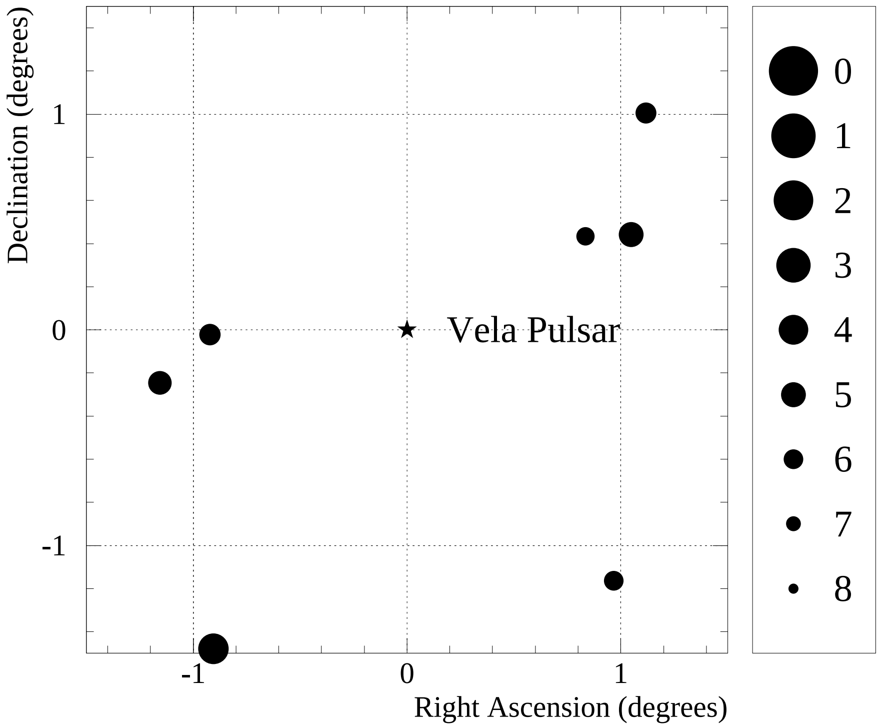

Figure 6.6: Bright stars around the Vela pulsar. The size of filled circles represents the star's visual magnitude as shown in the right of the figure. The positive y direction is the north.

where S_r is the area of the reflector, ϵ_r is the reflectivity of the reflector, ϵ_q is the quantum efficiency of the PMTs and ϵ_c is the collection factor of a PMT for reflected photons, which is calculated for each PMT and each star in the field of view taking the effect of aberration into account. In this equation, the quantum efficiency of the PMTs is approximated to be a constant of 0.2 between $\lambda_{\mathrm{min}} = 350$ nm and $\lambda_{\mathrm{max}} = 550$ nm. The observed data show a positive correlation between the above rates generating photoelectrons and the scaler counts. A correlation function has been determined using an observed data including signals of some bright stars. This function is used to convert a photoelectron rate to a scaler count.

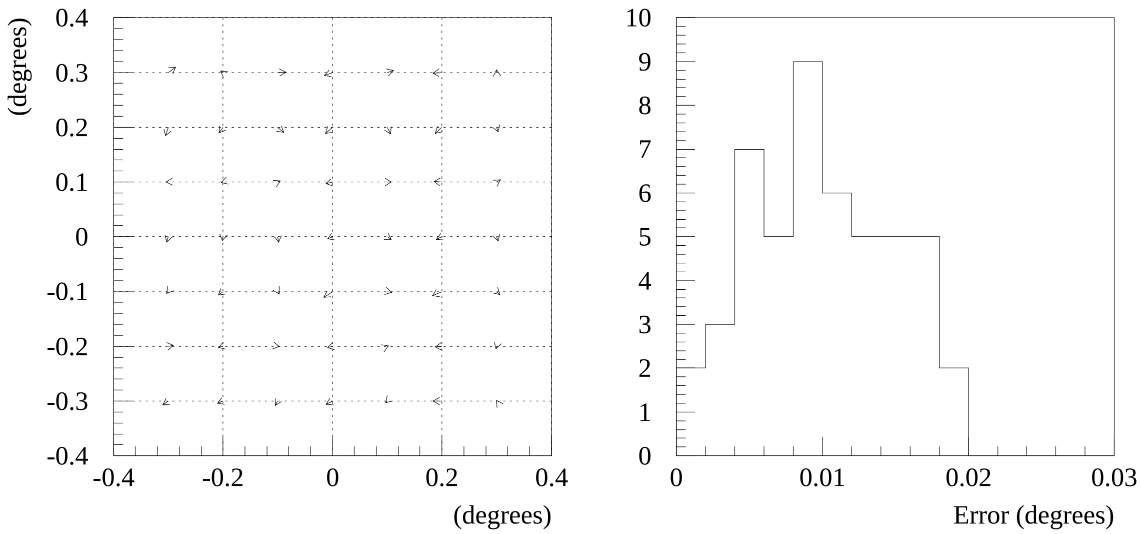

Figure 6.7: Errors of tracked points obtained by the simulation. Arrows of the left figure represent differences between input and output of the tracked points. The differences are compiled into a histogram in the right figure and the circular probable error is about $0^{\circ}.01$.

The right map of Figure 6.5 shows a resultant distribution indicating the tracked point given from the simulation. The simulation has been done using the same paths of stars as used in making the left map of Figure 6.5 and the tracked point has been input so as to agree with the center of the camera (the origin of the figure). It is seen that the simulation accurately reproduces the peak of the observed data. To estimate the accuracy of the calibration method, the simulated data have been fed into the calibration program, and differences between the input positions and the output positions of the tracked points are used as errors. The evaluation of the accuracy has been carried out in the field of view of $0^{\circ}.6 \times 0^{\circ}.6$ centered on the camera center as shown in Figure 6.7. The errors are shown by arrows in the left of Figure 6.7 and the right of Figure 6.7 is the histogram of the errors.

The circular probable error of this distribution is about $0^\circ.01$. This accuracy rather depends on the distribution and magnitude of stars in the field of view. Stars in the field of view around the Vela pulsar are used in the simulation of Figure 6.7, and the resultant accuracy of $0^\circ.01$ is rather better than the accuracy given by other fields of view because relatively many stars are in the field of view of the Vela pulsar. If paths of stars in the field of view are long enough, the accuracy is at most $0^\circ.02$, which is as good as the telescope's step size of $0^\circ.01$. The most probable position calibrated using the observed data, $(0^\circ.013, -0^\circ.018)$, almost agrees with the center of the camera. This calibrated position of the tracked point has been used in the image analysis in this thesis.

Chapter 7

Data Analysis Methods

7.1 Image Cleaning Procedures

As mentioned in Chapter 5, 12 bits values of an ADC, a TDC, a scaler and a DC current monitor for each PMT are recorded when a trigger pulse was generated. At the first step in the analysis, each ADC value must be subtracted by its pedestal value. The pedestal values include the effects of night sky background light, and are defined here as zero levels without Čerenkov light. There are two methods to calculate the ADC pedestal values and they are almost same as the methods taken in the Whipple group [36, 98]. In the first, the camera is artificially triggered so as to capture ADC values with no genuine input signal. The pedestal value and the pedestal standard deviation are calculated from simple moments of the pulse height spectrum generated from these injected events. In the second, the pedestal value and the pedestal standard deviation can be calculated using Čerenkov light triggered events, since only a small number of the PMTs contain a signal. After omitting any PMT which contains a signal or is adjacent to a PMT containing a signal, the pulse height spectrum is fitted to a Gaussian distribution as shown in Figure 7.1. To judge whether a PMT contains a signal, the TDC signal is used as a sign of a discrimination of the signal. These procedures give almost same results in the pedestal value and the pedestal standard deviation.

The pedestal standard deviation represents a noise level of the ADC value due to night sky

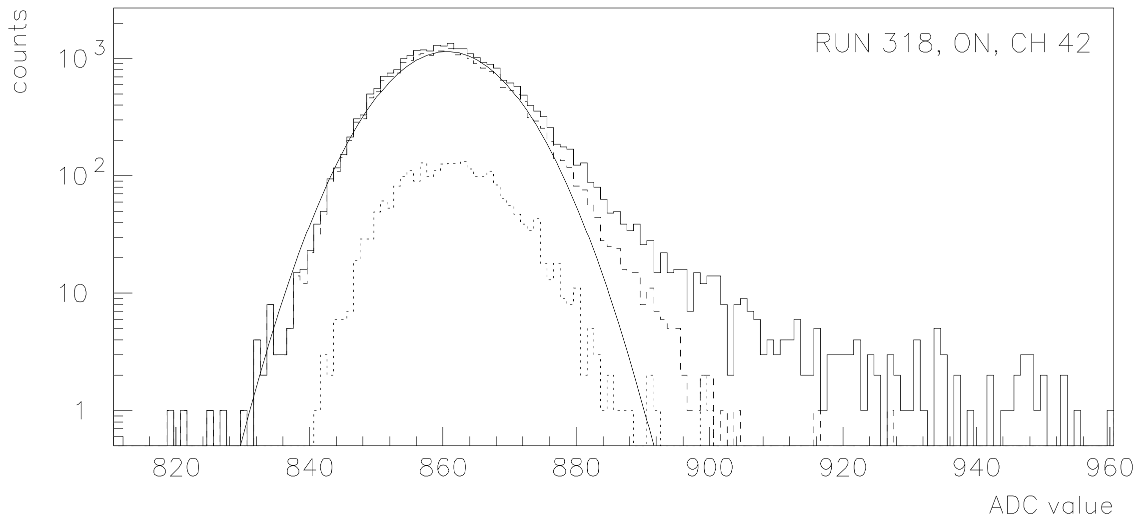

Figure 7.1: The determination of ADC pedestal values and their standard deviations. The histogram represented by the solid line is a raw pulse height spectrum. The signal-rejected histogram (dashed line) is fitted to a Gaussian (solid curve). The pulse height spectrum of artificially triggered events (dotted line) gives consistent results with the dashed histogram.

background light and electronic noises. The brightness of night sky background light is about 1×10^8 photons cm^{-2} sec^{-1} str^{-1} in the wavelength region from 350 nm to 550 nm [59], in which the PMT is sensitive in terms of the quantum efficiency, and because of this background light, 0.25 photoelectrons are, in average, generated in the photocathode of one PMT in the ~ 50 nsec gate for the ADC. This is a small value compared with the discrimination level of ~ 3 photoelectrons for TDCs, scalers and an event trigger, but this noise distorts the shape of the image especially having small ADC values. Therefore, any PMT signal lower than a certain threshold based on the noise level is rejected from the image. In the present analysis, $1\ \sigma$ is taken for this threshold.

After subtraction of the ADC pedestal values, the ADC values of a Čerenkov image are normalized by their relative gains. To determine relative PMT gains, about a few thousand images are recorded several times a night using a fast-timing ($\sim$ 20 nsec) blue LED illuminating the camera from the 3.8 m distance. Using the LED data, relative gains are calculated night by night.

The gate width of our ADC is about 50 nsec as mentioned above, and this is relatively wide compared with the time scale of a Čerenkov light wave which is less than 10 nsec. However, our TDC compensates this demerit. Since the probability in which a random background signal coincides with a Čerenkov light wave is very low, Most of signals due to night sky background can be rejected using fast timing of the TDC.

TDCs also have different pedestal values. The TDC pedestal value is calculated using the above LED data, and it is defined as a mean value of the TDC distribution. TDC values in a raw Čerenkov image are subtracted by their pedestal values and any signal whose TDC value is outside of a time window is rejected. Figure 7.2 shows the distribution of TDC values subtracted by their pedestal values. At present analyses, only PMTs having TDC values between the dashed lines in Figure 7.2 are used in calculation of image parameters. The width of this time window corresponds to about 70 nsec.

To reject the false events, which is caused by accidental coincidences due to night sky background light or electronic noises, the images are discriminated depending on the total ADC counts and number of PMTs possible to use in the parameterization. This discrimination is based on the facts that an image having a lower total ADC counts and a small number of PMTs includes more noises, and thus is difficult to be reconstructed. The discrimination levels used now are ≥ 200 for the total ADC counts, which corresponds to about 20 photoelectrons, and ≥ 5 for the number of PMTs.

Sometimes we have found electronic noises due to the motors controlling the telescope especially in our old data. The images due to this noises have a typical pattern in which PMT signals cluster only at a box of eight PMTs. Eight PMTs of one box share a common

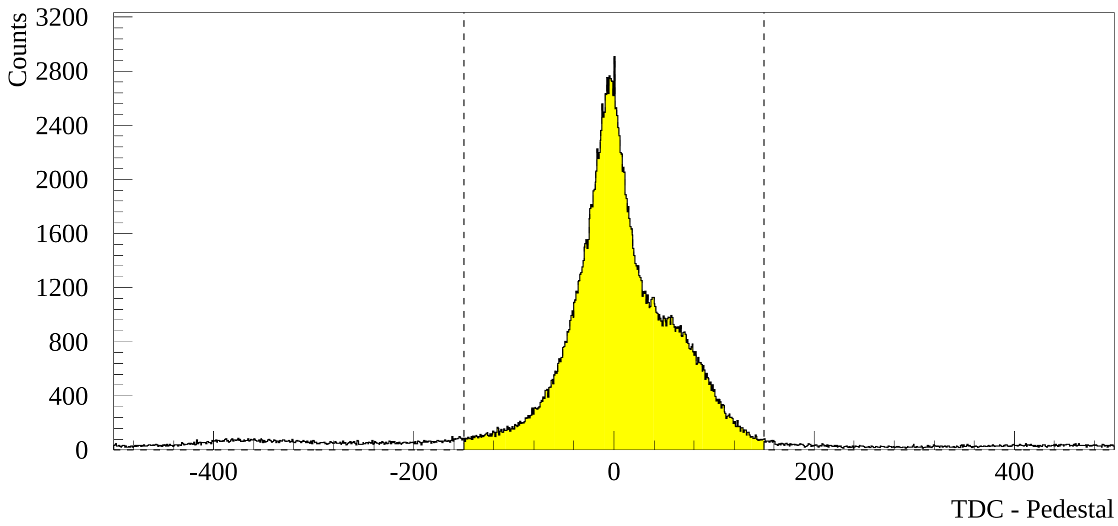

Figure 7.2: The distribution of TDC values subtracted by their pedestal values. Only PMTs having TDC values between the dashed lines (the shaded area) are used in the image analysis.

ground which is possibly different from other boxes, and thus the noise was probably picked up simultaneously for eight PMTs. However, This noises can be rejected using the ratio of the number of signal PMTs in a box to the total number of signal PMTs in the image. This ratio should be ~ 1 for the noise images, whereas shower images do not have such a tendency. Image centroid distributions in the field of view before this noise rejection and after the rejection are shown in Figure 7.3. It appears that the noises have been successfully rejected. The fraction of the gamma-ray image having this noise pattern has been checked by Monte Carlo simulations and only ~ 2 % of the simulated gamma-ray images are lost by this noise selection. This noise has been recently reduced by improvement of the system.

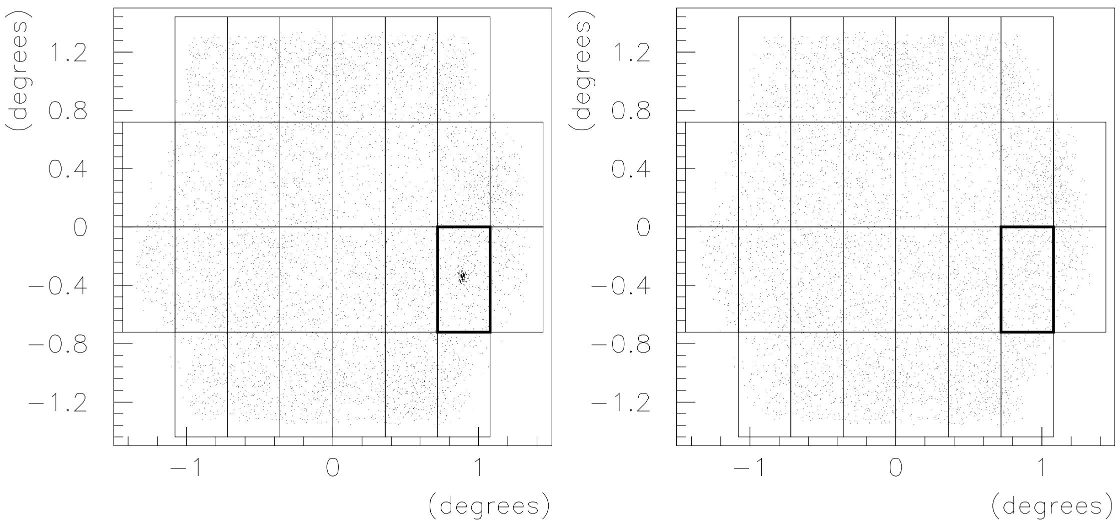

Figure 7.3: Image centroid distributions before the noise rejection (left) and after the rejection (right). The noises observed in a box of eight PMTs represented by the thick lines have been rejected in the right distribution.

7.2 Selection of Gamma-Ray-Like Images

7.2.1 Selection Criteria

An image selected in the above procedures is fitted to an ellipse and the parameters defined in Chapter 4 are calculated for each event. On the basis of the parameter distributions given by Monte Carlo simulations of gamma-ray and proton showers, which are shown in Figure 4.6, "canonical" selection criteria for the enhancement of a gamma-ray signal from a point source are defined as follows:

For image shape:

$$\begin{aligned} 0^\circ.01 &\leq \text{Width} \leq 0^\circ.08 \\ 0^\circ.1 &\leq \text{Length} \leq 0^\circ.4 \\ 0.4 &\leq \text{Conc} \leq 0.9 \end{aligned} \tag{7.1}$$

For image location:

$$0^\circ.6 \leq \text{Distance} \leq 1^\circ.3 \tag{7.2}$$

For image orientation:

$$\text{Alpha} \leq 10^\circ \tag{7.3}$$

Before the selection using the above criteria, the images near the edge of the camera, whose centroids are more than 1° distant from the center of the camera, are eliminated since a part of such an image is probably outside of the camera and the image is distorted. Distance and Alpha distributions of observed background images before and after this edge selection are shown in Figure 7.4, where Distance and Alpha are calculated assuming that the nominal source is at the center of the camera. The Alpha distribution of background images should be flat as described in Chapter 4. However, the Alpha distribution before the edge selection is not flat. This effect is reduced by the edge selection and a flat Alpha distribution is obtained as shown in the figure. $50 \sim 60$ % of background images are rejected by this edge selection, while ~ 60 % of the simulated gamma-ray images remain after this selection.

Of the above canonical criteria, the selection for Distance has two meanings. Distance of the gamma-ray image has a positive correlation with the impact parameter between the shower axis and the telescope. Thus, the upper limit for Distance roughly represents the maximum radius of the Čerenkov lateral distribution of gamma-ray showers. On the other hand, gamma-ray showers having small impact parameters make nearly circular images near the source direction in the field of view. The lower limit for Distance is set to reject such images of which Alphas are less accurately determined. The background images passing

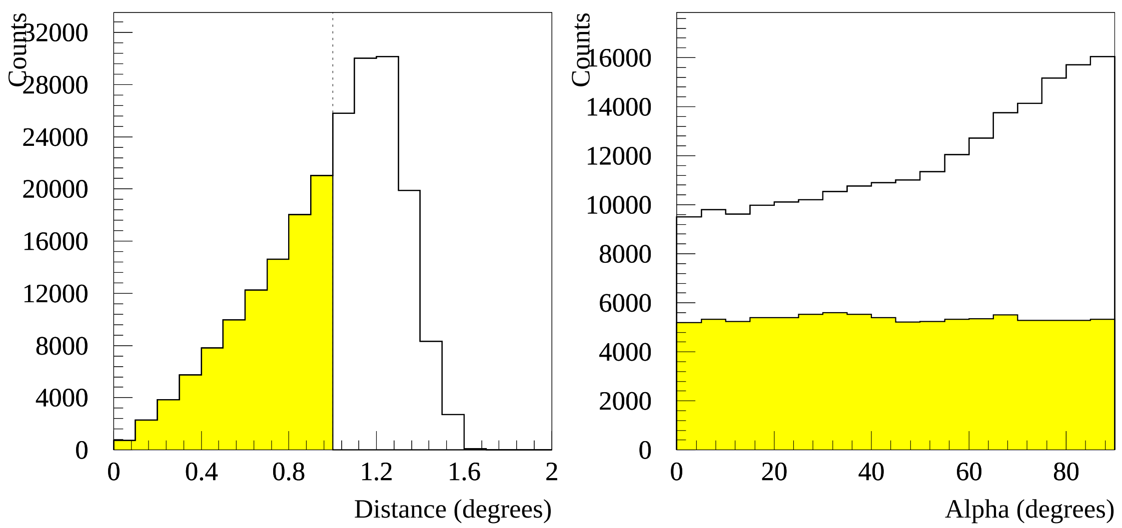

Figure 7.4: Distance and Alpha distributions of observed background images before and after the edge selection. The shaded histograms represent the distributions after the selection. The edge effect seen in the Alpha distribution is reduced by the selection and the flat Alpha distribution is obtained.

through the edge selection are further reduced to about 20 %, 60 %, 10 % and 2 % by the shape selections (Width, Length and Conc), the location selection (Distance), the orientation selection (Alpha) and the all selections, respectively. On the other hand, about 80 %, 80 %, 90 % and 70 % of the gamma-ray images remain after the shape, location, orientation and all selections, respectively.

The numbers of selected events of on-source and off-source data are compared together, and a gamma-ray signal should appear as a positive excess of the on-source event rate against the off-source.

7.2.2 Definition of Significance

As described in Chapter 4, Čerenkov telescopes detect the numerous backgrounds due to cosmic-ray nuclei. They cannot be rejected completely even after the above selections. Therefore, any detected gamma-ray signal is used to be compared with the fluctuation of the background level. If $N_{\rm on}$ and $N_{\rm off}$ events were recorded from a suspected source direction and background regions using the on/off tracking, the observed signal, the probable number of gamma rays contributed by the source, is

$$N_s = N_{\rm on} - \langle N_b \rangle = N_{\rm on} - \alpha N_{\rm off}, \tag{7.4}$$

where $\langle N_b \rangle$ is the estimate of the background included in $N_{\rm on}$ and α is the ratio of the on-source and off-source exposures. Since on-source and off-source counts are results of two independent measurements, one can estimate the standard deviation of the signal N_s:

$$\langle \sigma_s \rangle = (\langle \sigma_{\rm on} \rangle^2 + \alpha^2 \langle \sigma_{\rm off} \rangle^2)^{1/2} = (N_{\rm on} + \alpha^2 N_{\rm off})^{1/2}, \tag{7.5}$$

where $\langle \sigma_{\rm on} \rangle$ and $\langle \sigma_{\rm off} \rangle$ are the expected standard deviations of the on-source and off-source counts, respectively. In the above equation, the error of α has been ignored. Defining the significance S as a ratio of the excess count above background to its standard deviation, we have

$$S = \frac{N_s}{\langle \sigma_s \rangle} = \frac{N_{\rm on} - \alpha N_{\rm off}}{(N_{\rm on} + \alpha^2 N_{\rm off})^{1/2}}. \tag{7.6}$$

Significances calculated by the above equation have been investigated using Monte Carlo simulations by Li and Ma under the hypothesis that only background events have been detected, and are consistent with the Gaussian probabilities for $\alpha = 1$, but are systematically underestimated for $\alpha < 1$ and overestimated for $\alpha > 1$ [68]. Since our observations have usually been done in the on/off tracking and $\alpha = 1$, (7.6) will be used in the following analyses.

7.2.3 Asymmetry

In Chapter 4, the image parameters were defined assuming gamma-ray images to be elliptical. However, gamma-ray images are asymmetrical along their major axes since they elongate in the opposite side against the source position in the field of view, where the impact parameter between the shower axis and the telescope is smaller. The simulated gamma-ray image in Figure4.4 indeed shows this tendency. Using this tendency of gamma-ray images, we can determine directions of primary gamma-rays with higher accuracy, and thus gamma-ray sources can be detect with higher sensitivity. On the basis of this tendency, a new image parameter "Asymmetry" was recently proposed by Punch [92] (its basic idea has originally been shown by MacKeown et al. [71]) and he showed it was useful for further enhancement of gamma-ray signals using the data including gamma-ray signals from the Crab nebula. Asymmetry gives an asymmetry of the photon density on the image along the major axis. The location of the peak intensity of Čevenkov light is rather shifted to the source from the image centroid for the gamma-ray image. To detect this tendency, the "Asymmetry Vector" $\vec{A}$ is defined so as to point towards the source position from the centroid and have a length equal to the cubic root of the third moment of the image along the major axis, since the asymmetry of the photon density is reflected in its odd moments. See Appendix A in detail. The vector is schematically shown in Figure 7.5. If $\vec{D}$ is an distance vector pointing from the image centroid to the assumed source, Asymmetry normalized by Length is given as the following formula;

$$\text{Asymmetry} = \frac{\vec{A} \cdot \vec{D}}{\text{Distance Length } \cos(\text{Alpha})}. \tag{7.7}$$

Asymmetry distributions of Monte Carlo simulated Čerenkov images are shown in Figure 7.6. The distribution of gamma-ray images is well one-sided and concentrated around Asymmetry = 1, while the distribution of background (proton) images is almost symmetrical since the directions of the simulated primary protons are isotropic.

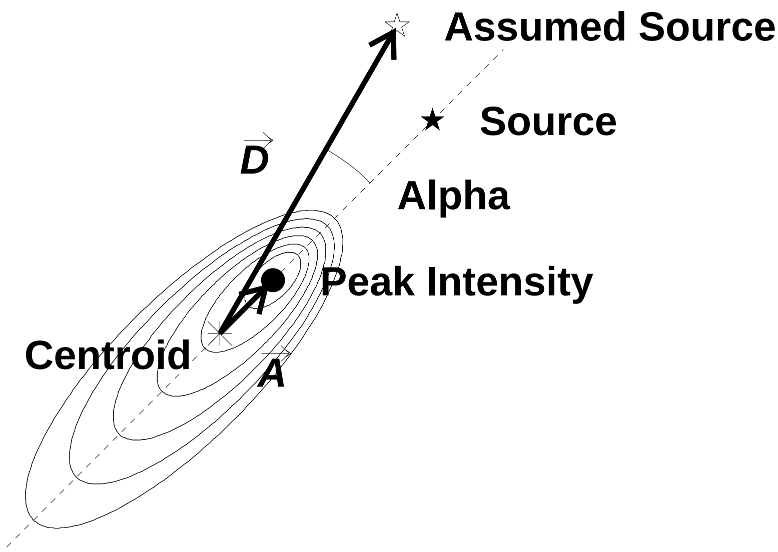

Figure 7.5: A schematic diagram of a typical gamma-ray image to define Asymmetry Vector $\vec{A}$. The Asymmetry Vector is taken along the major axis of the image and points to the source. Its length is the cubic root of the third moment of the image along the major axis.

7.3 Reconstruction of a Gamma-Ray Source Direction

The gamma-ray source has been assumed to be at the center of the field of view in the above. However, the gamma-ray source should lie along the major axis of the gamma-ray image as mentioned in Chapter 4, and thus the source position in the field of view can be reconstructed even if it is not at the center of the field of view. Akerlof et al. first suggested a conventional method to reconstruct a source position in the field of view using their Crab data base and they could determine the source position with errors of $0^\circ.13 \sim 0^\circ.21$ *for an averaged gamma-ray image* [2]. This method is useful to search a field of view of about

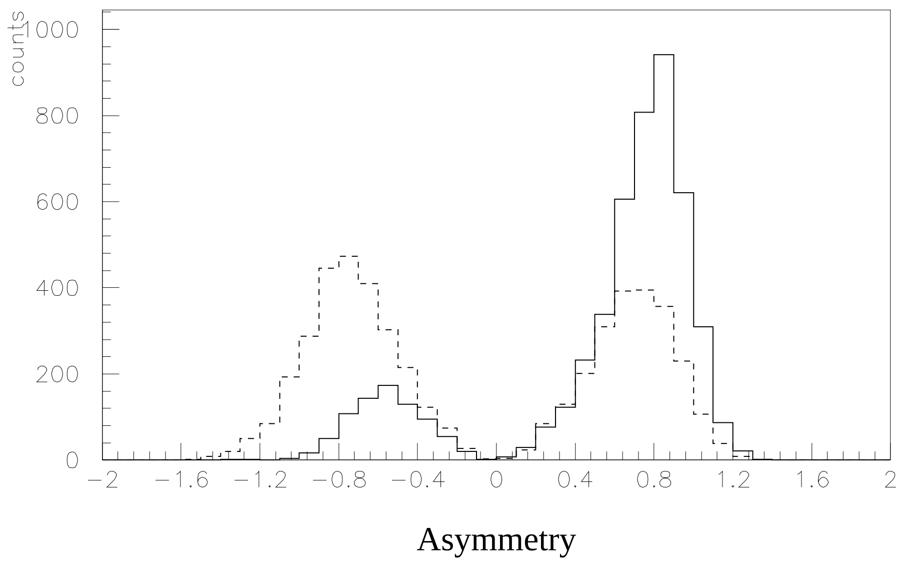

Figure 7.6: Asymmetry distributions of Monte Carlo simulated images. The distribution of gamma-ray images is represented by a solid line, while the dashed line is of proton images.

1° radius for the source of which the position is unknown. Moreover, the "good" angular resolution of this method is an advantage of the Čerenkov imaging technique compared with resolutions of the other gamma-ray experiments (about 1° in both of satellite experiments and air shower arrays). In this section, methods to reconstruct a source position in the field of view are explained and an advanced method is proposed.

7.3.1 Conventional Method

Gamma-ray signals can be estimated as a function of the position in the field of view as the following procedure. First, a Cartesian grid is overlapped on the field of view as shown in Figure 7.7. Each mesh point is assumed to be a possible gamma-ray source. The image

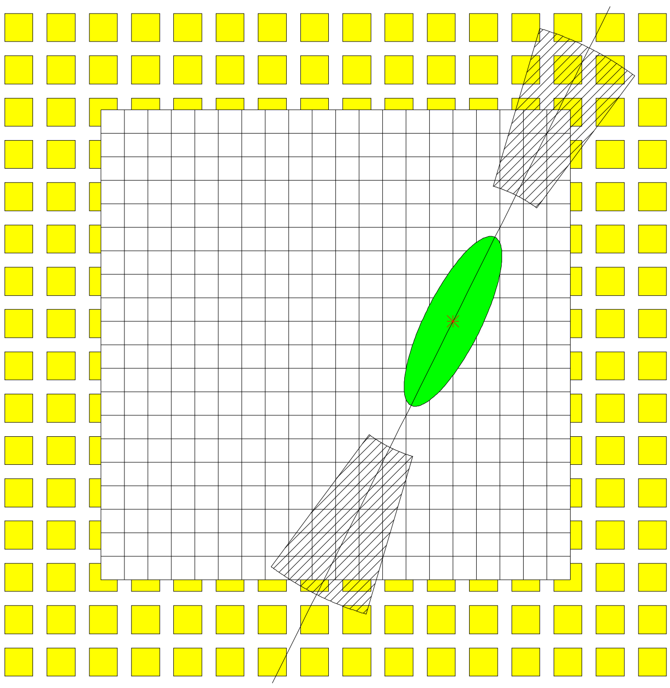

Figure 7.7: A schematic diagram of a method to search a gamma-ray source in the field of view. The image parameters are calculated assuming each mesh point to be a possible gamma-ray source. The hatched areas represent source candidate regions for the image given by the selection criteria for Distance and Alpha.

parameters are calculated for each event about every mesh point, then they are checked for compatibility with the gamma-ray selection criteria defined above. By carring out this process for every event in the data, a two-dimensional histogram can be constructed of events versus right ascension and declination. A map of the excess counts of on-source events above the background is obtained subtracting the corresponding off-source histogram from the on-source histogram. If a gamma-ray source is in the field of view of the on-source, a significant excess should appear at its location.

In the above method, only values of Distance and Alpha depend on the assumed source location. From the selection criteria for Distance and Alpha, mesh points in the hatched areas of Figure 7.7 are the probable candidates for the source location of the event. Thus, we take the hatched areas to be the source location with an equal weight. The "fan" shape of this weighting function is taken just for simplicity.

7.3.2 Source Probability Density Function

A weighting function reflecting the source position more precisely should be determined using Monte Carlo simulated gamma-ray images. This function is defined here as the "Source Probability Density Function (SPDF)". The SPDF is given by the following procedure. Monte Carlo simulated gamma-ray images are distributed as the left of Figure 7.8 if the source is at the center of the field of view. After calculating their centroids and major axes, all of these images are transformed together with the source positions so as to have the same centroid and the same axis, then a distribution of the transformed source positions with respect to the unified image is given. If the distribution of the source positions is approximated to a two-dimensional Gaussian distribution, it represents a probability density function of the source location with respect to the gamma-ray image. In the case that the centroid and the major axis correspond to the origin and the x axis respectively, the SPDF has the following formula;

$$\begin{aligned} P(x,y) &= \frac{1}{4\pi\sigma_x\sigma_y}\exp\left(-\frac{1}{2}\left\{\left(\frac{x-d}{\sigma_x}\right)^2+\left(\frac{y}{\sigma_y}\right)^2\right\}\right) \\ &\quad +\frac{1}{4\pi\sigma_x\sigma_y}\exp\left(-\frac{1}{2}\left\{\left(\frac{x+d}{\sigma_x}\right)^2+\left(\frac{y}{\sigma_y}\right)^2\right\}\right). \end{aligned} \tag{7.8}$$

σ_x, σ_y and d are given as simple moments of the above distribution, and they are determined as follows for the 3.8 m telescope by simulation;

$$d = 0^\circ.940,\quad \sigma_x = 0^\circ.252,\quad \sigma_y = 0^\circ.088. \tag{7.9}$$

In the definition of (7.8), two two-dimensional Gaussian distributions are superimposed symmetrically with respect to the image centroid since the asymmetry of the image is not taken

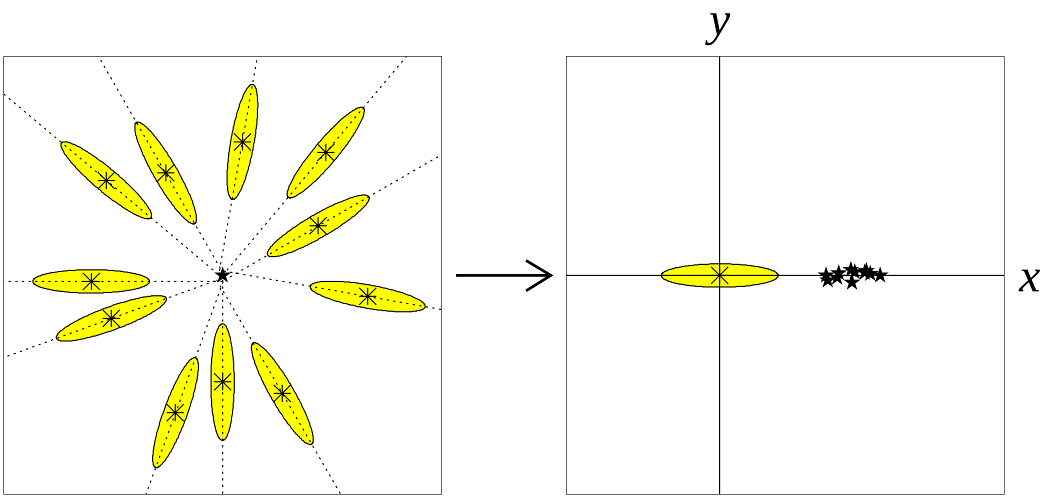

Figure 7.8: A schematic diagram of a method to obtain the SPDF. Monte Carlo simulated gamma-ray images are distributed as the left figure, where the source is located at the center of the field of view ($\star$). These images are transformed to the same image as the right, and the SPDF is given by the distribution of transformed source locations.

into account here. (7.8) is defined as the "symmetrical SPDF".

A two-dimensional distribution of event density is obtained by superimposing SPDFs of gamma-ray like images given after the image shape selections, as shown in Figure 7.9, instead of the "fan" shaped function of Figure 7.7. In the case using the conventional method, the vertical axis of the two-dimensional histogram does not have a clear meaning. However the superposition of SPDFs gives the vertical axis the meaning of event density since each SPDF is a probability density function and its integration is equal to 1.

In the conventional method, statistical significance of an excess count for each mesh point is calculated using (7.6) with $\alpha = 1$. A similar quantity is obtained about every mesh point

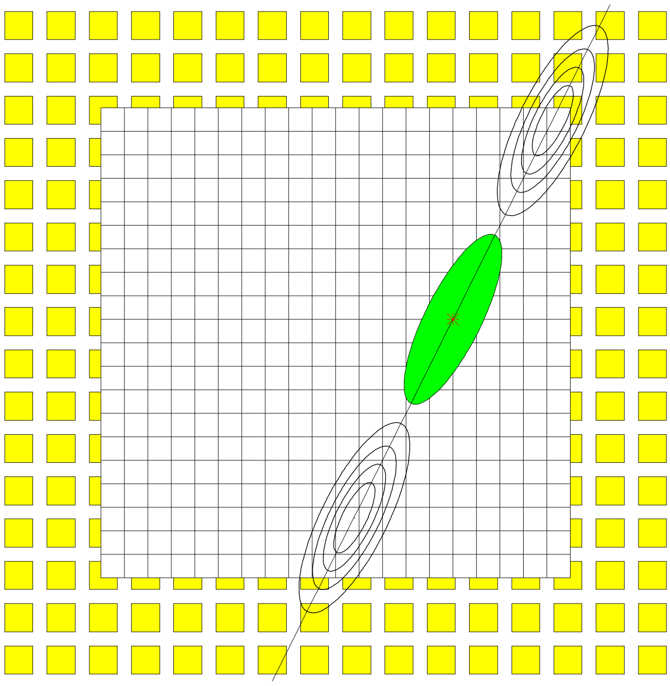

Figure 7.9: A diagram similar to Figure 7.7 using a SPDF.

summing up probabilities, or expectations, of events given by SPDFs, but the fluctuation of the quantity is not of the Poisson fluctuation. By defining S_i as the sum of probabilities given by the SPDF for the ith mesh point of the coordinates (x_i, y_i), that is,

$$S_i = \sum_j^n P(X_{ij}, Y_{ij}), \tag{7.10}$$

then the fluctuation of S_i, σ_i, is

$$\sigma_i^2 = \sum_j^n P(X_{ij}, Y_{ij})^2, \tag{7.11}$$

where (X_{ij}, Y_{ij}) is

$$X_{ij} = (x_i - \langle x \rangle_j) \cos\theta_j + (y_i - \langle y \rangle_j) \sin\theta_j, \tag{7.12}$$

$$Y_{ij} = -(x_i - \langle x \rangle_j) \sin\theta_j + (y_i - \langle y \rangle_j) \cos\theta_j. \tag{7.13}$$

$(\langle x\rangle_j, \langle y\rangle_j)$ and θ_j are the coordinates of the centroid for the jth event and the angle of the major axis from the x axis for the jth event, respectively. In this case, statistical significance of an excess signal is given by the following equation instead of (7.6);

$$S = \frac{S_{\text{on}} - S_{\text{off}}}{(\sigma_{\text{on}}^2 + \sigma_{\text{off}}^2)^{1/2}}, \tag{7.14}$$

where the amounts of exposure are assumed to be same between the on-source and off-source observations. The indicator i is omitted in (7.14).

The asymmetrical feature of the gamma-ray image mentioned in Section 7.2 can be included in this method, and increases the reliability of the estimated source position. If simulated gamma-ray images are transformed in Figure 7.8 so that their Asymmetry Vectors have the same directions as the x axis, the source distribution is fairly one-sided and its projection to the x axis is similar to the Asymmetry distribution of Figure 7.6 as seen in Figure 7.10. Here two-dimensional Gaussian distributions are obtained in the regions of $x > 0$ and $x < 0$ separately. As a result, the "asymmetrical SPDF" has the following formula;

$$\begin{aligned} P(x,y) &= \frac{f}{2\pi\sigma_{x1}\sigma_{y1}} \exp\left(-\frac{1}{2}\left\{\left(\frac{x-d_1}{\sigma_{x1}}\right)^2 + \left(\frac{y}{\sigma_{y1}}\right)^2\right\}\right) \\ &\quad + \frac{1-f}{2\pi\sigma_{x2}\sigma_{y2}} \exp\left(-\frac{1}{2}\left\{\left(\frac{x+d_2}{\sigma_{x2}}\right)^2 + \left(\frac{y}{\sigma_{y2}}\right)^2\right\}\right). \end{aligned} \tag{7.15}$$

The profile of this function is also shown in Figure 7.10. The parameters in (7.15) are determined by the simulation as follows;

$$f = 0.829, \tag{7.16}$$

$$d_1 = 0^\circ.931, \quad \sigma_{x1} = 0^\circ.248, \quad \sigma_{y1} = 0^\circ.083, \tag{7.17}$$

$$d_2 = 0^\circ.981, \quad \sigma_{x2} = 0^\circ.266, \quad \sigma_{y2} = 0^\circ.107. \tag{7.18}$$

The value of $f \sim 0.83$ means that a gamma-ray image points to the direction of its source in the field of view in the probability of ~ 83 %.

The spread of the source position derived from the above method is estimated using Monte Carlo simulation. The point spread function (PSF) for the case using the asymmetrical SPDF

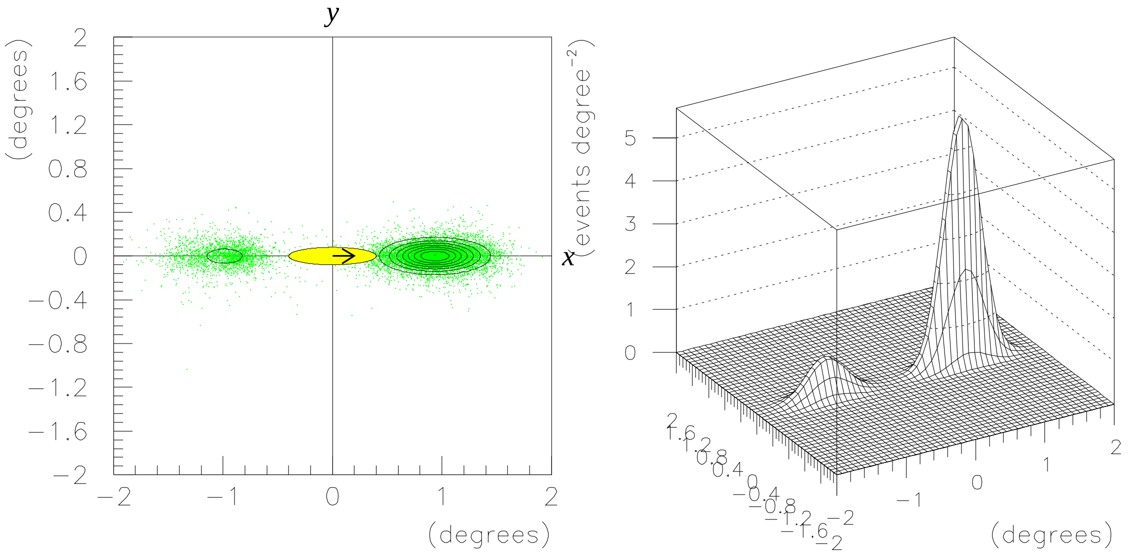

Figure 7.10: A contour plot and a histogram of the asymmetrical SPDF. The scatter plot of the left figure is the distribution of gamma-ray sources relative to the images given by a Monte Carlo simulation. The arrow in the typical gamma-ray image represents the Asymmetry Vector defined in Section 7.2.

is shown in Figure 7.11. This PSF is well approximated to a sum of two two-dimensional Gaussian distributions as

$$F(x, y; x_s, y_s) = f \exp\left(-\frac{(x - x_s)^2 + (y - y_s)^2}{2\sigma_1^2}\right) + (1 - f) \exp\left(-\frac{(x - x_s)^2 + (y - y_s)^2}{2\sigma_2^2}\right), \tag{7.19}$$

where (x_s, y_s) is the position of the gamma-ray source in the field of view and the other parameters have been obtained by fitting the distribution of Figure 7.11 to (7.19) as

$$f = 0.692, \quad \sigma_1 = 0^\circ.130, \quad \sigma_2 = 0^\circ.266. \tag{7.20}$$

This approximated function is shown in the right of Figure 7.11. If gamma rays are emitted from an extended region, the reconstructed peak profile will be broader than that of the above

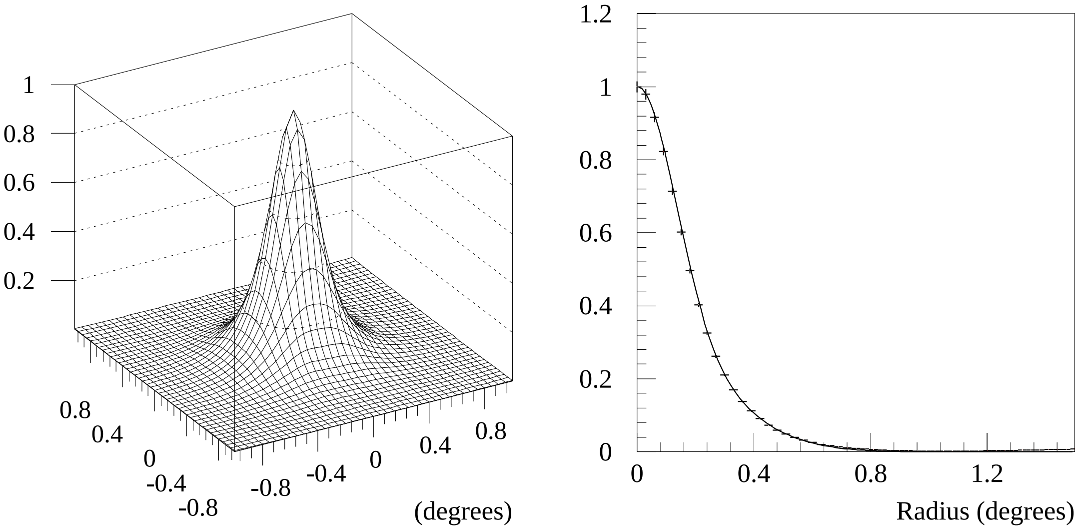

Figure 7.11: The point spread function (PSF) in the source reconstruction method using the asymmetrical SPDF. The PSF is well approximated to a sum of two two-dimensional Gaussian distribution and the line in the radial profile (right) shows the approximated function (7.19).

PSF. *Assuming that the gamma-ray intensity distribution is of a Gaussian distribution*, (7.19) can be modified for the diffuse emission as

$$F(x, y; x_s, y_s, \sigma_s) = f \exp\left(-\frac{(x-x_s)^2 + (y-y_s)^2}{2(\sigma_1^2 + \sigma_s^2)}\right) + (1-f)\exp\left(-\frac{(x-x_s)^2 + (y-y_s)^2}{2(\sigma_2^2 + \sigma_s^2)}\right), \tag{7.21}$$

The position and size of an observed gamma-ray source can be estimated by fitting the distribution of excess event density, $S_{\rm on} - S_{\rm off}$ (S is obtained by (7.10)), to the above function.

Chapter 8

Results

8.1 Overview

After the description of observations of the Vela pulsar in Section 8.2, the analysis in this chapter will be presented as follows:

In Section 8.3, the search for continuous emission from a gamma-ray source will be made using the image analysis. After noise cleaning of the raw data and the selections related to the image shape, a search for gamma-ray emission from the direction of the Vela pulsar will be made using the canonical selections. Then, the area of search will be extended around the pulsar, and the mapping by the symmetrical SPDF will be applied to the data. If any positive excess is found in the data, its Asymmetry distribution will be checked for compatibility with the Asymmetry distribution of gamma-ray images. Further enhancement of gamma-ray events will be tried using the asymmetrical SPDF. Then, the position and size of the gamma-ray emission region will be estimated using the modified PSF described in Chapter 7.

In Section 8.4, a search for periodic gamma-ray emission will be made about the Vela pulsar and any detected gamma-ray signal. The periodicity search will be done at the pulsar period given by radio observations and for a region around the fundamental period.

In Section 8.5, the detected gamma-ray flux or the flux upper limit to the gamma-ray

Year		Raw		Selected	
		(hours)	(events)	(hours)	(events)
1993	on-source	47.6	161614	32.6	116873
	off-source	42.8	125662	32.6	103309
1994	on-source	69.7	295732	41.9	194795
	off-source	61.9	227122	41.9	162029
1995	on-source	56.5	237474	44.9	183262
	off-source	51.8	196231	44.9	169425
total	on-source	173.8	694820	119.4	494930
	off-source	156.5	549015	119.4	434763

Table 8.1: A summary of observations of the Vela pulsar with the CANGAROO 3.8 m telescope.

signal will be estimated. Variability of the gamma-ray flux will also be investigated.

8.2 Observations of the Vela Pulsar

The Vela pulsar has been observed by the CANGAROO 3.8 m telescope for four years so far. However, the 1992 data include many noises since it was immediately after the installation of the telescope and the data are not used in the following analysis. The other observations are summarized in Table 8.1.

We usually take long on/off tracking ($2 \sim 5$ hours each) in our observations instead of the short ones (about 30 minutes each) taken at the Whipple observatory. This long on/off tracking can maximize the on-source exposure time, but is more affected by the change of the atmosphere. The raw data summarized in Table 8.1 includes the events for which no corresponding on-source or off-source observation has been done in the same atmospheric conditions or through the same horizontal coordinates. To estimate a continuous signal from a certain source comparing an on-source event count with an off-source one, the horizontal coordinates of the observations should be same between on-source and off-source since the threshold energy for gamma rays depends on the source elevation. First, to reject such events and to equalize conditions in the observations, rough selections are applied to all of the data taking into account the weather, the horizontal coordinates, transient noises and compatibility of PMT gains between on-source and off-source observations. The number of the selected events are also summarized in Table 8.1, and these events are used in the estimation of continuous emission in the next chapter. However, all of the raw data are used in the period analyses since the off-source events are not necessary and the change of the atmospheric conditions does not affect the results much.

8.3 Image Analysis

8.3.1 Noise Rejection and the Selections Related to Image Shape

A large difference in number between the on-source and off-source events remains even after matching runs by weather conditions and horizontal coordinates because noise events are still included. Selections to reject the noise events are applied to the data as described in Chapter 7. The remaining event counts are shown in the left column of Table 8.2. Here, the large difference of Table 8.1 has disappeared. Since the 1993 data include more noises than the other data, a severer selection for noise is applied to the 1993 data and the fraction of rejected events is higher than the others. Next, images near the edge of the camera are rejected as described in Chapter 7, and then the selections for the image shape parameters (Width, Length, Conc) are applied. After the selections for the image shape, an excess at 3.3 σ level has already been detected in the total event counts. Only the events selected by the image shape, listed in the right column of Table 8.2, will be used in all of the following analysis.

Year		Noise Rejection (events)	Edge Selection (events)	Shape Selections (events)
1993	on-source	36665	18226	3778
	off-source	35438	17709	3592
1994	on-source	88966	41039	12097
	off-source	88827	41110	11799
1995	on-source	100519	40141	9230
	off-source	101304	40662	8990
total	on-source	226150	99406	25105
	off-source	225569	99481	24381

Table 8.2: Changes of remaining event counts by the sequential selections.

8.3.2 Search for a Gamma-Ray Source at the Vela Pulsar

Gamma rays should be searched from the position of the Vela pulsar at first. The image parameters Distance and Alpha have been calculated with respect to the pulsar position in the field of view, and Alpha distributions of all events selected by Distance are shown in Figure 8.1. If the Vela pulsar is a VHE gamma-ray source, a narrow peak of excess counts should be found near Alpha = 0° as described in Chapter 4. In fact, a remarkable excess of the on-source counts exists near Alpha = 0°. The statistical significance of the excess of Alpha $\leq 10°$ is at 3.5 σ level. However, this peak is broader than the peak of a point source, compared with the Alpha distribution of Figure 4.6. Selecting events with Alpha $\leq 20°$ instead of Alpha $\leq 10°$, the significance of the excess is enhanced to 4.4 σ. Alpha distributions are also plotted year by year in Figure 8.2. An excess of the on-source counts is found near Alpha = 0° in each year's Alpha distribution. Counts of the remaining events are summarized in Table 8.3.

There are two possibilities for the broadness of the Alpha peak; an extended gamma-

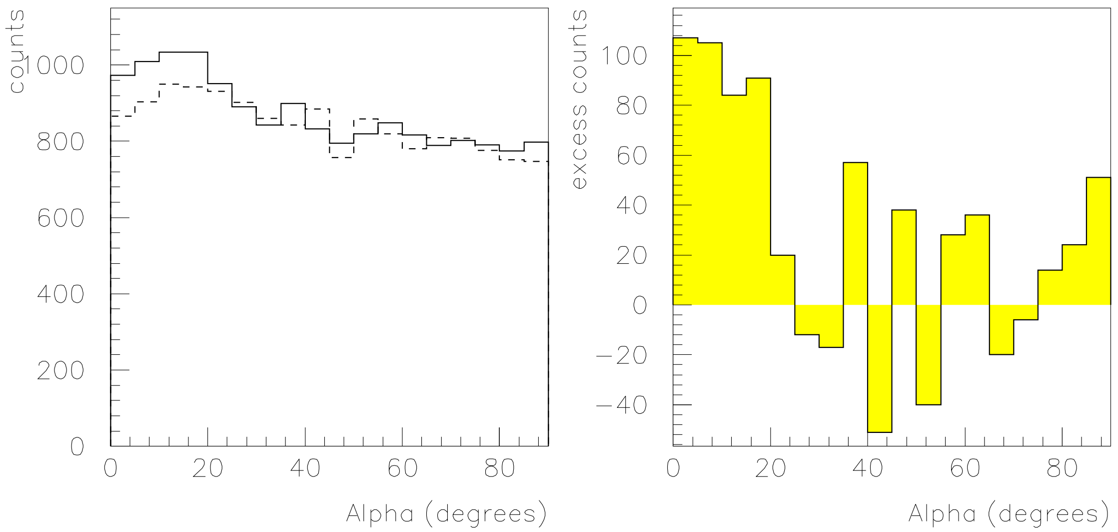

Figure 8.1: Alpha distributions for all of the data sets of the Vela pulsar after the image shape selections and the Distance selection. In the left figure, the histogram represented by the solid line is the distribution of on-source data and the dashed line is of off-source data. The right histogram is the distribution of excess counts.

ray source exists in the direction of the Vela pulsar, or a gamma-ray source exists near the direction of the Vela pulsar with a small offset between them. In both of the cases, one can easily understand the broadening of the Alpha peak since the fraction of the images pointing to directions offset with respect to the Vela pulsar increases. Alpha distributions due to gamma rays from some extended sources have been obtained by Monte Carlo simulations and shown in Figure 8.3. Indeed, the broader distribution can be seen as the source is more extended.

Since background images should not have any directionality, we can expect the Alpha distribution of background images to be flat. The Alpha distribution after reducing the edge

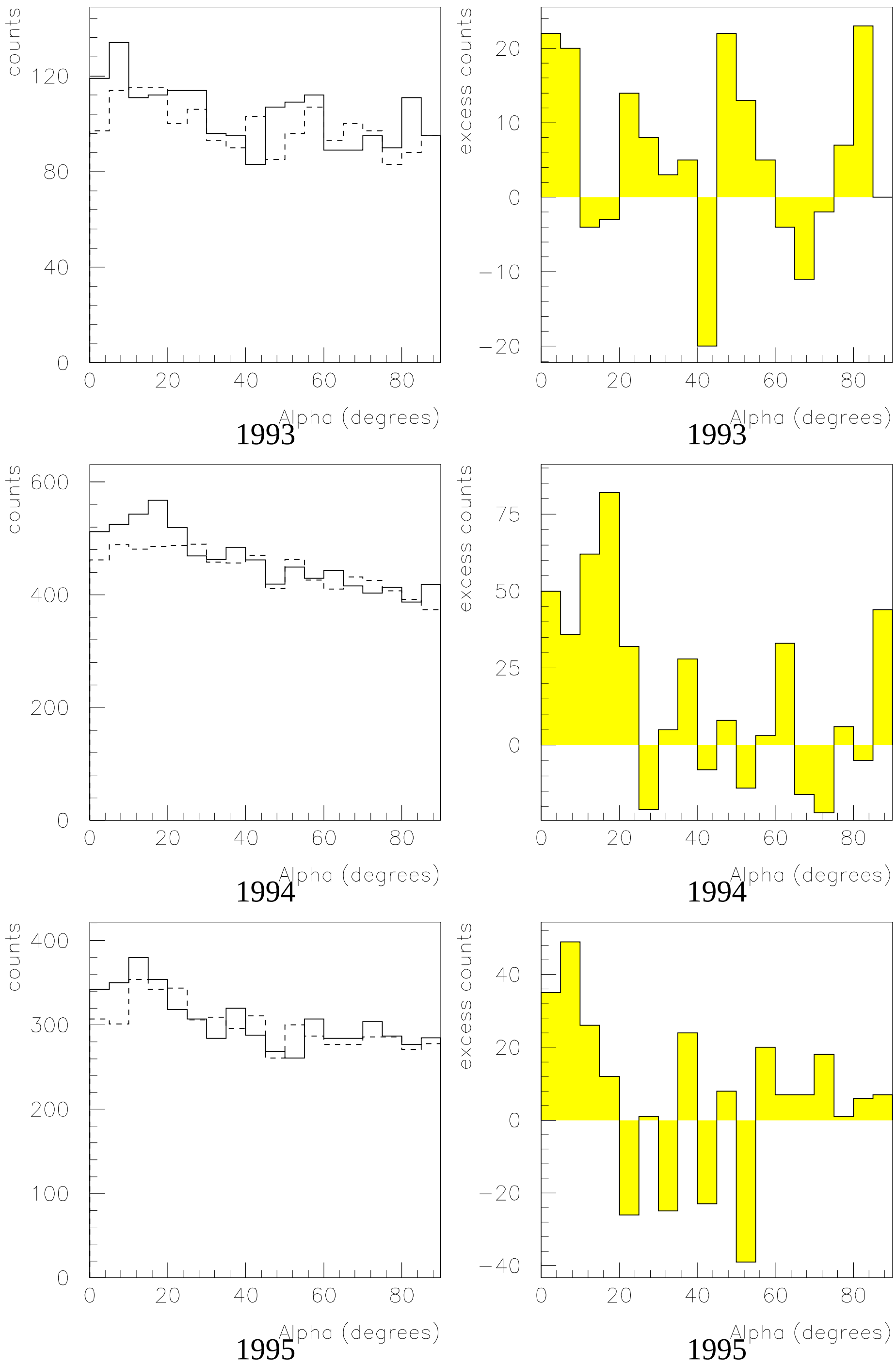

Figure 8.2: Alpha distributions for each year's data sets of the Vela pulsar. Distributions are plotted in the same way as Figure 8.1.

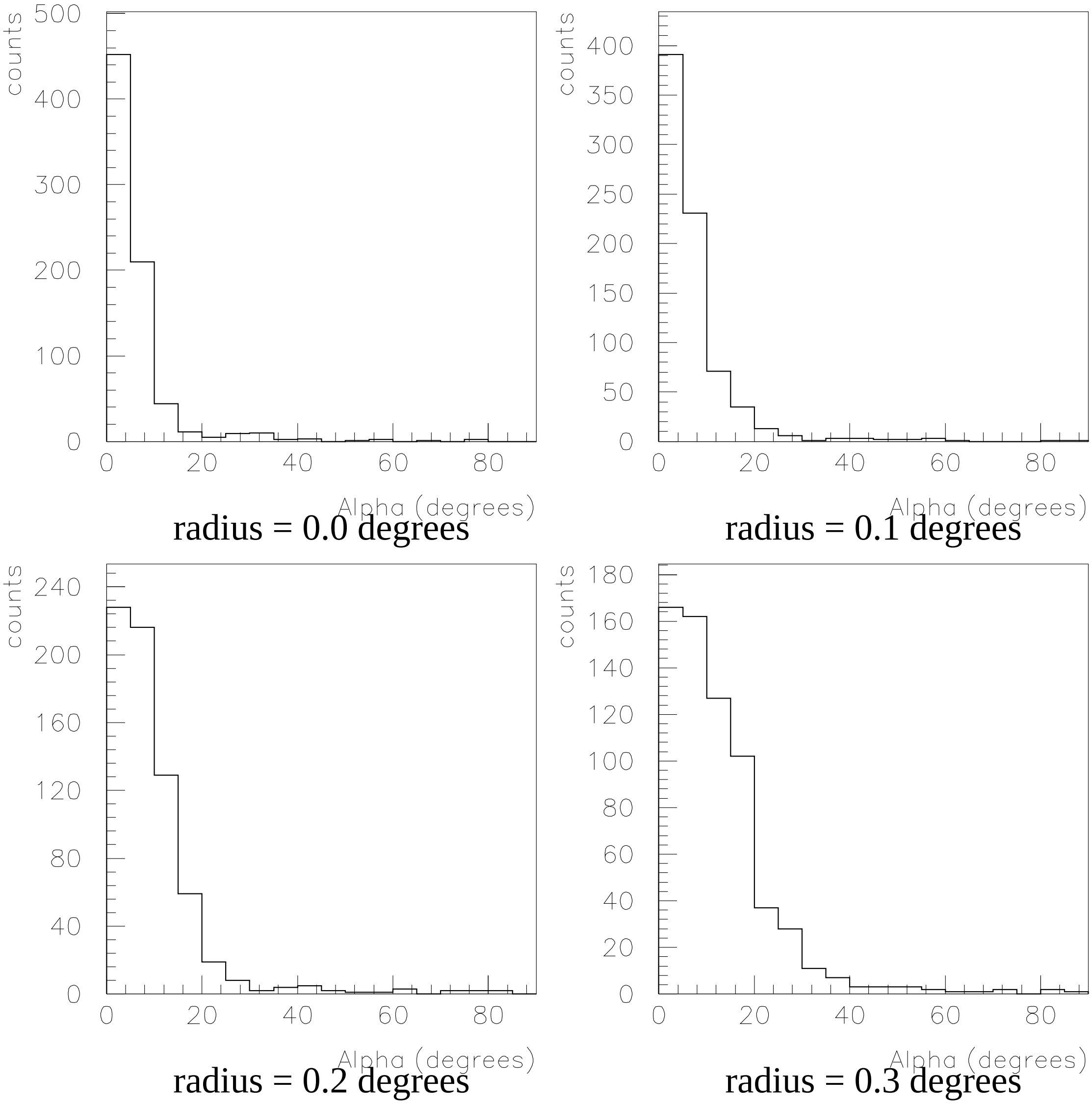

Figure 8.3: Simulated Alpha distributions due to gamma rays from extended sources. In the simulations, gamma rays have uniformly been emitted from the circular areas whose radii are described under the figures.

Year		Distance Selection (events)	Alpha $\leq 10°$ (events)	Alpha $\leq 20°$ (events)
1993	on-source	1875	253	476
	off-source	1777	211	441
	excess	98 (1.6 σ)	42 (1.9 σ)	35 (1.2 σ)
1994	on-source	8322	1037	2148
	off-source	8019	951	1918
	excess	303 (2.4 σ)	86 (1.9 σ)	230 (3.6 σ)
1995	on-source	5501	692	1426
	off-source	5393	608	1304
	excess	108 (1.0 σ)	84 (2.3 σ)	122 (2.3 σ)
total	on-source	15698	1982	4050
	off-source	15189	1770	3663
	excess	509 (2.9 σ)	212 (3.5 σ)	387 (4.4 σ)

Table 8.3: Changes of remaining event counts after the selection of Distance and Alpha. Distance and Alpha for every event have been calculated with respect to the position of the Vela pulsar.

effect is indeed flat as shown in Figure 7.4. However after the application of the canonical gamma-ray selections, the Alpha distributions of background images in Figure 8.1 and Figure 8.2 do not look flat, and have bumps near Alpha $= 20°$ and gradually decrease as Alpha increases. This fact may be explained assuming that the edge effect has not been rejected completely. If images are selected by their distance from the center of the camera with the above edge selection (the source is assumed to be at the center of the camera), the images with narrow shape and smaller Alpha are susceptive to this effect because the effect always increase the Alpha value larger than the presumed value of about $\sim 0°$ producing a

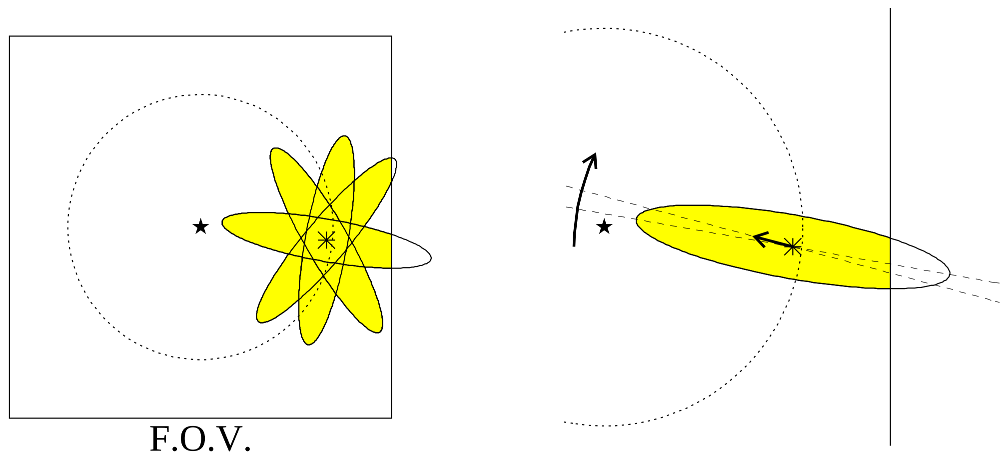

Figure 8.4: Schematic diagrams to explain hypotheses for the shape of background Alpha distributions after the canonical selections. The solid line represents the edge of the camera and the dotted line represent the boundary line of the edge selection. Of the narrow images near the boundary, images with small Alphas are susceptive to the edge effect because the effect always increase the Alpha value larger than the presumed value of about $\sim 0°$ producing a bump around Alpha $= 20°$ in the Alpha distribution. The centroid of such images are also drawn into the inside of the camera.

bump around Alpha $= 20°$ in the Alpha distribution. This effect is schematically shown in Figure 8.4. Furthermore, the edge-affected images of small Alpha are drawn into the inside of the camera and easy to pass the edge selection. Thus, the part of the distribution with small Alphas will be higher than the part with large Alphas. This hypotheses should be confirmed by Monte Carlo simulation, but this confirmation takes a very long CPU time and is still in progress.

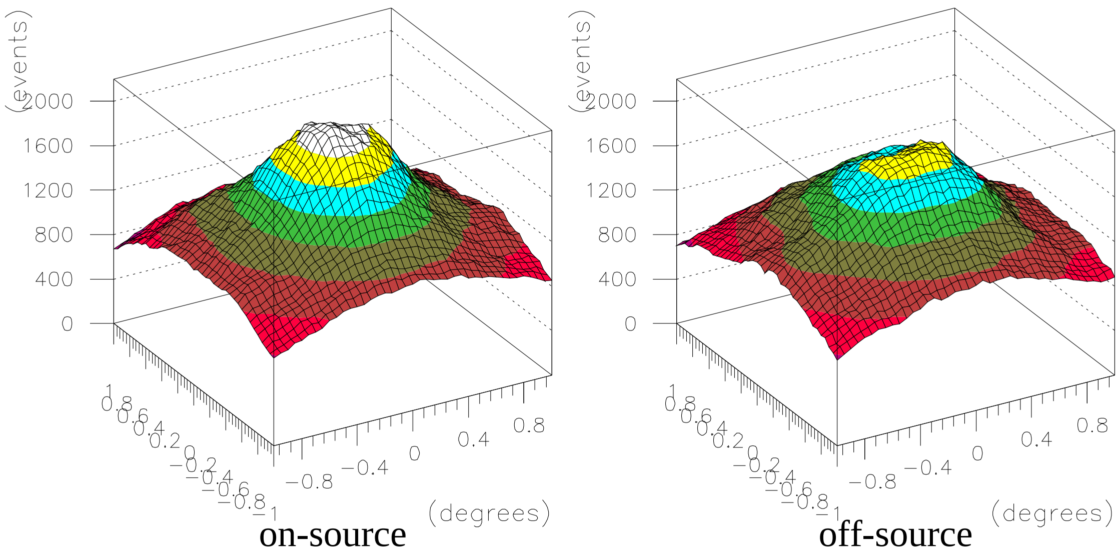

Figure 8.5: Histograms of number of events passing the gamma-ray selection criteria of (7.1) ∼ (7.3). The on-source histogram is on the left and the off-source histogram is on the right.

8.3.3 Search for a Gamma-Ray Source around the Vela Pulsar

As mentioned above, it is possible that a gamma-ray source exists at a direction different from, but near to, the Vela pulsar, and the field of view around the pulsar should be searched. Here, the field of view less than about 1° from the Vela pulsar is searched by the conventional method and the method using the symmetrical SPDF as described in Chapter 7.

The conventional method is first applied to search for a gamma-ray source. As described in Chapter 7, a grid is overlapped on the field of view centered on the pulsar, and image parameters are calculated for each event and every mesh point. Two-dimensional histograms for all the events passing the gamma-ray selection criteria of (7.1) ∼ (7.3) are shown in Figure 8.5. In these histograms, the center of the horizontal axes is taken to coincide with

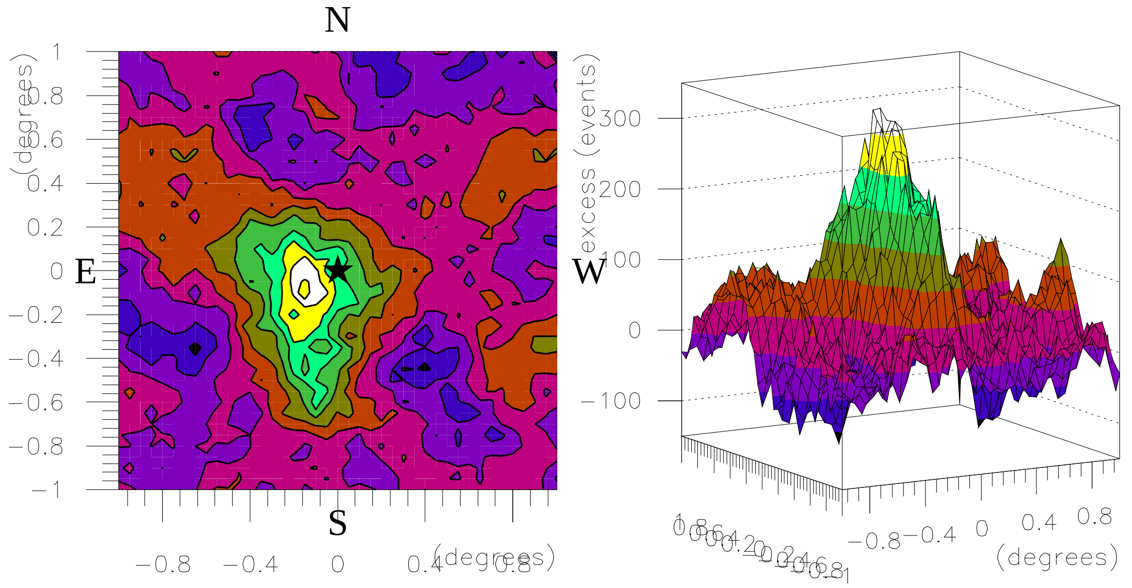

Figure 8.6: A histogram of excess counts of the on-source events (the difference between the histograms of Figure 8.5). The origin of horizontal axes are taken to coincide with the Vela pulsar ($\star$), and the positive y direction is the direction of the north.

the pulsar, and the positive x direction is the west and the positive y direction is the north. It is apparent that the histograms remarkably differ near the center, that is, near the pulsar. Although the off-source (background) histogram has a raised structure in the center of the field of view, this is because the effective area is smaller in the region outside of the field of view. A histogram of excess counts is given after subtracting the off-source histogram from the on-source histogram, and it is shown in Figure 8.6. A remarkable peak is found at $0°.1 \sim 0°.2$ southeast from the pulsar. This peak is statistically significant, and the maximum significance of the excess counts given by (7.6) is 5.3 σ at $(-0°.15, 0°.0)$, which corresponds to the probability of 4.0×10^{-8}.

To get a more precise position of the above peak of excess counts, the method using the

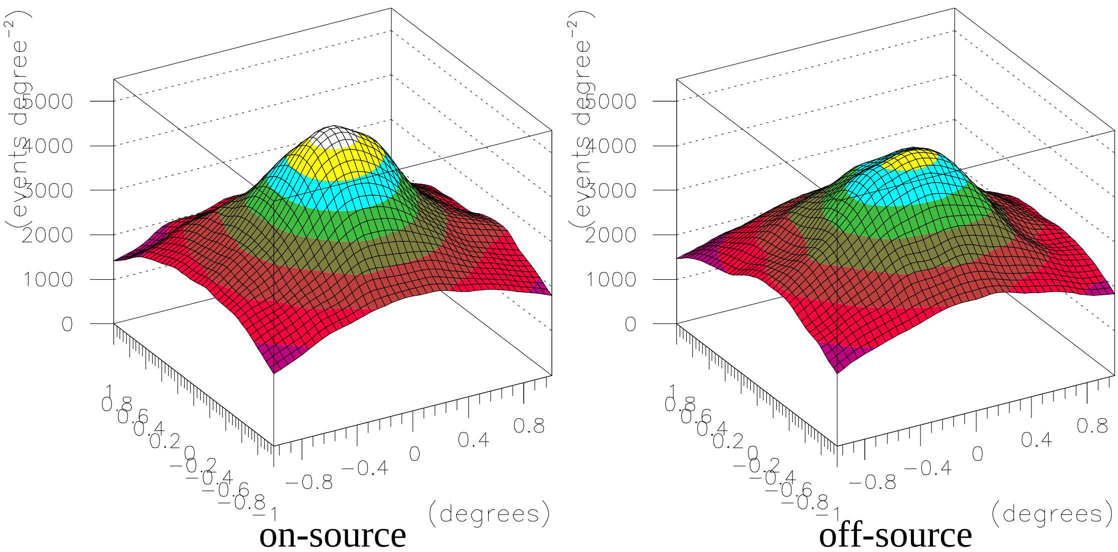

Figure 8.7: Distributions of event density given by superimposing symmetrical SPDFs for all of the on-source and off-source data. The left is of the on-source data and the right is of the off-source data.

symmetrical SPDF is applied to the same data set. The on-source and off-source distributions of event density given after superposition of SPDFs are shown in Figure 8.7. The shapes of the distributions are almost the same as the histograms given by the conventional method (Figure 8.6). A distribution of excess event density is given by subtracting the off-source distribution from the on-source distribution, and it is shown in Figure 8.8. A peak of excess event density is found at almost the same position as in Figure 8.6, but it is naturally smoothed by the use of the SPDF. The maximum statistical significance of this excess is 5.3 σ at $(-0^{\circ}.1, -0^{\circ}.05)$ and it is of the same level as of the conventional method. The shape of this peak looks broader than that of the PSF for the SPDF shown in Figure 7.11, and it may imply that the gamma-ray source is extended. This will be further discussed in the

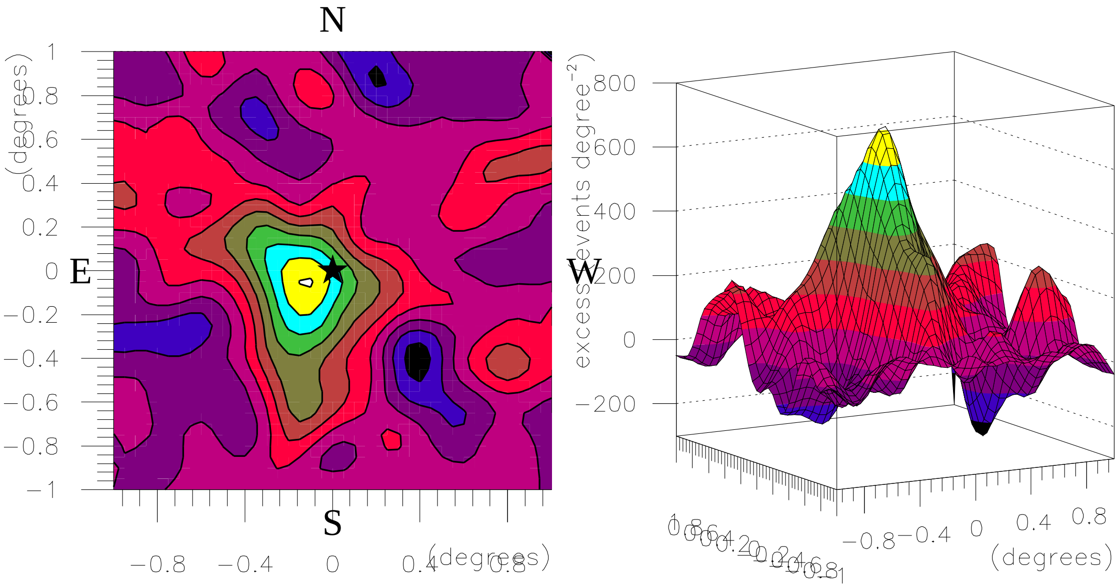

Figure 8.8: A distribution of excess event density of the on-source events (the difference between the on-source and off-source distributions of Figure 8.7). The coordinates are taken to be the same as of Figure 8.6.

following.

The above distribution of excess event density is divided into each year's distributions in Figure 8.9. A peak of excess event density is still seen in each year's distribution, and their positions are nearly the same as of Figure 8.8 although the peaks are not clear as they are affected by the background fluctuation. Their statistical significances are still more than 3 σ in each year.

Here, Alpha distributions are recalculated because the gamma-ray source position appears to be different from the pulsar position as obtained from the symmetrical SPDF method. Assuming that the most probable source position differs by $(-0^{\circ}.1, -0^{\circ}.05)$ from the pulsar, Alpha distributions for all observed data with respect to this position are shown in

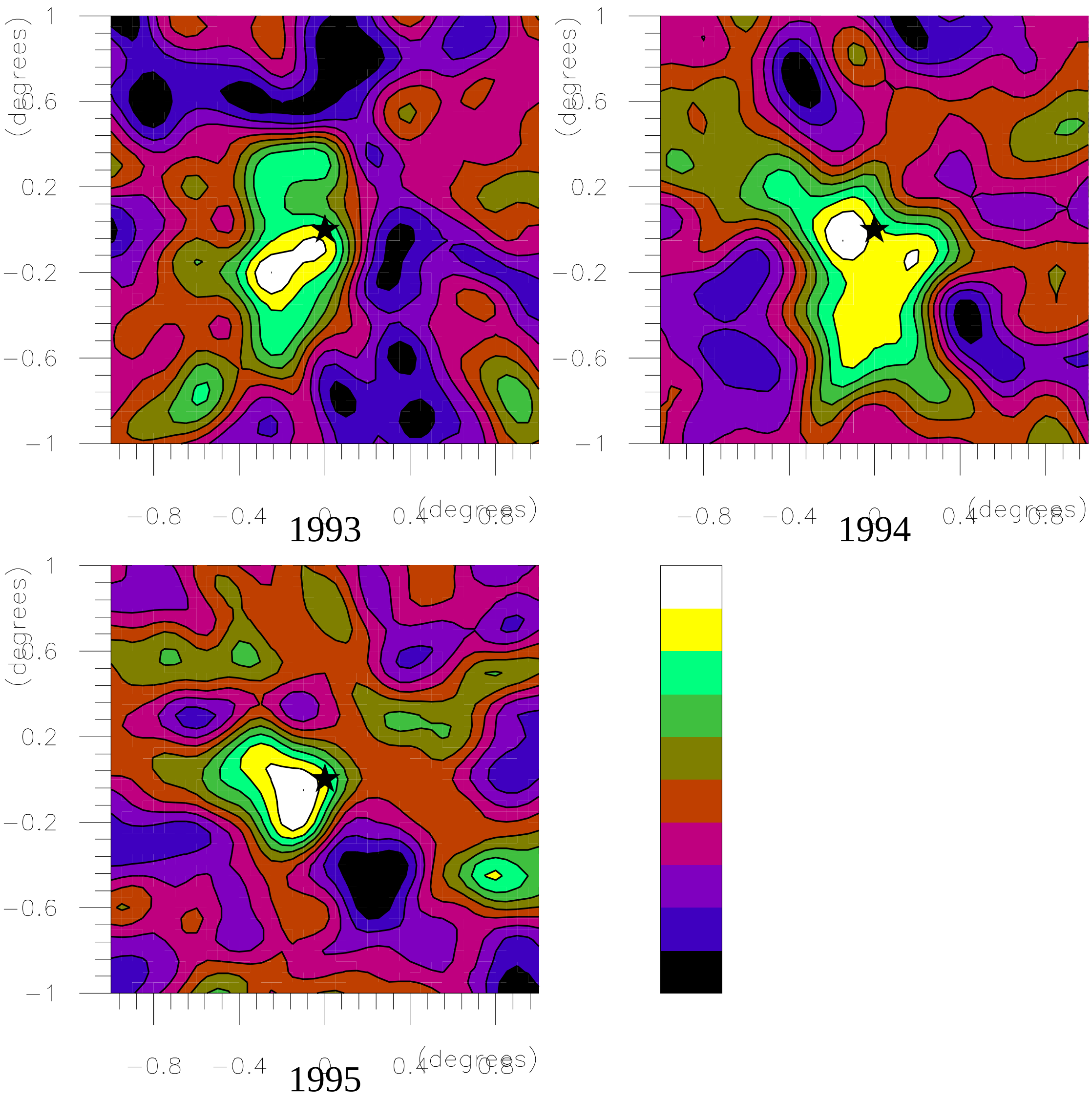

Figure 8.9: Distributions of excess event density for each year's data sets. The contour levels have been taken so as to divide each distribution to 10 levels between the minimum and maximum values of the distribution.

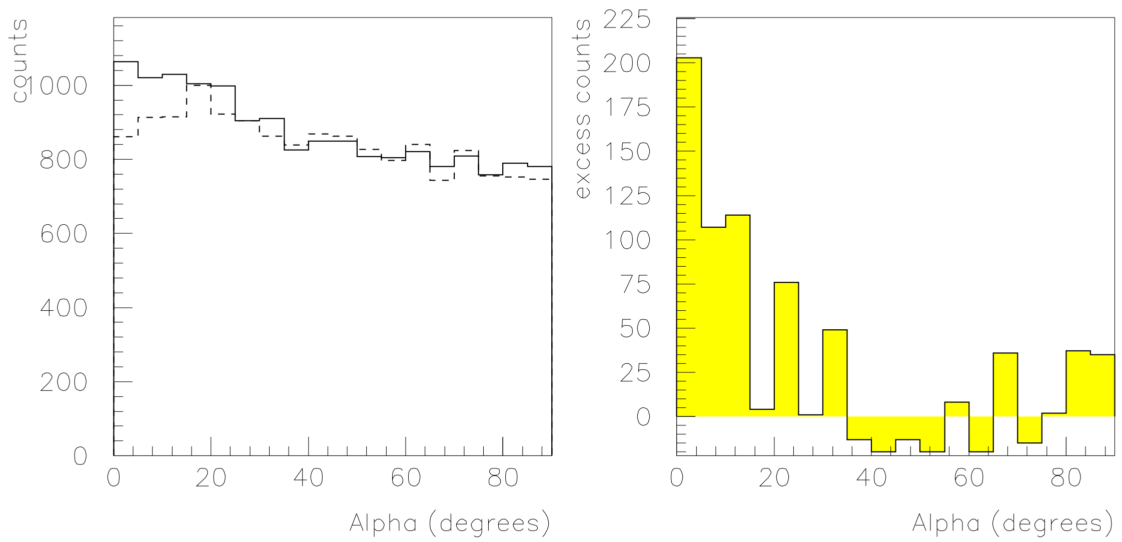

Figure 8.10: Alpha distributions with respect to the peak position of excess event density in Figure 8.8 for all observed data.

Figure 8.10. The peak of excess counts near Alpha = 0° is obviously sharper than the peak obtained for the pulsar position. The Alpha distributions for each year's data set are also plotted in Figure 8.11. Each peak of excess count near Alpha = 0° is not significant, but roughly looks sharper than the peak obtained for the pulsar position. The numbers of remaining events passing through the Distance and Alpha selections are summarized in Table 8.4.

Figure 8.12 shows the Alpha distributions of the events rejected by the gamma-ray selections of (7.1) ∼ (7.2) (Width, Length, Conc and Distance). The flat distributions of the on-source and off-source events are obtained in the left histograms and no significant peaks appear in the excess distribution. The distributions seem to be due to only background events and this means that the above gamma-ray selections are reliable. To investigate from

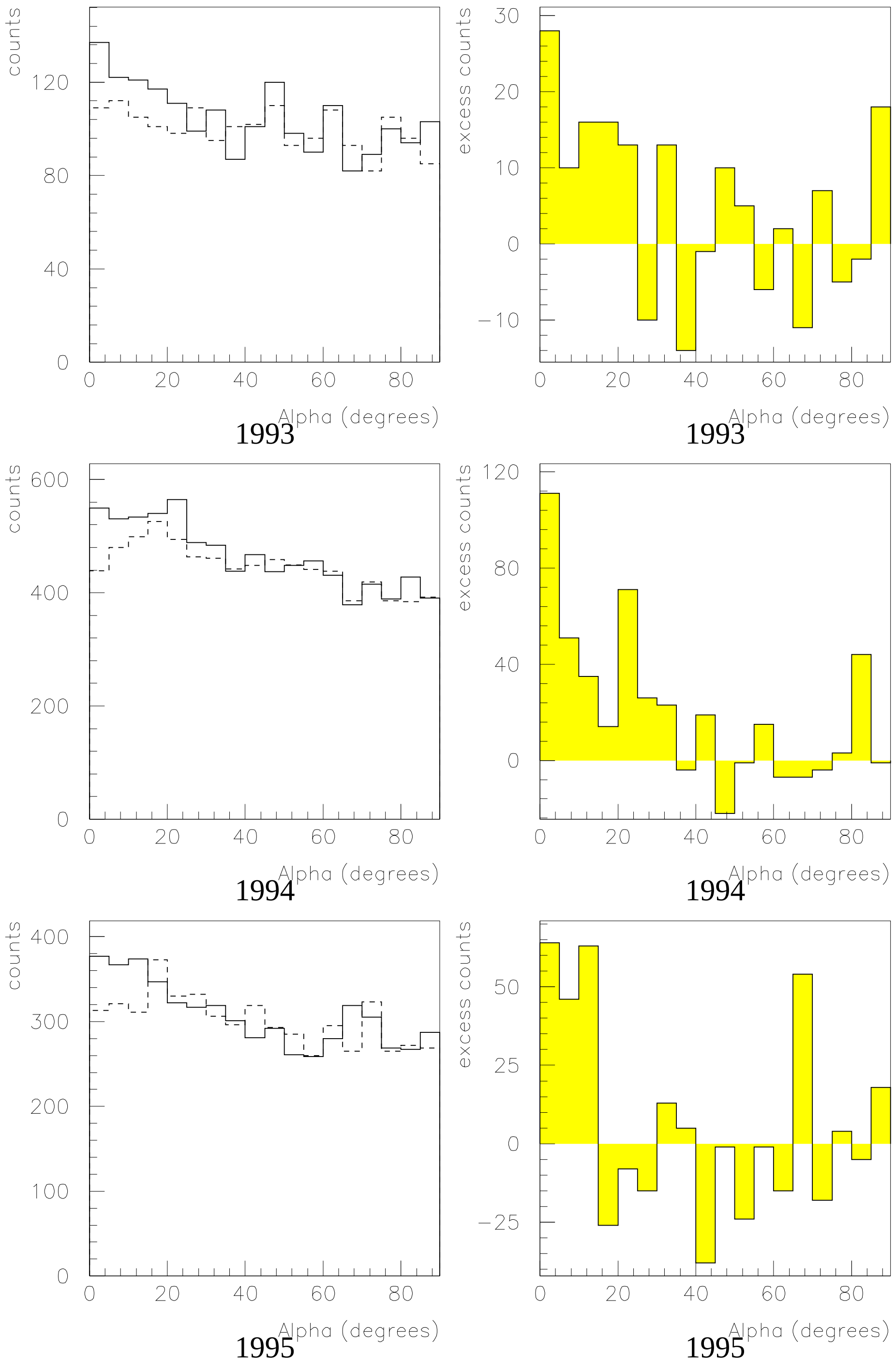

Figure 8.11: Alpha distributions with respect to the peak position of excess event density in Figure 8.8 for each year's data.

Year		Distance Selection (events)	Alpha $\leq 10°$ (events)	Alpha $\leq 20°$ (events)
1993	on-source	1889	259	497
	off-source	1800	221	427
	excess	89 (1.5 σ)	38 (1.7 σ)	70 (2.3 σ)
1994	on-source	8372	1081	2155
	off-source	8006	919	1944
	excess	366 (2.9 σ)	162 (3.6 σ)	211 (3.3 σ)
1995	on-source	5544	744	1465
	off-source	5428	634	1318
	excess	116 (1.1 σ)	110 (3.0 σ)	147 (2.8 σ)
total	on-source	15805	2084	4117
	off-source	15234	1774	3689
	excess	571 (3.2 σ)	310 (5.0 σ)	428 (4.8 σ)

Table 8.4: Changes of remaining event counts after the selection of Distance and Alpha. Distance and Alpha for every event have been calculated with respect to the peak position of the excess event density distribution of Figure 8.8.

another viewpoint whether the above peak of excess events is due to VHE gamma rays, the tendency of Asymmetry distributions is checked for the events selected with respect to the above peak position. The gamma-ray selection criteria of (7.1) $\sim$ (7.3) are applied to parameters calculated with respect to the peak position which differs by $(-0°.1, -0°.05)$ from the pulsar, and Asymmetry is calculated using (7.7). The resultant Asymmetry distributions are shown in Figure 8.13. The left histograms in Figure 8.13 represent the on-source and off-source distributions, and their differences, $N_{\rm on} - N_{\rm off}$, are plotted on the right. The Asymmetry distribution of gamma-ray images should be one-sided with the peak on the positive

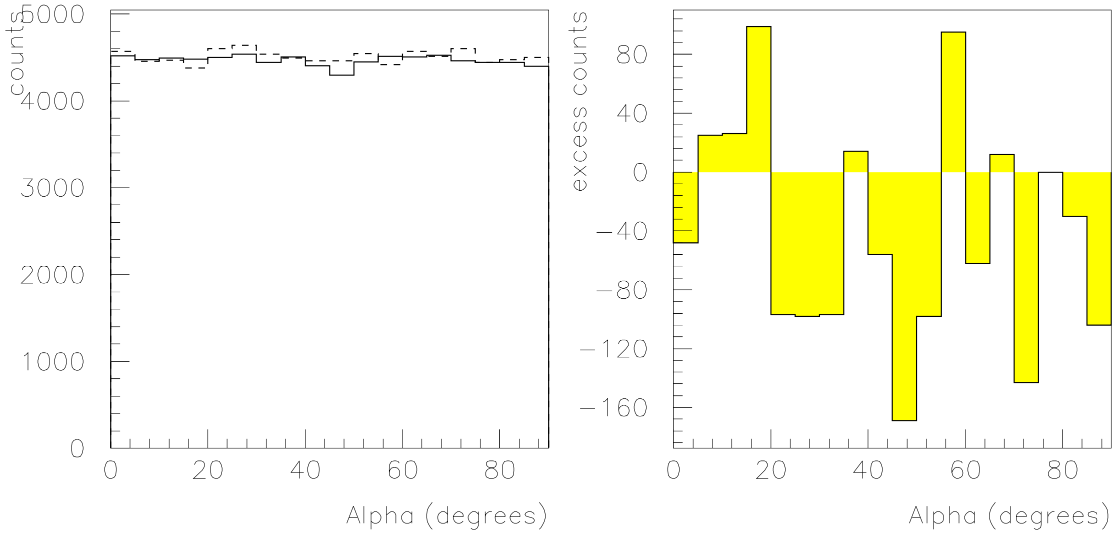

Figure 8.12: Alpha distributions of the events rejected by the criteria of (7.1) $\sim$ (7.2). The solid line in the left figure represents the distribution of the on-source events, while the dashed line is the off-source distribution. The right histogram is the distribution of the excess events.

side. The on-source histograms still include many background events, therefore the numbers of events with negative Asymmetry are almost the same as in positive Asymmetry, as seen in the simulated proton distribution of Figure 7.6. However, the excess in the Asymmetry distributions of Figure 8.13 are one-sided on the positive side as expected for gamma-ray events, and similar excesses are detected in each year. The ratio of the number of excess events in the positive side to in the negative side is similar to the ratio in the simulated gamma-ray distribution of Figure 8.13. This result is strong evidence that the detected excess events of Figure 8.8 are due to VHE gamma rays.

The above tendency in Asymmetry should be effective in further enhancement of the gamma-ray events. Therefore, the asymmetrical SPDF proposed in Chapter 7 is applied to

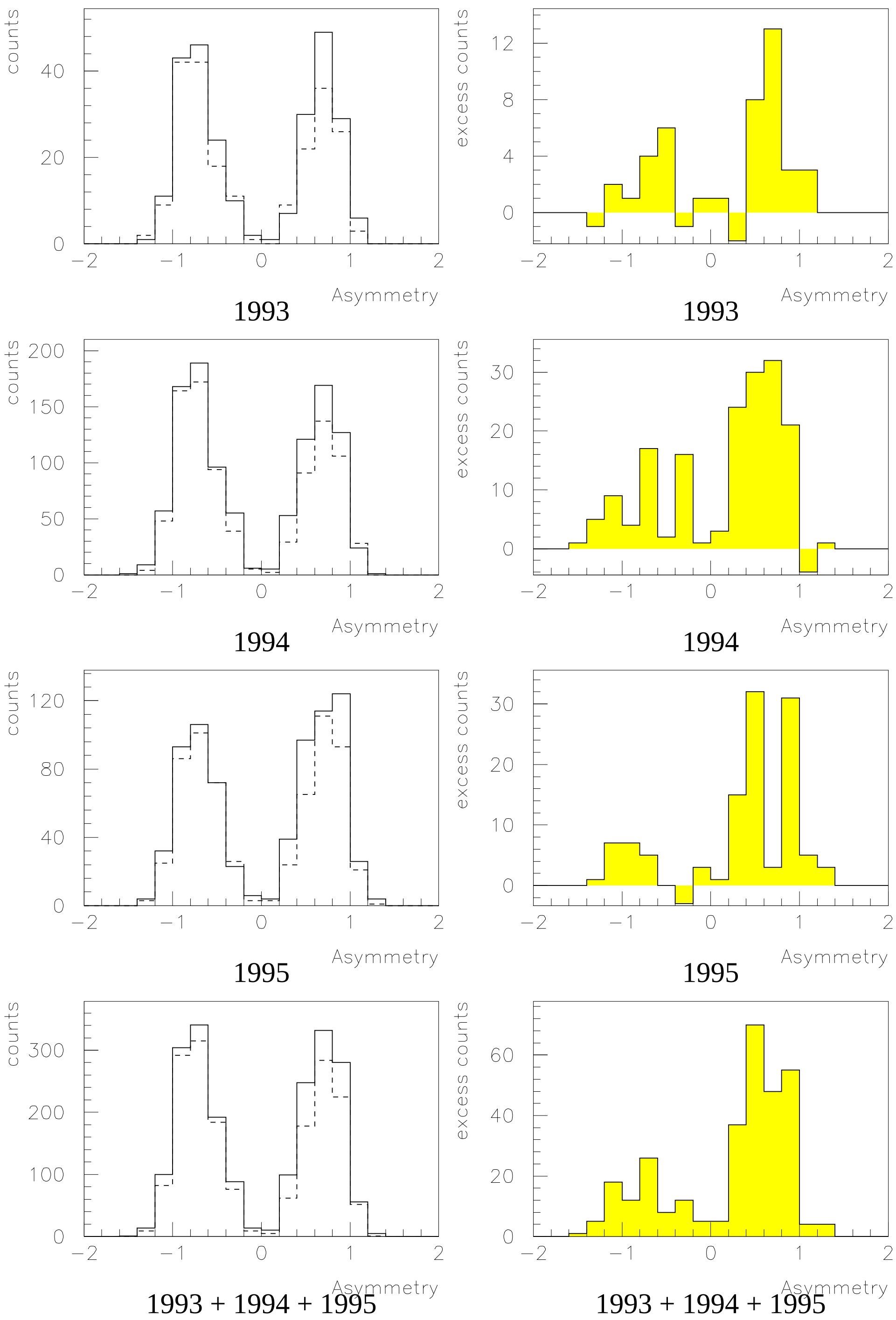

Figure 8.13: Asymmetry distributions for the events selected by the criteria of (7.1) $\sim$ (7.3). The solid lines in the left figures represent distributions of the on-source events, while the dashed lines are the off-source distributions. The right histograms are distributions of the excess events.

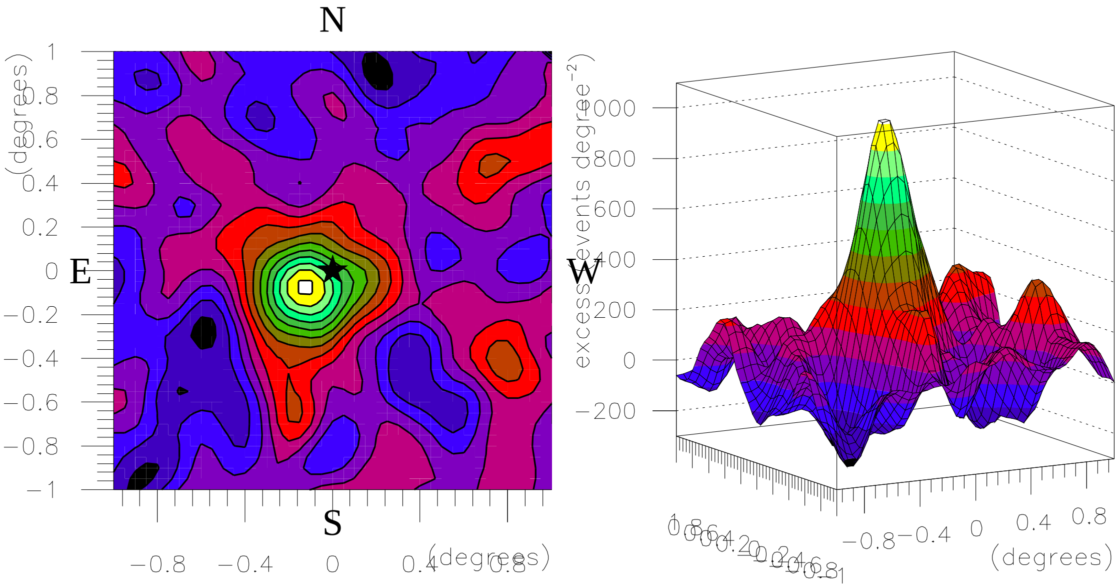

Figure 8.14: The distribution of excess event density of the on-source events given by superpositions of asymmetrical SPDFs. The coordinates are taken to be the same as of Figure 8.6.

the data in the same way as the case of the symmetrical SPDF. The resultant distribution of excess event density for all observed data is shown in Figure 8.14. The peak of excess event density has become more significant as expected *a priori*, and the statistical significance is 6.2 σ at the peak maximum of $(-0^{\circ}.1, -0^{\circ}.1)$, which is slightly shifted from the peak maximum in Figure 8.8. Furthermore, the shape of the peak has become sharper than that of Figure 8.8, and the rather extended feature of the peak in Figure 8.8 has not been enhanced. The extended feature is possibly due to a fluctuation of the background. The same plot is obtained for each year in Figure 8.15. The peak at about 4 σ level is obtained in each year and also looks sharper than the corresponding peak of Figure 8.9.

The above result means that the use of the image asymmetry is effective in enhancing

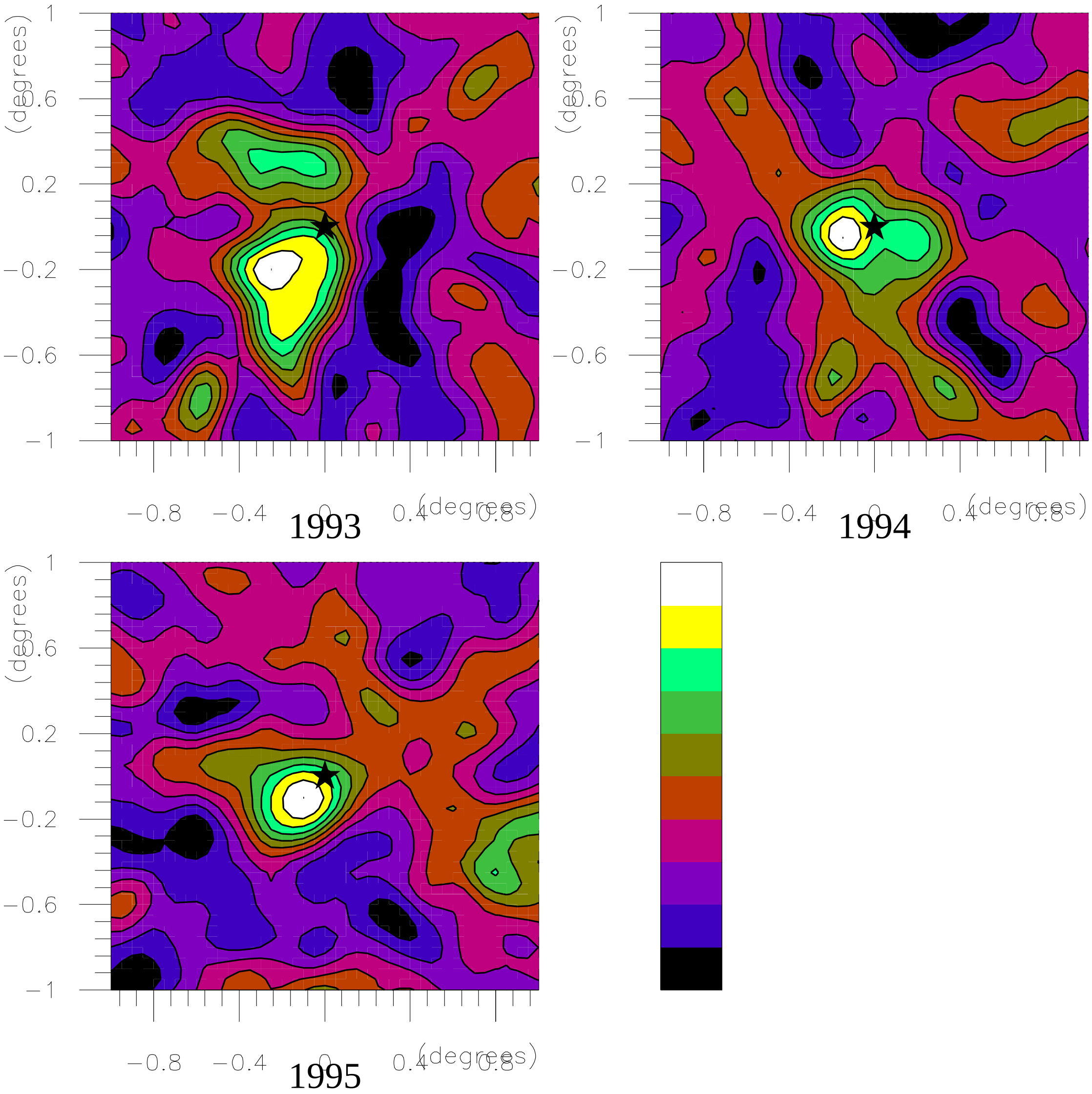

Figure 8.15: Distributions of excess event density for each year's data sets given by superpositions of asymmetrical SPDFs. The contour levels have been taken so as to divide each distribution into 10 levels between the minimum and maximum values of the distribution.

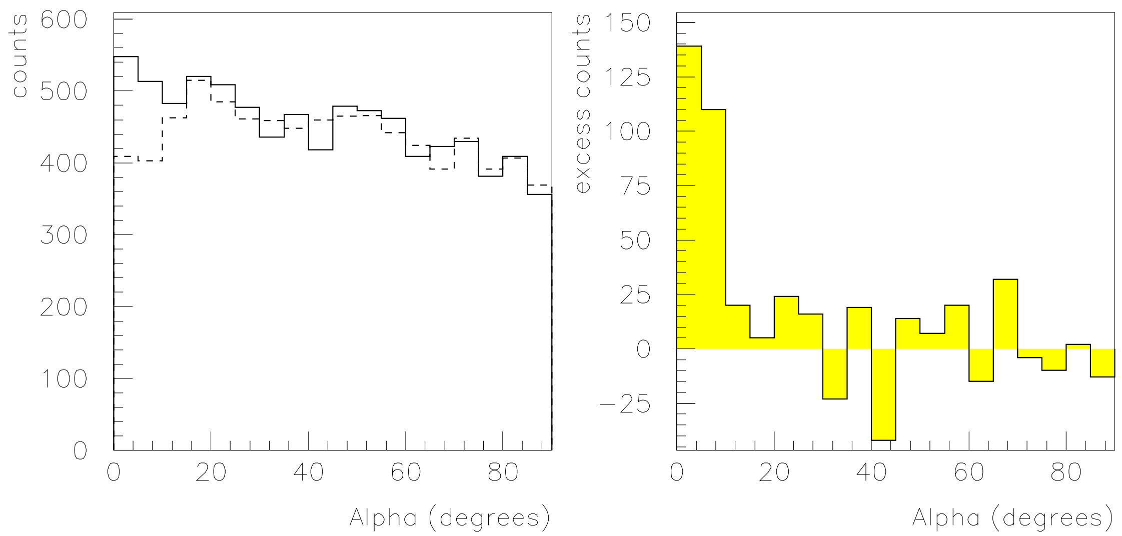

Figure 8.16: Alpha distributions obtained for the peak position of excess event density, $(-0^\circ.1, -0^\circ.1)$, in Figure 8.14 for all observed data. Asymmetry ≥ 0 is used in the gamma-ray selection together with the other parameters except for Alpha.

gamma-ray events. This fact can also be confirmed using Asymmetry conservatively. If a criterion for Asymmetry is roughly taken as

$$\text{Asymmetry} \geq 0, \tag{8.1}$$

and applied to the above data together with the other gamma-ray selection criteria except for Alpha, the Alpha distributions with respect to the peak position $(-0^\circ.1, -0^\circ.1)$ are given in Figure 8.16. The peak near Alpha $= 0^\circ$ in the excess histogram is sharper than the peak of Figure 8.10, and this fact is consistent with the sharpness of the peak in Figure 8.14. The statistical significance of the peak (Alpha $\leq 10^\circ$) is 5.8 σ.

As a summary of the image analysis, the Alpha distributions of the all observed data after the each step of the selection are shown in Figure 8.17. In this figure, the source position has

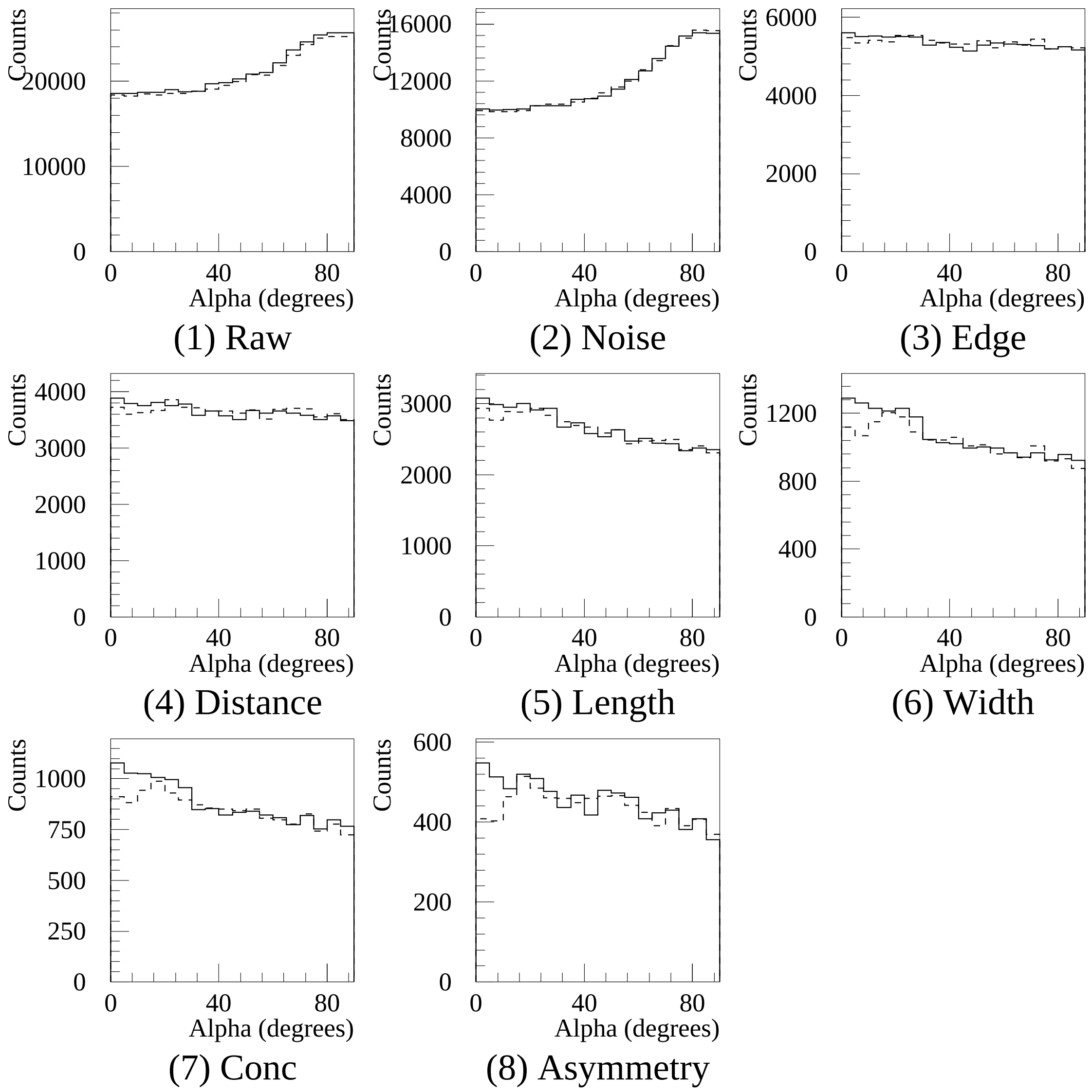

Figure 8.17: Changes of the Alpha distributions after the series of selections. The solid lines represent the on-source distributions, while the dashed lines represent the off-source distributions. The selections have applied in the order of (1) $\sim$ (8). The selection criteria are (7.1) $\sim$ (7.2) and (8.1). The source position is assumed to be at $(-0^{\circ}.1, -0^{\circ}.1)$.

been assumed to be at $(-0^\circ.1, -0^\circ.1)$, and the selections have been applied in the order of (1) $\sim$ (8). It can be seen that the excess of the on-source events near Alpha $= 0^\circ$ has been enhanced step by step. Figure 8.18 shows these excess distributions in terms of significance. The significance of the Alpha peak increases as more gamma-ray selections are applied.

8.4 Period Analysis

The periodicity of the events from the Vela pulsar and the direction of the above gamma-ray-like peak is investigated in this section. The search for pulsed emission has been done for the three kinds of data sets; (1) after the noise rejection described in Chapter 7, (2) after (1) and the canonical gamma-ray selections of (7.1) $\sim$ (7.3) and (3) after (2) and the Asymmetry selection of (8.1). Here, the events rejected in the above analyses due to the differences of the conditions between the on-source observations and the off-source observations are revived, but the data observed in 1993 are not included in the analysis since the GPS system had not been installed during 1993 observations. Numbers of events used in the period analysis are summarized in Table 8.5. The excess position has been taken to be offset by $(-0^\circ.1, -0^\circ.1)$ from the pulsar. If the events having corresponding off-source observations are taken out from the events of Table 8.5 and the event count is compared with the off-source event count, 4.7 σ excess events are still included with respect to the excess position. The fraction of the excess events is about 15 % of the total events after the selections.

8.4.1 Method of the Analysis

The arrival time of each event must be first transformed to the solar system barycentric (SSB) arrival time because of the relatively short period of the Vela pulsar ($\sim$ 89 msec). A derivative of the TEMPO programs [116] is used for the transformation of the event arrival times. The solar system ephemeris used in the analysis comes from the Jet Propulsion Laboratory (JPL) and is based on epoch 2000 (DE 200) [107]. The SSB arrival time is

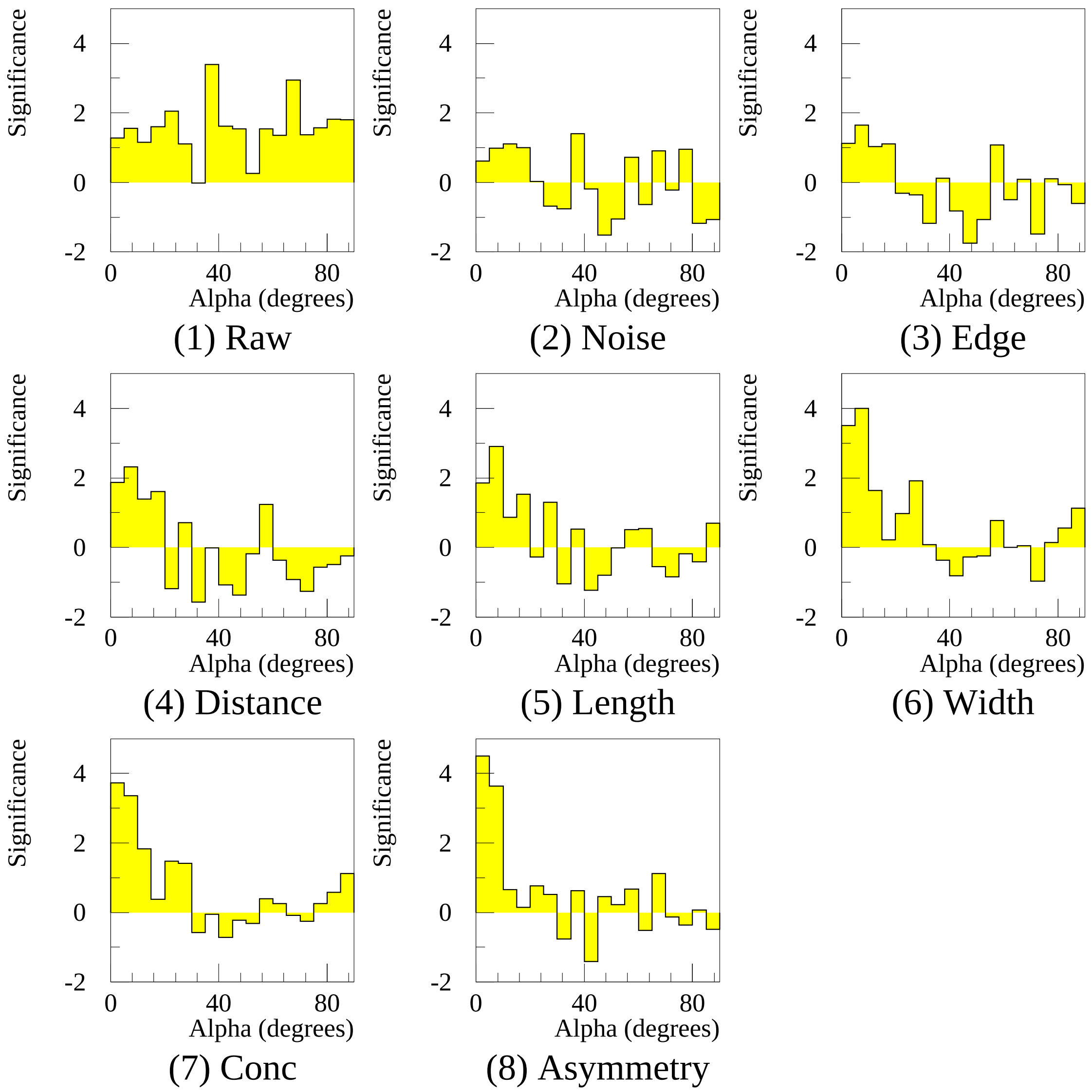

Figure 8.18: The Alpha distributions of the excess events in terms of significance after the series of selections. The selections and the source position are the same as in Figure 8.17.

Year	Kind of the data	Pulsar position (events)	Excess Position (events)
1994	(1) noise rejection	139100	139100
	(2) = (1) + canonical selections	1592	1670
	(3) = (2) + Asymmetry	748	782
1995	(1) noise rejection	117408	117408
	(2) = (1) + canonical selections	878	946
	(3) = (2) + Asymmetry	473	522
total	(1) noise rejection	256508	256508
	(2) = (1) + canonical selections	2470	2616
	(3) = (2) + Asymmetry	1221	1304

Table 8.5: Numbers of events used in the period analysis. The excess position has been taken to be offset by $(-0^\circ.1, -0^\circ.1)$ from the pulsar.

reduced to a pulsar phase according to

$$\phi = \nu \Delta T + \frac{1}{2}\dot{\nu}\Delta T^2 + \frac{1}{6}\ddot{\nu}\Delta T^3, \tag{8.2}$$

vwhere $\Delta T = T - T_0$, T is the SSB arrival time and T_0 is the reference epoch. ν, $\dot{\nu}$ and $\ddot{\nu}$ are the pulsar frequency, its first and second derivative, respectively. They comes from the radio observations and the values used in the analysis are summarized in Table 8.6. The reference epochs in Table 8.6 have already been transformed to the SSB arrival time of a radio pulse.

The most commonly used test of periodicity is the Rayleigh test. This test can be visualized by representing the N phases, $\phi_i (i = 1, \ldots, N)$, by N unit vectors, each oriented at an angle $2\pi\phi_i$ with respect to a particular direction. The Rayleigh statistic, R, is then the length of the resultant vector divided by N. However, if the lightcurve of a particular source has a narrow and double-peaked structure, for example as seen in Figure 3.1, the Rayleigh test may not be sensitive since the resultant vector is likely to be small. Therefore, the Z_n^2

Date	Epoch[a] T_0 (MJD)	Frequency ν ($\sec^{-1}$)	1st Derivative $\dot{\nu}$ (10^{-11} $\sec^{-2}$)	2nd Derivative $\ddot{\nu}$ (10^{-21} $\sec^{-3}$)
1994 Jan. 15 - Jan. 21	49353.002394239	11.1975539227276	-1.55984	0.172
1994 Feb. 5 - Mar. 12	49428.003321521	11.1974528567704	-1.55935	0.792
1995 Jan. 7	49710.002067014	11.1970840126856	-1.56447	2.36
1995 Jan. 27 - Mar. 5	49772.003547013	11.1970002349415	-1.56344	2.63

[a] The radio arrival time at the SSB.

Table 8.6: Ephemerides used in the period analysis.

test [21], which is more sensitive to the above case, is used here to investigate the periodicity of the events. The Z_n^2 statistic is defined by the following equation:

$$Z_n^2 = \frac{2}{N}\sum_{k=1}^{n}\left[\left(\sum_{i=1}^{N}\cos 2\pi k\phi_i\right)^2 + \left(\sum_{i=1}^{N}\sin 2\pi k\phi_i\right)^2\right]. \tag{8.3}$$

This statistic is equivalent to using the Rayleigh statistic if $n = 1$ and is thus the Rayleigh statistic modified to include n harmonics. For a uniform phase distribution, Z_n^2 is distributed asymptotically as $\chi^2(2n)$.

8.4.2 Results

The Z_2^2 statistics have been calculated for the data in Table 8.5 and they are listed in Table 8.7 together with the corresponding chance probabilities. The Z_2^2 column also lists the contribution from the first and second harmonics separately in parentheses. No significant value is seen in Table 8.7 and these results are consistent with no pulsed emission having been detected with the period of the Vela pulsar. The resultant lightcurves are also shown in Figure 8.19 for the events selected by the canonical criteria of (7.1) $\sim$ (7.3). No significant excess is seen in any phase bin.

To calculate the upper limit to the pulsed gamma-ray fraction in the data, we assume the pulse profile to be of a delta function, which is more appropriate for the Vela pulsar than a

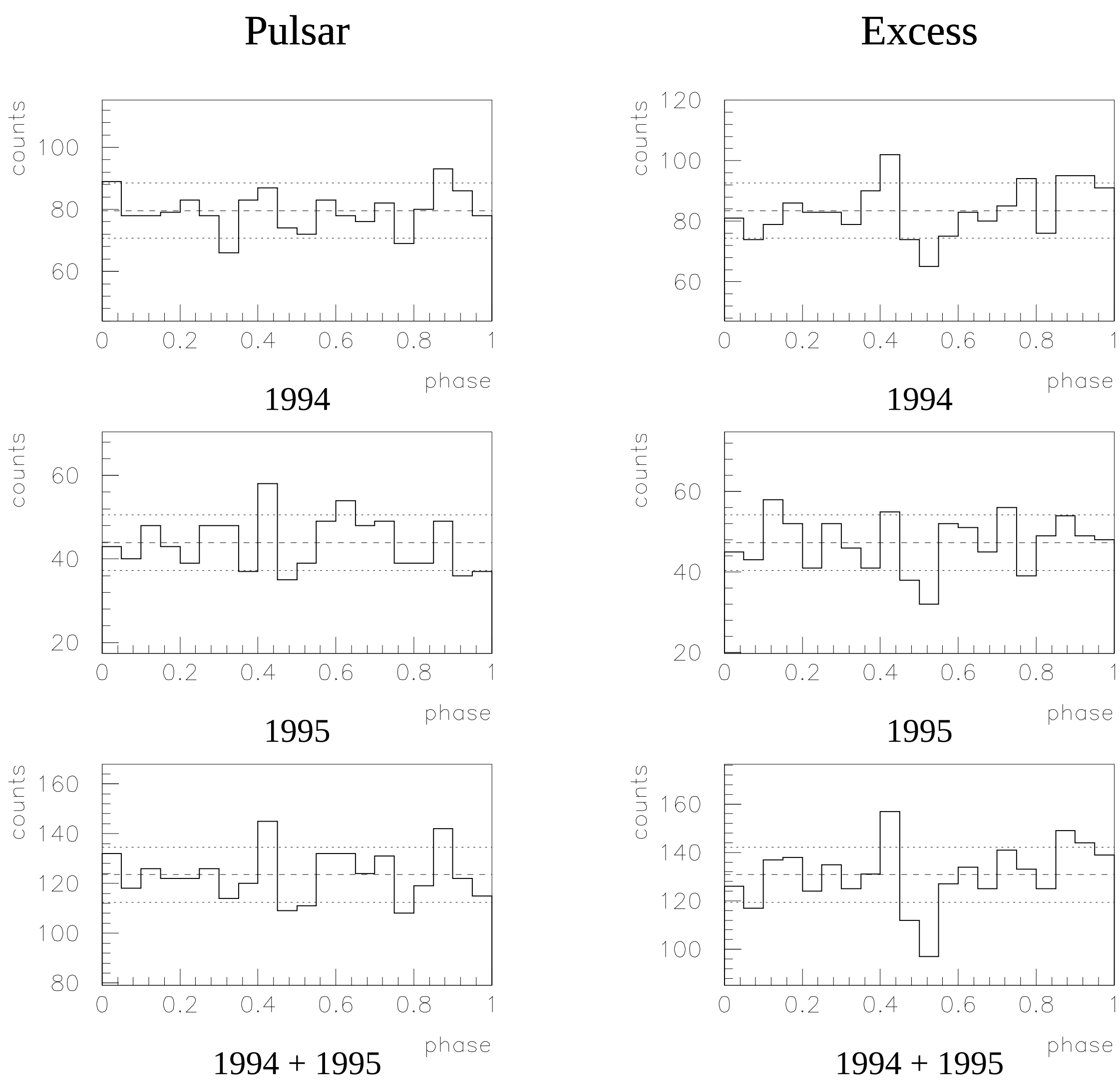

Figure 8.19: Lightcurves with respect to the Vela pulsar and the detected excess position. The lightcurves of 1994 and 1995 are incoherently summed, and the lightcurves of the total data are shown at the bottom. The events have been given by the canonical selection of (7.1) $\sim$ (7.3). The dashed lines indicate the average counts per bin and the dotted lines indicate the $\pm 1\sigma$ deviations from the average counts.

Year		Pulsar position		Excess position	
		Z_2^2	probability	Z_2^2	probability
1994	(1)	2.99 (1.99 + 1.00)	0.56 (0.37 + 0.61)	2.99 (1.99 + 1.00)	0.56 (0.37 + 0.61)
	(2)	1.22 (0.66 + 0.56)	0.88 (0.72 + 0.76)	6.45 (0.94 + 5.51)	0.17 (0.63 + 0.06)
	(3)	2.34 (1.66 + 0.69)	0.67 (0.44 + 0.71)	4.25 (0.12 + 4.13)	0.37 (0.94 + 0.13)
1995	(1)	2.69 (0.91 + 1.78)	0.61 (0.63 + 0.41)	2.69 (0.91 + 1.78)	0.61 (0.63 + 0.41)
	(2)	2.24 (1.35 + 0.89)	0.69 (0.51 + 0.64)	1.65 (1.09 + 0.56)	0.80 (0.58 + 0.76)
	(3)	1.33 (0.28 + 1.05)	0.86 (0.87 + 0.59)	1.31 (1.07 + 0.25)	0.86 (0.59 + 0.88)

Table 8.7: Results of the Z_2^2 test. The first and second harmonics are also shown in parentheses. See Table 8.5 for the explanation of (1) $\sim$ (3).

sinusoidal function taking its HE gamma-ray lightcurve (see Figure 3.1) into account. If f is the pulsed fraction in N events tested, Z_2^2 is asymptotically distributed as

$$p_2(Z_2^2; f^2N) = \int_0^{Z_2^2} p_1(Z_1^2; f^2N) p_1(Z_2^2 - Z_1^2; f^2N) dZ_1^2, \tag{8.4}$$

where

$$p_1(Z_1^2; f^2N) = \frac{I_0\left(\{2f^2NZ_1^2\}^{1/2}\right)}{2\exp\left(f^2N + Z_1^2/2\right)}, \tag{8.5}$$

and I_0 is the modified Bessel function of the first kind of order zero [89]. If independent M trials have been done and Z_{max} is the maximum value of Z_2^2, the upper limit to f^2N at a confidence level C is obtained by solving

$$C = 1 - \left\{1 - \int_{Z_{max}}^{\infty} p_2(Z_2^2; f^2N) dZ_2^2\right\}^M. \tag{8.6}$$

Table 8.8 shows the 95 % confidence upper limits to the pulsed fraction calculated from the values of Z_2^2 in Table 8.7.

The Z_2^2 tests have also been done on a day-by-day basis. The observations of the Vela pulsar has been done on 48 nights for the two years, and the maximum values of the Z_2^2

Year		Pulsar position		Excess position	
		pulsed fraction (%)	pulsed events	pulsed fraction (%)	pulsed events
1994	(1)	< 0.35	< 494	< 0.35	< 494
	(2)	< 1.9	< 30.0	< 4.5	< 75.3
	(3)	< 4.3	< 32.1	< 5.5	< 43.3
1995	(1)	< 0.37	< 432	< 0.37	< 432
	(2)	< 3.9	< 34.0	< 3.1	< 29.4
	(3)	< 3.7	< 17.7	< 3.5	< 18.3
total	(1)	< 0.20	< 522	< 0.20	< 522
	(2)	< 1.7	< 40.8	< 3.3	< 86.9
	(3)	< 2.0	< 23.9	< 3.7	< 48.2

Table 8.8: The 95 % confidence upper limits to the pulsed fraction and the corresponding numbers of events on the basis of the Z_2^2 test. See Table 8.5 for the explanation of (1) $\sim$ (3).

statistic are 12.7 (noise rejection only) and 15.9 (after the canonical selections) for the pulsar position and the excess position, respectively. These values correspond to the chance probabilities of 1.3×10^{-2} and 3.3×10^{-3}, but reduced to 0.46 and 0.15 considering that the independent 48 observations have been done. These results are also consistent with no pulsed emission.

It is possible that the excess events detected from the different direction from the Vela pulsar have periodicity in a different period from the pulsar period. A ± 0.1 msec range around the pulsar period has been searched with respect to the excess position using the Z_2^2 test on a day-by-day basis. The maximum Z_2^2 value of all tests is 28.7 at 89.265 msec given by 7520 sec data observed on 3rd March 1995 after the canonical gamma-ray selections. This value corresponds to the chance probability of 8.9×10^{-6}, but reduced to 5.1×10^{-3} after considering the number of independent periods in the range searched, n_I, given by

$$n_I \sim \frac{3T\Delta P}{P^2}, \tag{8.7}$$

where P is the fundamental pulsar period, ΔP is the width of the range searched and T is the time interval over which the observations were made [90]. The chance probability is further reduced to 0.22 after considering the number of observations, 48, and this is compatible with no pulsed emission having been detected. The periodograms for all observations have also been summed incoherently but no significant signal has been found from the summed periodogram.

8.5 Flux Estimation and Variability

To obtain the flux corresponding to the above excess count and the flux upper limit to the pulsed signal, the effective area of our telescope for gamma-ray detection has been investigated by a Monte Carlo simulation (see Appendix B). Figure 8.20 shows the effective area of the 3.8 m telescope as a function of energy for gamma rays from a point source. In the figure, both the effective area by the trigger only and after the canonical gamma-ray selection of (7.1) $\sim$ (7.3) are plotted. The direction of the simulated gamma-ray showers is at the zenith and the effective area of Figure 8.20 is almost the same as for the observations of the Vela pulsar which have been done mainly at zenith angle $< 20°$. If it is assumed that the power of the source differential spectrum is -2.5, which is roughly the same as the extrapolation of the Vela pulsar's spectral break observed by EGRET, and the threshold energy for gamma-ray detection is defined to be at the energy of the maximum differential flux, the threshold energy after the gamma-ray selection is about 2.5 TeV as shown in Figure 8.21. The systematic error for the threshold energy has been estimated to be about ± 1 TeV assuming the uncertainties of the differential spectral index, the trigger conditions and the reflectivity of the reflector to be $-3.0 \sim -2.0$, ± 0.5 photoelectrons $\times$ ± 0.5 PMTs and ± 5 % respectively. The effective area is averaged in the energy greater than 2.5 TeV assuming that the power of the source

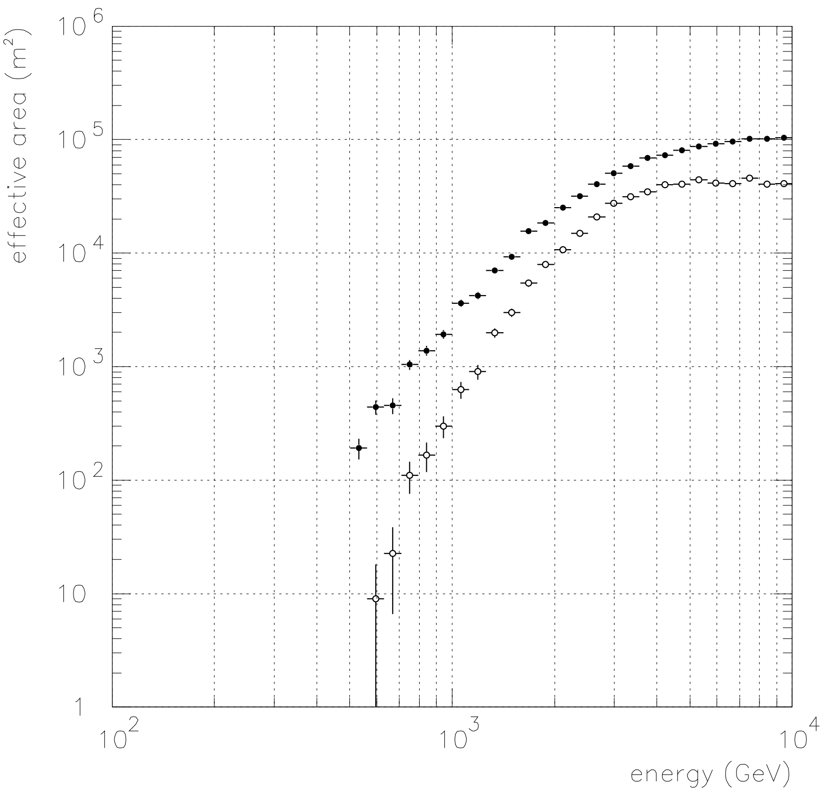

Figure 8.20: Effective area of the 3.8 m telescope as a function of energy for gamma rays given by Monte Carlo simulation. Filled circles indicate the effective area by the trigger only, while open circles indicate the effective area after the gamma-ray selection.

spectrum is -2.5. The averaged effective area then is $(3.36 \pm 0.04 \pm 0.6) \times 10^4$ m^2. The first and second errors are statistical and systematic respectively. The systematic error has been estimated assuming the above uncertainties. Thus, the gamma-ray integral flux detected near the direction of the Vela pulsar ($0^\circ.1$ to the south and $0^\circ.1$ to the east from the pulsar) is

$$F(> 2.5 \text{ TeV}) = (2.5 \pm 0.5 \pm 0.4) \times 10^{-12} \text{ photons cm}^{-2} \text{ sec}^{-1}. \quad (8.8)$$

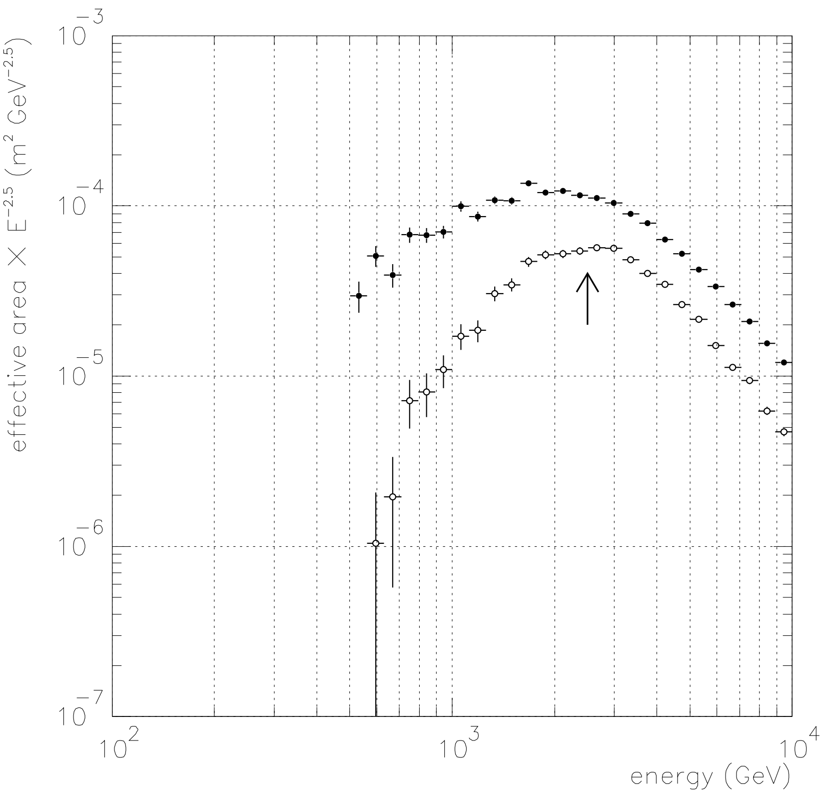

Figure 8.21: Definition of the threshold energy for gamma rays. The source differential spectrum is assumed to be -2.5. Then, the threshold energy is defined at the energy of the maximum differential flux and is about 2.5 TeV for gamma rays after the gamma-ray selections. The arrow shows the point of the maximum flux.

Once again, the first and second errors in this flux are statistical and systematic respectively. A severe cut for noise rejection has been applied to the 1993 data as mentioned above, and the effect has been considered in the calculation of the above flux. On the other hand, the 95 % confidence upper limits to the pulsed emission can also be calculated from the upper limits to the pulsed fraction in Table 8.8 under the assumption of a delta function phase distribution. From the results using the canonical gamma-ray selections ((2) in Table 8.8), the 95 % confidence flux upper limits for the pulsar position and the excess position are

$$F_{\rm pulsar}(> 2.5~{\rm TeV}) < (2.7 \pm 0.5) \times 10^{-13}~{\rm photons~cm^{-2}~sec^{-1}}, \tag{8.9}$$

and

$$F_{\rm excess}(> 2.5~{\rm TeV}) < (5.7 \pm 1.0) \times 10^{-13}~{\rm photons~cm^{-2}~sec^{-1}}, \tag{8.10}$$

respectively. The errors in (8.9) and (8.10) are systematic only.

The above fluxes are plotted in Figure 8.22 and Figure 8.23, together with HE and VHE gamma-ray fluxes previously reported by other groups. As mentioned in Chapter 3, the HE gamma-ray spectrum from the Vela pulsar reported by the EGRET group has a spectral break above 4 GeV and the dashed lines in Figure 8.22 and Figure 8.23 are its extrapolation in the energy greater than 4 GeV (the integral power ~ -1.59). Our results are further below the extrapolation. The EGRET group has also reported the upper limits to the unpulsed emission, and they are plotted by the open circles in Figure 8.22. On the other hand comparing with the other results in the VHE region, our detected flux is rather lower than the others. However, if any previous upper limit for the flux from the Vela pulsar was lower than our detected flux, it is not inconsistent with our result since our flux is the first one for the continuous emission from the direction of the Vela pulsar, while the other previous reports were results of period analyses. Our upper limit for the pulsed emission is of the lowest level of all the reported VHE fluxes.

The VHE gamma-ray luminosity at the emission region can be estimated from the above detected flux assuming that the distance to the emission region ~ 500 pc, the power of the differential spectrum ~ -2.5, the maximum gamma-ray energy ~ 10 TeV and the emission is isotropic (no beaming). The resultant gamma-ray luminosity is

$$L_\gamma \sim 5.2 \times 10^{32}~{\rm erg~sec^{-1}}. \tag{8.11}$$

This luminosity corresponds to the efficiency for VHE gamma-ray production, η,

$$\eta = \frac{L_\gamma}{\dot{E}} \sim 7.5 \times 10^{-5}, \tag{8.12}$$

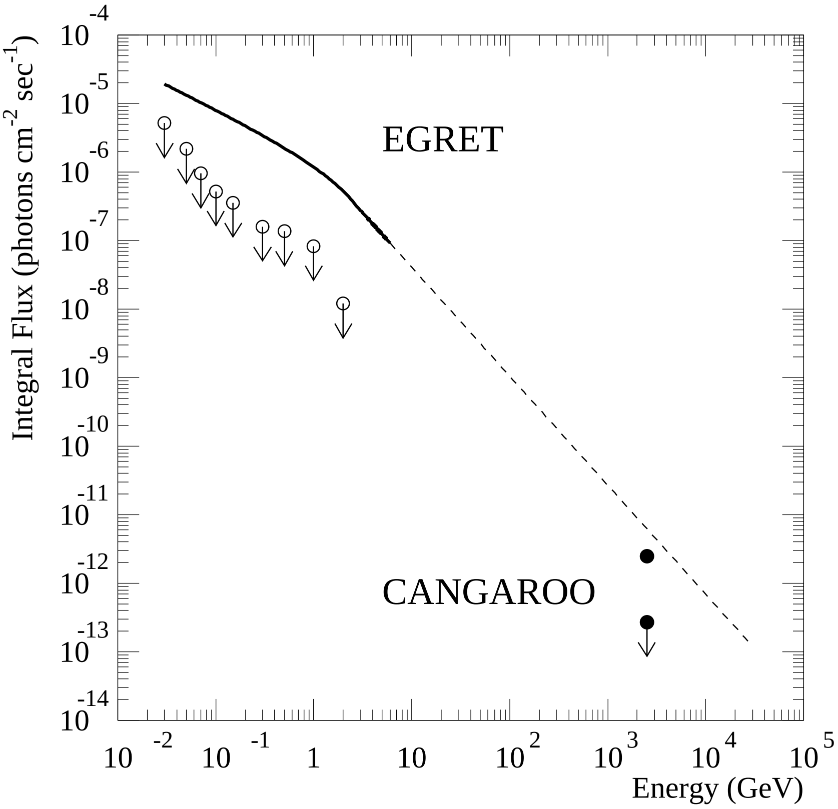

Figure 8.22: Integral gamma-ray fluxes from the direction of the Vela pulsar. Our results are plotted by filled circles with "CANGAROO". The upper filled circle represents the detected flux from the direction 0°.14 to the southeast of the pulsar, and the lower one is the upper limit to the pulsed emission from the Vela pulsar. The solid line represents the HE gamma-ray spectrum from the Vela pulsar observed by EGRET and the dashed line indicates the extrapolation of its spectral break seen above 4 GeV. The open circles are the upper limits to the HE unpulsed emission reported by the EGRET group [60].

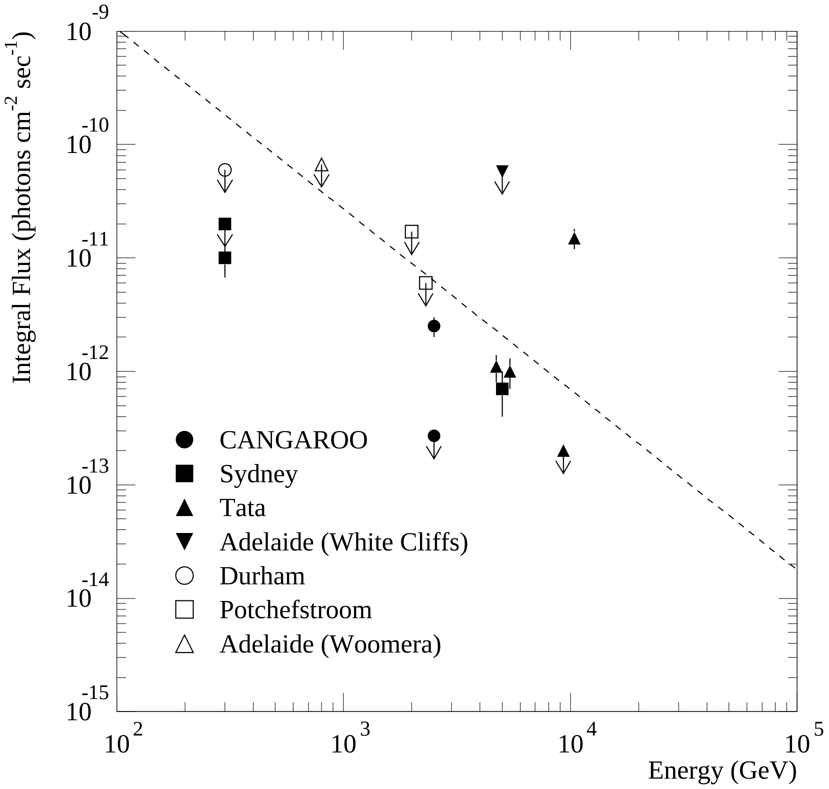

Figure 8.23: Integral VHE gamma-ray fluxes from the direction of the Vela pulsar. The dashed line is the extrapolation of the EGRET spectral break (Figure 8.22). Our results are plotted by filled circles as explained in the caption of Figure 8.22. The previous results summarized in Table 3.2 are also plotted.

where $\dot{E} = 6.9 \times 10^{36}$ erg sec^{-1} is the spindown luminosity of the Vela pulsar [115]. This efficiency is much lower than in the HE gamma-ray region ($\eta = 2.4 \times 10^{-3}$ [95]) and it is not energetically incompatible with a hypothesis that a part of the pulsar spindown energy is converted into the VHE gamma-ray emission, considering the visible energy from the Vela pulsar is much lower than the total spindown energy. The upper limit to the pulsed

Year	Flux (10^{-12} photons cm^{-2} sec^{-1})
1994	2.3 ± 1.3
1994	3.2 ± 0.9
1995	2.0 ± 0.7
total	2.5 ± 0.5

Table 8.9: Detected year-by-year and total fluxes. The errors are statistical.

gamma-ray luminosity from the Vela pulsar can be calculated as well as the above detected luminosity. However, it is here assumed instead of the above assumptions that gamma rays are emitted as a beam of 1 str in solid angle and the maximum gamma-ray energy is ~ 6 TeV following the prediction of the outer gap model [25]. Then, the upper limit to the pulsed VHE gamma-ray luminosity is

$$L_\gamma \lesssim 1.2 \times 10^{31} \text{ erg sec}^{-1}. \tag{8.13}$$

This corresponds to the upper limit to the VHE gamma-ray efficiency

$$\eta \lesssim 1.7 \times 10^{-6}. \tag{8.14}$$

This is about two orders of magnitude smaller than the prediction of the outer gap model described in Chapter 3. This result indicates that most of inverse Compton photons must be emitted below 2.5 TeV from the Vela outer gaps, even if the prediction of Cheng, Ho and Ruderman is correct.

To investigate time variability of the flux, the integral flux of (8.8) is divided into year-by-year fluxes. They are shown in Table 8.9 and plotted in Figure 8.24. The year-by-year fluxes agree well with their mean flux as seen in Figure 8.24. Thus, the data are compatible with no variation having been detected on the time scales of a year.

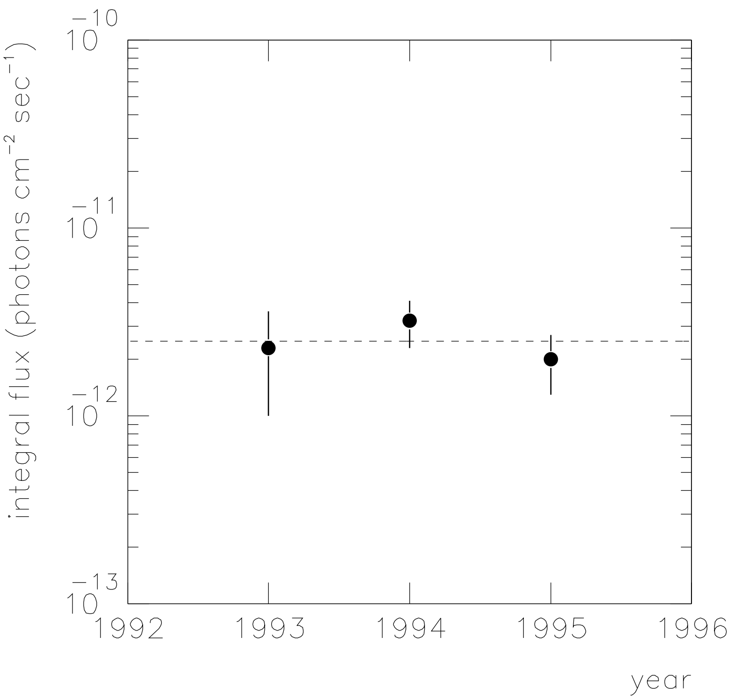

Figure 8.24: Detected gamma-ray fluxes as a function of year. The horizontal dashed line indicates the mean flux.

Chapter 9

Discussion and Conclusions

Gamma-ray-like events were detected from the direction of the Vela pulsar, but the position of the excess peak maximum is likely to differ from the pulsar position. If the signal is correlated with the pulsar, the distance of the emission region from the pulsar is an important parameter to understand the gamma-ray emission mechanism. In Chapter 8, the peak maximum position $(-0^\circ.1, -0^\circ.1)$ in Figure 8.14 has been determined from the mesh points of $0^\circ.05$ spacing. However, as mentioned in the end of Chapter 7, a more probable position of the gamma-ray emission region can be estimated by fitting the peak profile of Figure 8.14 to the modified PSF, together with the size of the emission region. The parameters in the function (7.21) have been obtained by the fitting as; $(x_s, y_s) = (-0^\circ.11, -0^\circ.08)$ and $\sigma_s = 0^\circ.09$. Note that σ_s means the standard deviation of the gamma-ray intensity distribution assumed to be a Gaussian distribution as defined in Chapter 7.

The errors of the above parameters due to the fluctuation of the background distributions have been estimated by simulations. The off-source map of Figure 8.7, which has been given by the asymmetrical SPDF, can be simulated assuming that the centroids and directions of background images are randomly distributed in the field of view. On the other hand, the on-source map has been simulated by superposing a gamma-ray peak, which has been simulated as the PSF of Figure 7.11 using the Monte Carlo simulation, to a simulated off-source map. A map of excess event density is obtained subtracting a simulated off-source map from a

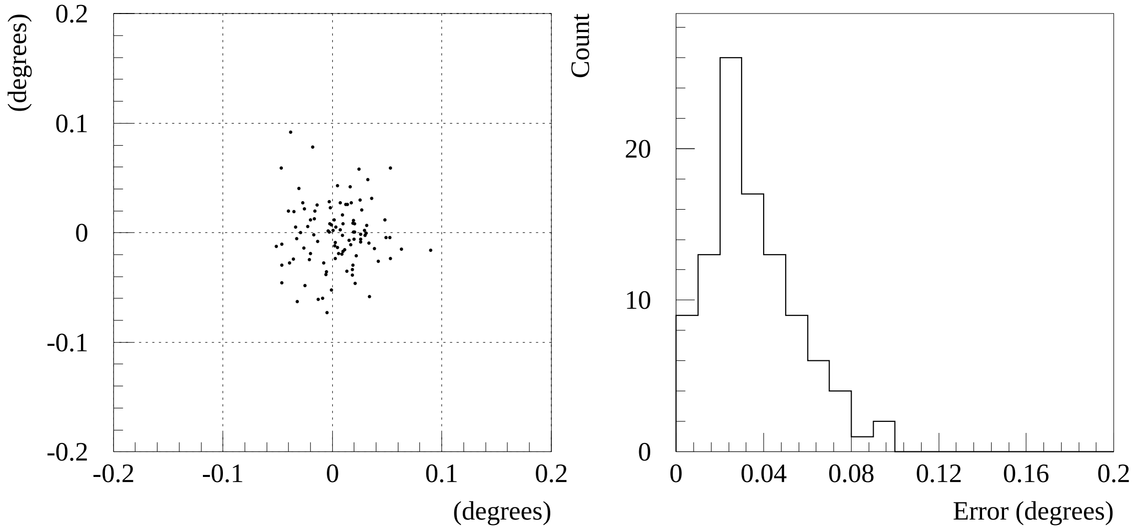

Figure 9.1: The distribution of the gamma-ray source positions obtained by fitting the simulated maps to the modified PSF. The source inputted to the simulation is at the origin of the left figure and its size is 0°.0. The right figure shows the radial error distribution. The standard deviation of this error distribution is about 0°.03.

simulated on-source map, and is fitted to the modified PSF to obtain (x_s, y_s) and σ_s as well as the above case for the observed map. This simulation has been done for the gamma-ray source sizes of 0°.0, 0°.05, 0°.1 and 0°.15, and their gamma-ray intensity distributions have been assumed to be Gaussian distributions (the above source sizes correspond to their standard deviations). Figure 9.1 shows the distribution of the estimated position (x_s, y_s) for the source of the size 0°.0 at the center of the field of view (the origin of the figure). The standard deviation of this "error" distribution is about 0°.03. However, it increases with the source size. When the source size is about 0°.1 as the case of the detected peak, the standard deviation is $\sim$ 0°.04. Thus, the position of the observed emission region is offset from the pulsar by

$$(x_s, y_s) = (-0^\circ.11 \pm 0^\circ.04, -0^\circ.08 \pm 0^\circ.04), \tag{9.1}$$

where the errors are statistical.

Considering that the tracking accuracy of our telescope is as good as $0^\circ.01$ (Chapter 5) and the calibration of the tracked point has been done with the accuracy better than $0^\circ.02$ (Chapter 6), the offset of about $0^\circ.14$ to the southeast from the pulsar is probably significant. It is possible to refute the thought that the offset is the result of not correctly 'flat fielding' the imaging camera, for example to errors in PMT gains, since such effects are canceled as the field of view rotates (more than 90° in a long run). The effect of stars in the field of view are checked using the same method as that of Krennrich [66]. The position angle of the image centroid with respect to the position of the excess peak is calculated for every gamma-ray selected event, and the distribution of the excess events in terms of significances as a function of the position angle is shown in Figure 9.2. The position angles of the stars in the field of view are shown by the arrows in the figure, together with their visual magnitudes. There is no significant correlation between the star's position angles and the distribution of the excess events. Therefore, the offset of the excess peak is not likely to be caused by the stars.

The angular size of the emission region is also an important parameter. In particular, if the emission region actually differ from the pulsar as mentioned above, it is interesting whether the pulsar is included in the emission region. The results of the above simulations are summarized with respect to the source size in Figure 9.3. The simulations have been done 100 times for each input source size, and the median values of the distributions of the output source size are plotted by the filled circles in the figure together with their error bars representing the range from 16 % to 84 %. It appears that the source sizes are reproduced by the fitting to the modified PSF with the accuracy of $\sim 0^\circ.03$. Thus, the size (radius) of the observed emission region is estimated as

$$\sigma_s = 0^\circ.09 \pm 0^\circ.03. \tag{9.2}$$

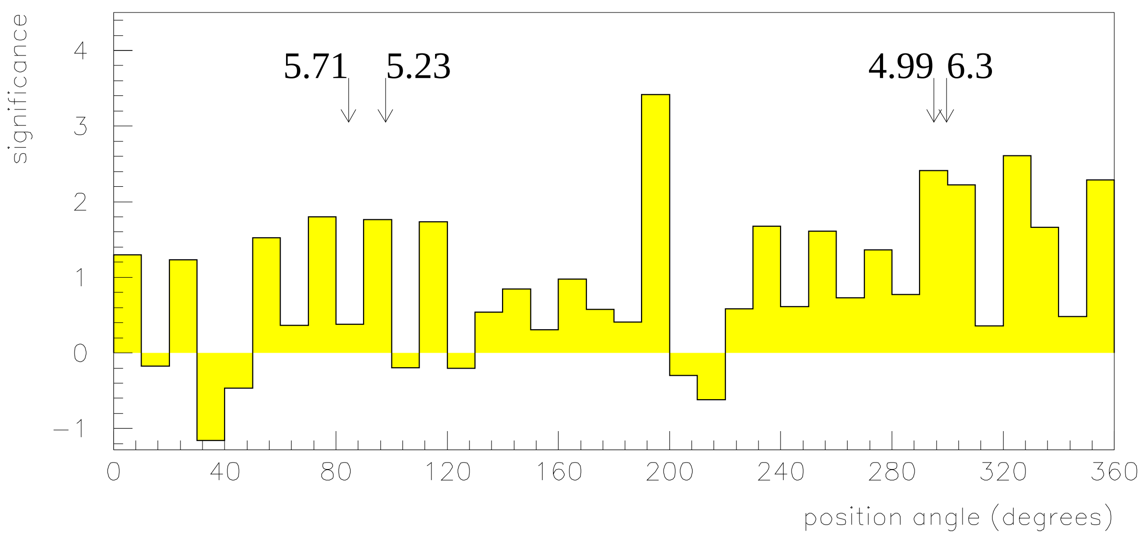

Figure 9.2: The distribution of the excess events in terms of significances as a function of the position angle with respect to the excess peak in Figure 8.14. The position angles of the stars in the field of view less than 1°.5 from the peak position are shown by the arrows. The star's visual magnitudes are also shown by the corresponding arrow.

Here, we assume that the source direction is $\sim 0°.14$ to the southeast of the pulsar and the angular size of the source is $\sim 0°.18$ in diameter following the above estimation. In this case, the distance of the emission region from the pulsar is about 1.2 pc assuming the pulsar distance of 500 pc. Thus, the emission region is much more distant from the pulsar than the light cylinder radius ($\sim 10^{-10}$ pc), and it is probably impossible for the detected signal to be due to particle acceleration at a site very close to the pulsar, say, the polar cap or the outer gap. This hypothesis is also supported by the fact that no pulsation has been detected at the pulsar period. If the detected emission is associated with the pulsar, the particle acceleration possible at a region 1 pc distant from an isolated pulsar is the pulsar

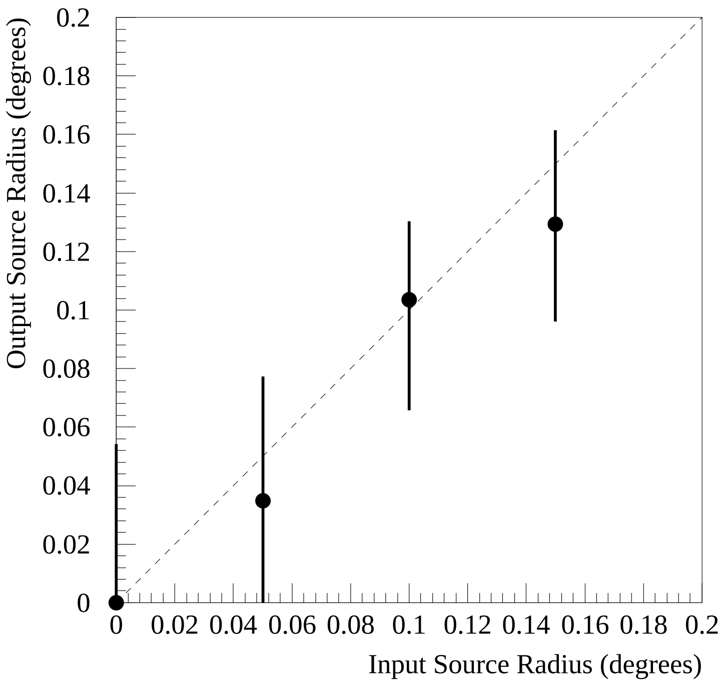

Figure 9.3: The source radii inputted to the simulations versus the output source radii. The filled circles represent the median values of the distributions of the output source size. The error bars show the range from 16 % to 84 % of the output distributions.

wind shock acceleration. This reminds us the case of the Crab pulsar and nebula. Thus, the plausible interpretation for the detected emission is that VHE gamma rays are emitted from shock accelerated particles by inverse Compton scattering.

One can estimate the maximum electron energy at the above shock near the Vela pulsar using the equations (2.13) and (2.14). Taking $\sigma = 0.003$ and $r_s \sim 4 \times 10^{18}$ cm (~ 1.2 pc), the maximum electron energy is $E_{max} \sim 7 \times 10^{14}$ eV. Thus, VHE gamma rays can be produced by the electrons accelerated at the shock in the model of Kennel and Coroniti.

On the other hand, the emission region has been assumed to be $\sim 0^{\circ}.18$ (~ 1.6 pc) above, and does not possibly include the pulsar. There are two possible interpretations about the association between the pulsar wind and the emission region:

- A directional wind (a jet) is ejected to the southeast.
- A spherical wind is ejected, but the pressure of the ambient matter is higher at the emission region.

Jets from the Crab pulsar and the Vela pulsar have actually been observed at X-ray wavelengths and it is not unnatural for jets to be ejected from pulsars. However, all of the observed jets are ejected to the direction of the pulsar rotation axes, while the direction of the above emission region from the pulsar is almost perpendicular to the pulsar rotation axis. This asymmetrical jet with respect to the pulsar rotation axis is not likely to be explained by any currently existing model.

Here, let us assume both the pulsar winds and the gamma-ray emission from the emission region to be spherical (isotropic). If S is the size of the emission region, the luminosity transported to the emission region from the pulsar is $\sim S^2\dot{E}/4\pi r_s^2$. If f is the conversion factor of the luminosity to the VHE gamma-ray emission in the emission region,

$$\eta = \frac{L_\gamma}{\dot{E}} \sim \frac{S^2 f}{4\pi r_s^2} = 1.4 \times 10^{-1} f \left(\frac{S}{1.6\ \mathrm{pc}}\right)^2 \left(\frac{r_s}{1.2\ \mathrm{pc}}\right)^{-2}. \tag{9.3}$$

Equating this equation with (8.12),

$$f \sim 6 \times 10^{-4} \left(\frac{S}{1.6\ \mathrm{pc}}\right)^{-2} \left(\frac{r_s}{1.2\ \mathrm{pc}}\right)^2. \tag{9.4}$$

As seen in Section 8.3, the gamma-ray luminosity corresponding to the detected flux is much smaller than the spindown luminosity of the Vela pulsar. However, the energy in the emission region is converted into VHE gamma rays in at least an order of magnitude higher efficiency in this model.

At the end of the discussion, it is pointed out that an interesting feature which may imply the existence of a shock at the southeast of the pulsar is found in the ROSAT image of the region around the Vela pulsar (Figure 3.4). In this image, diffuse X-ray emission is present at the direction of the detected gamma-ray signal. The authors have not given any interpretation of this diffuse emission.

In conclusion, we have observed the Vela pulsar with the CANGAROO 3.8 m telescope during January 1993 and March 1995. A gamma-ray signal has been detected from the direction of the Vela pulsar at about 6 σ level using the atmospheric Čerenkov imaging technique. The integral gamma-ray flux is $(2.5 \pm 0.5 \pm 0.4) \times 10^{-12}$ photons cm^{-2} sec^{-1} above 2.5 ± 1.0 TeV, and is steady on a one year time scale. The signal is likely to be offset from the pulsar position to the southeast, and the emission region is likely to be extended but small compared with the offset. No pulsed emission has been detected from the pulsar nor the direction of the detected signal. The 95 % confidence flux upper limit to the pulsed emission from the pulsar has been set to be $(2.7 \pm 0.5) \times 10^{-13}$ photons cm^{-2} sec^{-1} above 2.5 ± 1.0 TeV.

A calibration technique to get a tracked point in the field of view of the imaging camera using starlight has been developed. The accuracy of the calibration was confirmed to be less than $0^{\circ}.02$ using simulations, and this is as good as the tracking accuracy of the 3.8 m telescope. Results of this calibration have been reflected in the above analyses.

New analysis techniques have been developed and applied to the data including the above gamma-ray signal. A new image parameter "Asymmetry" has been expected to be effective to extract a tendency of gamma-ray images pointing to their source. This tendency has been found in the Asymmetry distribution of the detected excess events, and this is strong evidence of the excess events being due to gamma rays. On the other hand, the "source probability density functions" have been defined from the source distribution with respect to the position of simulated gamma-ray images, and the use of this function instead of the conservative method is more effective to accurately determine a gamma-ray source position in the field of view. It has been confirmed that both of the techniques are also effective to enhance a gamma-ray signal.

Our new project for observations of 50 GeV gamma rays with a 10 m telescope has been financed in 1995 and the telescope will be in operation four years later. VHE gamma-ray observations with higher resolution and a lower threshold energy will be possible with the 10 m telescope. Therefore, the above features around the Vela pulsar will be revealed more clearly by the 10 m telescope.

References

[1] Aharonian, F.A. and Atoyan, A.M., *Astropart. Phys.*, **3**, 275-282 (1995).

[2] Akerlof, C.W., et al., *Astrophys. J.*, **377**, L97-L100 (1991). (1993).

[3] Antonucci, R.R.J. & Miller, J.S., *Astrophys. J.*, **297**, 621-632 (1985).

[4] Arons, J., *Proc. IAU Symp. 94 "Origin of Cosmic Rays", Bologna*, 175-204 (1981).

[5] Arons, J., *Adv. Space Res.*, **3 (10-12)**, 287-296 (1984).

[6] Aschenbach, B., Egger, R. & Trümper, J., *Nature*, **373**, 587-590 (1995).

[7] Awaki, H., et al., *Publ. Astron. Soc. Japan*, **43**, 195-212 (1991).

[8] Bailes, M., et al., *Astrophys. J.*, **343**, L53-L55 (1989).

[9] Baillon, P., et al., *Proc. 22nd Internat. Cosmic Ray Conf., Dublin*, **1**, 220-223 (1991).

[10] Baillon, P., et al., *Proc. 23rd Internat. Cosmic Ray Conf., Calgary*, **1**, 271-274 (1993).

[11] Baltrusaitis, R.M., et al., *Nucl. Inst. Meth. Phys. Res. A*, **240**, 410-428 (1985).

[12] Beaman, J., et al., *Proc. 23rd Internat. Cosmic Ray Conf., Calgary*, **1**, 346-348 (1993).

[13] Bertsch, D.L., et al., *Nature*, **357**, 306-307 (1992).

[14] Bertsch, D.L., et al., *Astrophys. J.*, **416**, 587-600 (1993).

[15] Bhat, P.N., et al., *Astron. Astrophys.*, **81**, L3-L5 (1980).

[16] Bhat, P.N., et al., *Astron. Astrophys.*, **178**, 242-246 (1987).

[17] Biller, S.D., et al., *Astrophys. J.*, **445**, 227-230 (1995).

[18] Blandford, R.D. & Ostriker, J.P., *Astrophys. J.*, **237**, 793-808 (1980).

[19] Brazier, K.T.S., et al., *Proc. 21st Internat. Cosmic Ray Conf., Adelaide*, **2**, 304-307 (1990).

[20] Buccheri, R., et al., *Astron. Astrophys.*, **69**, 141-142 (1978).

[21] Buccheri, R., et al., *Astron. Astrophys.*, **128**, 245-251 (1983).

[22] Buckley, J.H., et al., *Proc. Internat. Workshop "Towards a Major Atmospheric Cherenkov Detector III", Tokyo*, 171-178 (1994).

[23] Chen, K. & Ruderman, M., *Astrophys. J.*, **402**, 264-270 (1993).

[24] Cheng, K.S., Ho, C. & Ruderman, M., *Astrophys. J.*, **300**, 500-521 (1986).

[25] Cheng, K.S., Ho, C. & Ruderman, M., *Astrophys. J.*, **300**, 522-539 (1986).

[26] Cheng, K.S. & Ding, W.K.Y., *Astrophys. J.*, **431**, 724-731 (1994).

[27] Ciliegi, P., Bassani, L. & Caroli, E., *Astrophys. J. Suppl.*, **85**, 111-118 (1993).

[28] Clay, R.W., et al., *Proc. 20th Internat. Cosmic Ray Conf., Moscow*, **1**, 271-274 (1987).

[29] Degrange, B., *Proc. Internat. Workshop "Towards a Major Atmospheric Cherenkov Detector III", Tokyo*, 305-310 (1994).

[30] Degrange, B. & Le Bohec, S., *Proc. 24th Internat. Cosmic Ray Conf., Rome*, **3**, 436-439 (1995).

[31] De Jager, O.C. & Harding, A.K., *Astrophys. J.*, **396**, 161-172 (1992).

[32] De Jager, O.C., Stecker, F.W. & Salamon, M.H., *Nature*, **369**, 294-296 (1994).

[33] Edwards, P.G., et al., *Astron. Astrophys.*, **291**, 468-472 (1994).

[34] Emmering, R.T. & Chevalier, R.A., *Astrophys. J.*, **321**, 334-348 (1987).

[35] Erber, T., *Rev. Mod. Phys.*, **38**, 626-659 (1966).

[36] Fegan, D.J., et al., *Proc. Internat. Workshop "Towards a Major Atmospheric Cherenkov Detector III", Tokyo*, 149-162 (1994).

[37] Fermi, E., *Phys. Rev.*, **75**, 1169-1174 (1949).

[38] Fichtel, C.E., et al., *Astrophys. J.*, **198**, 163-182 (1975).

[39] Fichtel, C.E., et al., *Astrophys. J. Suppl.*, **94**, 551-581 (1994).

[40] Fierro, J.M., et al., *Astrophys. J.*, **413**, L27-L30 (1993).

[41] Fomin, V.P., et al., *Astropart. Phys.*, **2**, 137-150 (1994).

[42] Fontaine, G., *Nucl. Phys. B (Proc. Suppl.)*, **14B**, 79-94 (1990).

[43] Ford, H.C., et al., *Astrophys. J.*, **435**, L27-L30 (1994).

[44] Gaisser, T.K., *"Cosmic Rays and Particle Physics"*, Cambridge University Press (1990).

[45] Goldreich, P. and Julian, W.H., *Astrophys. J.*, **157**, 869-880 (1969).

[46] Goret, P., et al., *Proc. 22nd Internat. Cosmic Ray Conf., Dublin*, **2**, 630-633 (1991).

[47] Goret, P., et al., *Astron. Astrophys.*, **270**, 401-406 (1993).

[48] Grenier, I.A., Hermsen, W. & Clear, J., *Astron. Astrophys.*, **204**, 117-132 (1988).

[49] Grindlay, J.E., et al., *Astrophys. J.*, **201**, 82-89 (1975).

[50] Hara, T., et al., *Nucl. Inst. Meth. Phys. Res. A*, **332**, 300-309 (1993).

[51] Harding, A.K., *Nucl. Phys. B (Proc. Suppl.)*, **14A**, 3-16 (1990).

[52] Harms, R.J., et al., *Astrophys. J.*, **435**, L35-L38 (1994).

[53] Harnden, F.R., et al., *Astrophys. J.*, **299**, 828-838 (1985).

[54] Heitler, W., *"The Quantum Theory of Radiation"*, Oxford University Press (1954).

[55] Hester, J.J., et al., *Astrophys. J.*, **448**, 240-263 (1995).

[56] Hewish, A., et al., *Nature*, **217**, 709-713 (1968).

[57] Hillas, A.M., *J. Phys. G*, **8**, 1475-1492 (1982).

[58] Hillas, A.M., *Proc. 19th Internat. Cosmic Ray Conf., La Jolla*, **3**, 445-448 (1985).

[59] Jelley, J.V., *"Čerenkov Radiation and its Applications"*, Pergamon Press (1958).

[60] Kanbach, G., et al., *Astron. Astrophys.*, **289**, 855-867 (1994).

[61] Kennel, C.F. & Coroniti, F.V., *Astrophys. J.*, **283**, 694-709 (1984).

[62] Kennel, C.F. & Coroniti, F.V., *Astrophys. J.*, **283**, 710-730 (1984).

[63] Kifune, T., et al., *Astrophys. J.*, **438**, L91-L94 (1995).

[64] Kifune, T., et al., *Aust. J. Phys.*, **48**, 305-319 (1995).

[65] Konopelko, A., et al., *Astropart. Phys.*, in press (1996).

[66] Krennrich, F., *Proc. Internat. Workshop "Towards a Major Atmospheric Cherenkov Detector III", Tokyo*, 71-82 (1994).

[67] Large, M.I., Vaughan, A.E. & Mills, B.Y., *Nature*, **220**, 340-341 (1968).

[68] Li, T. & Ma, Y., *Astrophys. J.*, **272**, 317-324 (1983).

[69] Longair, M.S., *"High Energy Astrophysics"*, Cambridge University Press (1981).

[70] Lyne, A.G. & Manchester, R.N., *Mon. Not. R. astr. Soc.*, **234**, 477-508 (1988).

[71] MacKeown, P.K., et al., *Proc. 18th Internat. Cosmic Ray Conf., Bangalore*, **9**, 175-178 (1983).

[72] Macomb, D.J., et al., *Astrophys. J.*, **449**, L99-L103 (1995).

[73] Manchester, R.N., *Astron. Astrophys.*, **171**, 205-215 (1987).

[74] Markwardt, C.B. & Ögelman, H., *Nature*, **375**, 40-42 (1995).

[75] Mayer-Hasselwander, H.A., et al., *Astron. Astrophys.*, **105**, 164-175 (1982).

[76] McCulloch, P.M., et al., *Nature*, **303**, 307-308 (1983).

[77] Michelson, P.F., *Proc. Internat. Workshop "Towards a Major Atmospheric Cherenkov Detector III", Tokyo*, 321-331 (1994).

[78] Miyoshi, M., et al., *Nature*, **373**, 127-129 (1995).

[79] Naito, T. & Takahara, F., *Proc. Internat. Workshop "Towards a Major Atmospheric Cherenkov Detector III", Tokyo*, 289-293 (1994).

[80] Nel, H.I., et al., *Astrophys. J.*, **398**, 602-609 (1992).

[81] Nel, H.I., et al., *Astrophys. J.*, **418**, 836-843 (1993).

[82] Nolan, P.L., et al., *Astrophys. J.*, **409**, 697-704 (1993).

[83] Ögelman, H., Finley, J.P. & Zimmermann, H.U., *Nature*, **361**, 136-138 (1993).

[84] Ögelman, H. & Zimmermann, H.U., *Astron. Astrophys.*, **214**, 179-185 (1989).

[85] Oke, J.B. & Schild, R.E., *Astrophys. J.*, **161**, 1015-1023 (1970).

[86] Ong, R.A., et al., *Proc. Internat. Workshop "Towards a Major Atmospheric Cherenkov Detector III", Tokyo*, 295-303 (1994).

[87] Ostriker, J.P. & Gunn, J.E., *Astrophys. J.*, **157**, 1395-1417 (1969).

[88] Petry, D., *Proc. 24th Internat. Cosmic Ray Conf., Rome*, **2**, 495-498 (1995).

[89] Protheroe, R.J., *Proc. Astron. Soc. Aust.*, **7 (2)**, 167-172 (1987).

[90] Protheroe, R.J., *Proc. NATO Workshop "Very High Energy Gamma Ray Astronomy", Durham*, 91-100 (1987).

[91] Punch, M., et al., *Nature*, **358**, 477-478 (1992).

[92] Punch, M., Ph.D. thesis, National University of Ireland (1993).

[93] Quinn, J., et al., *Astrophys. J.*, **456**, L83-L86 (1996).

[94] Ramana Murthy, P.V. & Wolfendale, A.W., *"Gamma-Ray Astronomy"*, Cambridge University Press (1986).

[95] Ramana Murthy, P.V., et al., *Astrophys. J.*, **447**, L109-L112 (1995).

[96] Ramana Murthy, P.V., et al., *Astrophys. J.*, **458**, 755-760 (1996).

[97] Rees, M.J. & Gunn, J.E., *Mon. Not. R. astr. Soc.*, **167**, 1-12 (1974).

[98] Reynolds, P.T., et al., *Astrophys. J.*, **404**, 206-218 (1993).

[99] Reynolds, P.T., et al., *J. Phys. G*, **19**, 1217-1231 (1993).

[100] Ruderman, M.A. & Sutherland, P.G., *Astrophys. J.*, **196**, 51-72 (1975).

[101] Ruderman, M. & Cheng, K.S., *Astrophys. J.*, **335**, 306-318 (1988).

[102] Salamon, M.H., Stecker, F.W. & De Jager, O.C., *Astrophys. J.*, **423**, L1-L4 (1994).

[103] Schönfelder, V., *J. Phys. G*, **19**, S65-S80 (1993).

[104] Sembroski, G., et al., *Proc. 24th Internat. Cosmic Ray Conf., Rome*, **3**, 428-431 (1995).

[105] Seward, F.D., *Space Sci. Rev.*, **49**, 385-423 (1989).

[106] Shapiro, S.L. & Teukolsky, S.A., *"Black Holes, White Dwarfs, and Neutron Stars"*, A Wiley-Interscience Publication (1983).

[107] Standish, E.M., *Astron. Astrophys.*, **114**, 297-302 (1982).

[108] Stecker, F.W., Puget, J.L. & Fazio, G.G., *Astrophys. J.*, **214**, L51-L55 (1977).

[109] Stecker, F.W., De Jager, O.C. & Salamon, M.H., *Astrophys. J.*, **390**, L49-L52 (1992).

[110] Sturner, S.J. & Dermer, C.D., *Astron. Astrophys.*, **293**, L17-L20 (1995).

[111] Sturrock, P.A., *Nature*, **227**, 465-470 (1970).

[112] Tanaka, Y., et al., *Nature*, **375**, 659-661 (1995).

[113] Tanimori, T., et al., *Astrophys. J.*, **429**, L61-L64 (1994).

[114] Tanimori, T., et al., *Proc. Internat. Workshop "Towards a Major Atmospheric Cherenkov Detector III", Tokyo*, 311-319 (1994).

[115] Taylor, J.H., Manchester, R.N. & Lyne, A.G., *Astrophys. J. Suppl.*, **88**, 529-568 (1993).

[116] Taylor, J.H. & Weisberg, J.M., *Astrophys. J.*, **345**, 434-450 (1989).

[117] Thompson, D.J., et al., *Astrophys. J.*, **200**, L79-L82 (1975).

[118] Thompson, D.J., et al., *Nature*, **359**, 615-616 (1992).

[119] Thompson, D.J., et al., *Astrophys. J. Suppl.*, **101**, 259-286 (1995).

[120] Thornton, G.J., et al., *Proc. Internat. Workshop "Towards a Major Atmospheric Cherenkov Detector III", Tokyo*, 125-129 (1994).

[121] Thornton, G.J., et al., *Proc. 24th Internat. Cosmic Ray Conf., Rome*, **3**, 476-479 (1995).

[122] Vacanti, G., et al., *Astrophys. J.*, **377**, 467-479 (1991).

[123] Wallace, P.T., et al., *Nature*, **266**, 692-694 (1977).

[124] Weekes, T.C., *Phys. Rep.*, **160**, 1-121 (1988).

[125] Weekes, T.C., et al., *Astrophys. J.*, **342**, 379-395 (1989).

[126] Weiler, K.W. & Panagia, N., *Astron. Astrophys.*, **70**, 419-422 (1978).

[127] Weiler, K.W. & Panagia, N., *Astron. Astrophys.*, **90**, 269-282 (1980).

[128] Willmore, A.P., et al., *Mon. Not. R. astr. Soc.*, **254**, 139-145 (1992).

Appendix A

Definition of the Image Parameters

Definition of the image parameters used in this thesis is almost the same as of the Hillas parameters originally used in the Whipple group [92, 98]. However, the following definition based on the Asymmetry Vector is convenient to make event maps as described in Chapter 7. Suppose the ith PMT is given by coordinates (x_i, y_i) in degrees and registers a signal s_i. The following is first defined:

$$\langle x\rangle = \frac{\sum s_i x_i}{\sum s_i}, \quad \langle y\rangle = \frac{\sum s_i y_i}{\sum s_i}, \tag{A.1}$$

$$\langle x^2\rangle = \frac{\sum s_i x_i^2}{\sum s_i}, \quad \langle xy\rangle = \frac{\sum s_i x_i y_i}{\sum s_i}, \quad \langle y^2\rangle = \frac{\sum s_i y_i^2}{\sum s_i}, \tag{A.2}$$

$$\langle x^3\rangle = \frac{\sum s_i x_i^3}{\sum s_i}, \quad \langle x^2 y\rangle = \frac{\sum s_i x_i^2 y_i}{\sum s_i}, \quad \langle xy^2\rangle = \frac{\sum s_i x_i y_i^2}{\sum s_i}, \quad \langle y^3\rangle = \frac{\sum s_i y_i^3}{\sum s_i}. \tag{A.3}$$

The coordinates $(\langle x\rangle, \langle y\rangle)$ correspond to the centroid of the image. The following is further defined:

$$\sigma_{x^2} = \langle x^2\rangle - \langle x\rangle^2, \quad \sigma_{xy} = \langle xy\rangle - \langle x\rangle\langle y\rangle, \quad \sigma_{y^2} = \langle y^2\rangle - \langle y\rangle^2, \tag{A.4}$$

$$\sigma_{x^3} = \langle x^3\rangle - 3\langle x^2\rangle\langle x\rangle + 2\langle x\rangle^3, \quad \sigma_{y^3} = \langle y^3\rangle - 3\langle y^2\rangle\langle y\rangle + 2\langle y\rangle^3, \tag{A.5}$$

$$\sigma_{x^2y} = \langle x^2 y\rangle - 2\langle xy\rangle\langle x\rangle + 2\langle x\rangle^2\langle y\rangle - \langle x^2\rangle\langle y\rangle, \quad \sigma_{xy^2} = \langle xy^2\rangle - 2\langle xy\rangle\langle y\rangle + 2\langle x\rangle\langle y\rangle^2 - \langle y^2\rangle\langle x\rangle. \tag{A.6}$$

If $d = \sigma_{y^2} - \sigma_{x^2}$ and $z = [d^2 + 4\sigma_{xy}^2]^{1/2}$, then

$$\text{Width} = \left(\frac{\sigma_{x^2} + \sigma_{y^2} - z}{2}\right)^{1/2}, \quad \text{Length} = \left(\frac{\sigma_{x^2} + \sigma_{y^2} + z}{2}\right)^{1/2}. \tag{A.7}$$

If an assumed source position in the field of view is (x_s, y_s) and the Distance vector $\vec{D} = (x_D, y_D)$ is defined as

$$\vec{D} = (x_s - \langle x \rangle, y_s - \langle y \rangle), \tag{A.8}$$

then

$$\text{Distance} = (x_D^2 + y_D^2)^{1/2}. \tag{A.9}$$

If an unit vector of the major axis, $\vec{u} = (x_u, y_u)$, is

$$\vec{u} = \left(\left(\frac{z-d}{2z} \right)^{1/2}, \ \text{sign}(\sigma_{xy}) \left(\frac{z+d}{2z} \right)^{1/2} \right), \tag{A.10}$$

then

$$\text{Alpha} = \cos^{-1} \left(\frac{x_u x_D + y_u y_D}{\text{Distance}} \right). \tag{A.11}$$

The Asymmetry vector $\vec{A} = (x_A, y_A)$ is

$$\vec{A} = -\sigma_A \vec{u}, \tag{A.12}$$

where

$$\sigma_A = \{\sigma_{x^3} \cos^3\phi + 3\sigma_{x^2y} \cos^2\phi \sin\phi + 3\sigma_{xy^2} \cos\phi \sin^2\phi + \sigma_{y^3} \sin^3\phi\}^{1/3} \tag{A.13}$$

and ϕ is the angle of $\vec{u}$ with respect to the x axis. Asymmetry is defined as

$$\text{Asymmetry} = \text{sign}(\vec{A} \cdot \vec{D}) \frac{|\sigma_A|}{\text{Length}} = \frac{\vec{A} \cdot \vec{D}}{\text{Distance Length } \cos(\text{Alpha})}. \tag{A.14}$$

If the largest two PMT signals in the image is S_1 and S_2, then

$$\text{Conc} = \frac{S_1 + S_2}{\sum s_i}. \tag{A.15}$$

Appendix B

Monte Carlo Simulation of Atmospheric Čerenkov Light

Monte Carlo simulation of atmospheric Čerenkov light used in this thesis is shortly explained here. The simulation program consists of production of an EAS from a primary particle, production of Čerenkov photons from the EAS and production of triggered images by telescopes distributed on the ground.

To generate EASs, GEANT version 3.15 has been used. GEANT is a system of detector description and simulation tools for the high energy particle physics and has been developed in CERN. We have considered the atmosphere as a particle detector of 80 layers and the US standard atmosphere has been used to calculate air density.

Čerenkov photons are produced from each particle generated by GEANT. Numbers of Čerenkov photons have been calculated using the equation (4.6) assuming that the quantum efficiency of the PMTs is constant in the wavelength region from 350 nm to 550 nm. The numbers of Čerenkov photons have further been reduced taking the Rayleigh and Mie scattering into account.

Generated Čerenkov photons have been collected by the reflectors put on the ground. They have been checked for compatibility with the trigger criteria described in Chapter 5 and an image has been constructed for each triggered event taking the noise level into account.

The simulated images are fed to the same program used in the analysis of real data.

The Monte Carlo simulation of background showers (proton showers) has been done and the results have been checked for compatibility with real observations in the triggering rate and the parameter distributions. The proton showers have been simulated in the energy range from 500 GeV to 20 TeV with the primary differential power of -2.7. The primary directions of the protons have been distributed uniformly in the $3°$ radius field, which is about four times larger than the field of view of the camera, and the shower axes have also been distributed uniformly in the area less than 300 m from the telescope, which is much larger than the effective detection area. The expected triggering rate, R, can be calculated as

$$R \sim \eta A \Omega \int_{E_{\min}}^{E_{\max}} f(E) dE, \tag{B.1}$$

where η is the trigger efficiency given by the simulation, $\Omega = 2\pi(1 - \cos 3°) \sim 8.6 \times 10^{-3}$ str, $A = \pi(300 \text{ m})^2 \sim 2.8 \times 10^9 \text{ cm}^2$ and $f(E) = 1.8E^{-2.7} \text{ cm}^{-2} \text{ sec}^{-1} \text{ str}^{-1} \text{ GeV}^{-1}$ [44] is the differential spectrum of cosmic rays. 2873 simulated events have been triggered out of 1.1 million trials, thus $\eta \sim 2.6 \times 10^{-3}$. Then, the expected triggering rate due to background showers is obtained as $R \sim 0.9$ Hz. This result is consistent with the triggering rate in real observations (~ 1 Hz).

The image parameter distributions for simulated proton showers have also been compared with the distributions for observed background showers. (Figure B.1). Although there seems to be a small difference between the distributions in Conc, the observed parameter distributions have been reproduced well by the simulation.

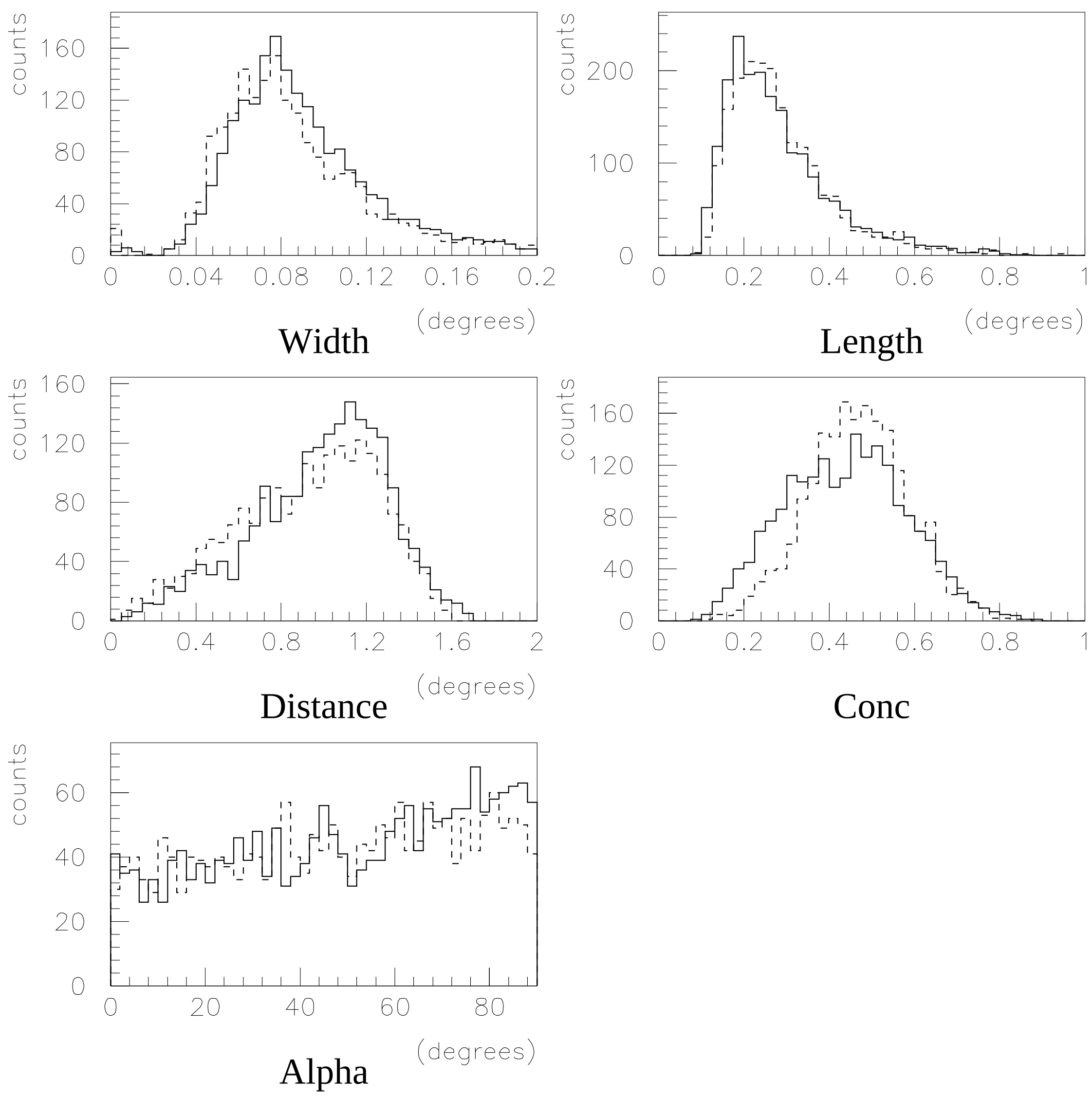

Figure B.1: Image parameter distributions given by real observations (solid lines) and the Monte Carlo simulation (dashed lines). The primary particle used in the Monte Carlo simulation is proton and the power of the primary differential spectrum is -2.7. The maximum core distance in the simulation is 300 m. The primary directions are taken randomly in the region less than 3° from the zenith, while the real data have been taken in the zenith angles less than 20°. The histograms have been normalized with the total number of events.